DEVELOPMENT AND PROPAGATION OF PREMIXED AND DIFFUSION FLAMES IN CONFINED CHANNELS

By

Ashwin Hariharan

A DISSERTATION

Submitted to
Michigan State University
in partial fulfillment of the requirements
for the degree of

Mechanical Engineering – Doctor of Philosophy

2016

ABSTRACT

DEVELOPMENT AND PROPAGATION OF PREMIXED AND DIFFUSION FLAMES IN CONFINED CHANNELS

By

Ashwin Hariharan

This work presents the experimental and numerical investigation of premixed and diffusion flame propagation in confined channels. In the case of premixed flame propagation, a constant volume combustion chamber with an aspect ratio of six (6) is used to study the propagation of laminar methane-air flame. This flame undergoes distinct changes in its topology during its propagation. Upon ignition with a spark plug, a spherical flamelet develops which rapidly grows in radius (surface area) and volume. This spherical flamelet grows faster in the axial direction, leading to the formation of a progressively more elongated "finger-shaped" flame. When the side-skirts of the finger flame come in contact with the cold wall, they extinguish and the flame area and flame speed both decrease rapidly. When the side-skirts near the leading edge, the flame flattens to a planar flame. An inward pointing cusp called the "tulip flame" is formed, which retains its topology until it is quenched wither by the cold wall or by collision with a flame that has been ignited on the opposite end. A detailed analysis of the flow-field is performed to study the influence of stagnation points, vortices and other flow features on the structure of the flame.

In order to study the propagation of diffusion flames over solid fuel in microgravity conditions, burn tests are usually performed in a drop-tower, to simulate microgravity levels comparable to those in space. Tests of longer duration, which are also cost-effective, can be performed on the earth using a Narrow Channel Apparatus (NCA), where the height of the channel is restricted to minimize or suppress the influence of buoyancy on the flame structure and its rate of propagation.

Oxidizer is supplied from the opposite side of the horizontal flame spread and the propagation is recorded using a video camera. The flame spread rate over a slab of Poly-MethylMethAcrylate (PMMA) is quantified for different slab thicknesses and opposed flow oxidizer speeds. The flame spread results obtained from the fourth iteration of Michigan State University's Narrow Channel Apparatus are compared with those obtained from microgravity tests to be performed at the International Space Station (ISS) in 2014 and will eventually be compared with ISS results in late 2016 or early 2017. The goal is to develop an earth-based testing system (the Narrow Channel Apparatus) that can be used to assess material fire safety for applications in space flight.

ACKNOWLEDGEMENTS

First and foremost, I would like to thank my advisor, Professor Indrek S. Wichman, who has guided and supported me throughout my graduate studies. I have been very fortunate to access to his vast knowledge on combustion physics and mathematics. I am greatly thankful for him giving me the freedom to choose my research project and helping me develop it further. His constant encouragement and ideas have helped me greatly in working towards my research goals.

I would like to thank Dr. Sandra Olsen at NASA Glenn Research Center and Dr. Fletcher Miller for their support in setting up the Narrow Channel Apparatus.

A special thanks goes to Professor Norbert Mueller, who has given me the freedom to work on investigation of flame propagation in combustion chambers while I was helping him develop the Wave Disk Engine. I have benefitted greatly by collaborating with his large team and have been able to understand and appreciate the challenges faced in transforming a computational design into a working experimental prototype.

I would also like to thank my dissertation committee members, Professors Elisa Toulson and Charles Petty for their valuable feedback on my research progress.

I would also like to thank all my co-workers and friends for the endless hours of discussion on a variety of topics and making graduate school a memorable experience.

Last, but not the least, I would like to thank my wife and family for their emotional and moral support during my graduate studies.

TABLE OF CONTENTS

LIST OF TABLES

LIST OF FIGURES

KEY TO SYMBOLS

S_L: Laminar flame speed

ρ: Density

δ: Reaction zone thickness

C_p: Specific heat, at constant pressure

λ: Thermal conductivity

$\dot{w}$: Reaction rate

α: Thermal diffusivity

Le: Lewis number

D_{th}: Thermal diffusion coefficient

χ: Euler characteristic number

V: velocity

τ: Viscous stress tensor

MW_i: Molecular weight of species i

k: Reaction rate constant

E_a: Activation energy

T: Temperature

INTRODUCTION

The primary research covered in this dissertation is the propagation of flames in confined combustion chambers. Two distinct types of flame types are studied –

(i) Premixed flames – The gaseous fuel and oxidizer are mixed at a molecular level to form a combustible mixture.

(ii) Diffusion flames – The fuel and oxidizer are not mixed, and combustion occurs only along an interface between the fuel and oxidizer, where mixing and reaction both occur.

The dissertation is divided into two parts. The first part (Chapters 1 through 6) deals with the study of premixed flame propagation in confined channels. The second part of the dissertation (Chapters 7) deals with the study of diffusion flame spread over a solid fuel in simulated microgravity conditions.

The study of premixed flames in confined channels has applications in automotive engines, mine safety and areas where a premixed fuel-air mixture is present in an enclosed chamber. The primary motivation to study premixed flame propagation for this dissertation has been for the development of the Wave Disk Engine (WDE), which is a rotary, constant volume combustor engine, described in detail by Iancu et al. (2008), Piechna (2006) and Vagani (2009) [see the references therein for older work]. The rotary wave disk engine project was funded by the US Department of Energy (US-DoE) and Advanced Research Projects Agency – Energy (ARPA-E) to investigate the use of high-speed rotary engines to increase fuel-economy and reduce emissions. A schematic image of the rotary wave disk engine is shown in Figure I.1.

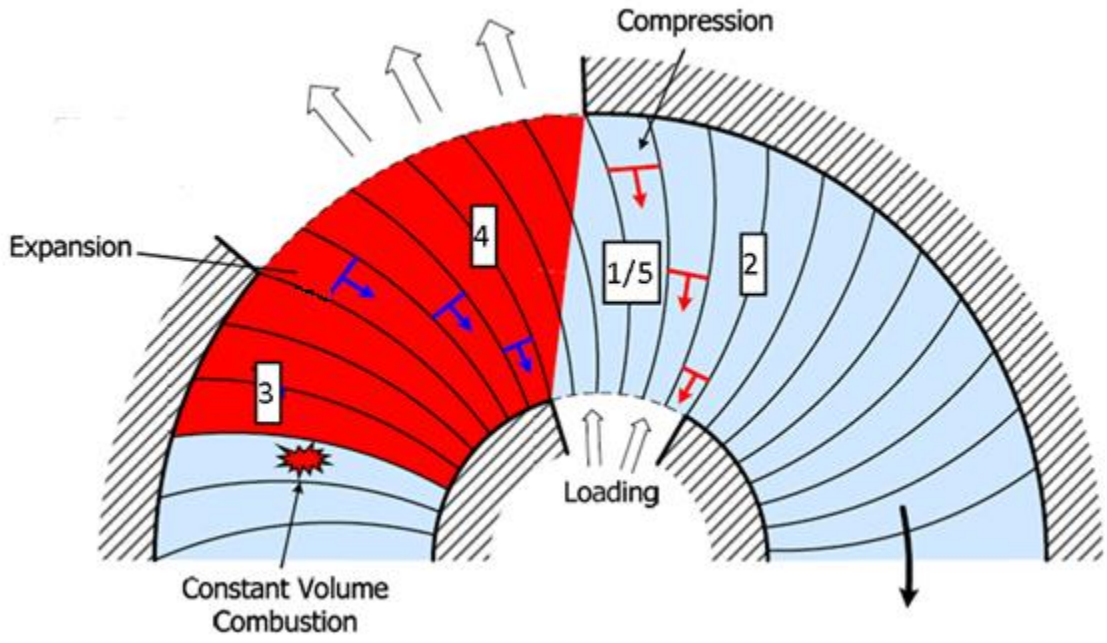

Figure I.1: Schematic representation of the rotary wave disk engine.

The wave disk engine is a radial rotary engine consisting of curved square cross-section channels with an aspect ratio of 6. To perform detailed study of the flame propagation, a combustion chamber with glass walls is constructed. For simplicity, this combustion chamber is not curved and is enclosed by aluminum walls for sealing. The combustion chamber is filled with stoichiometric methane-air mixture and ignited with spark plugs located at ends of the combustion chamber. The flame undergoes distinct changes in its topology during its propagation. A photo of the MSU combustion chamber apparatus is shown in Figure I.2.

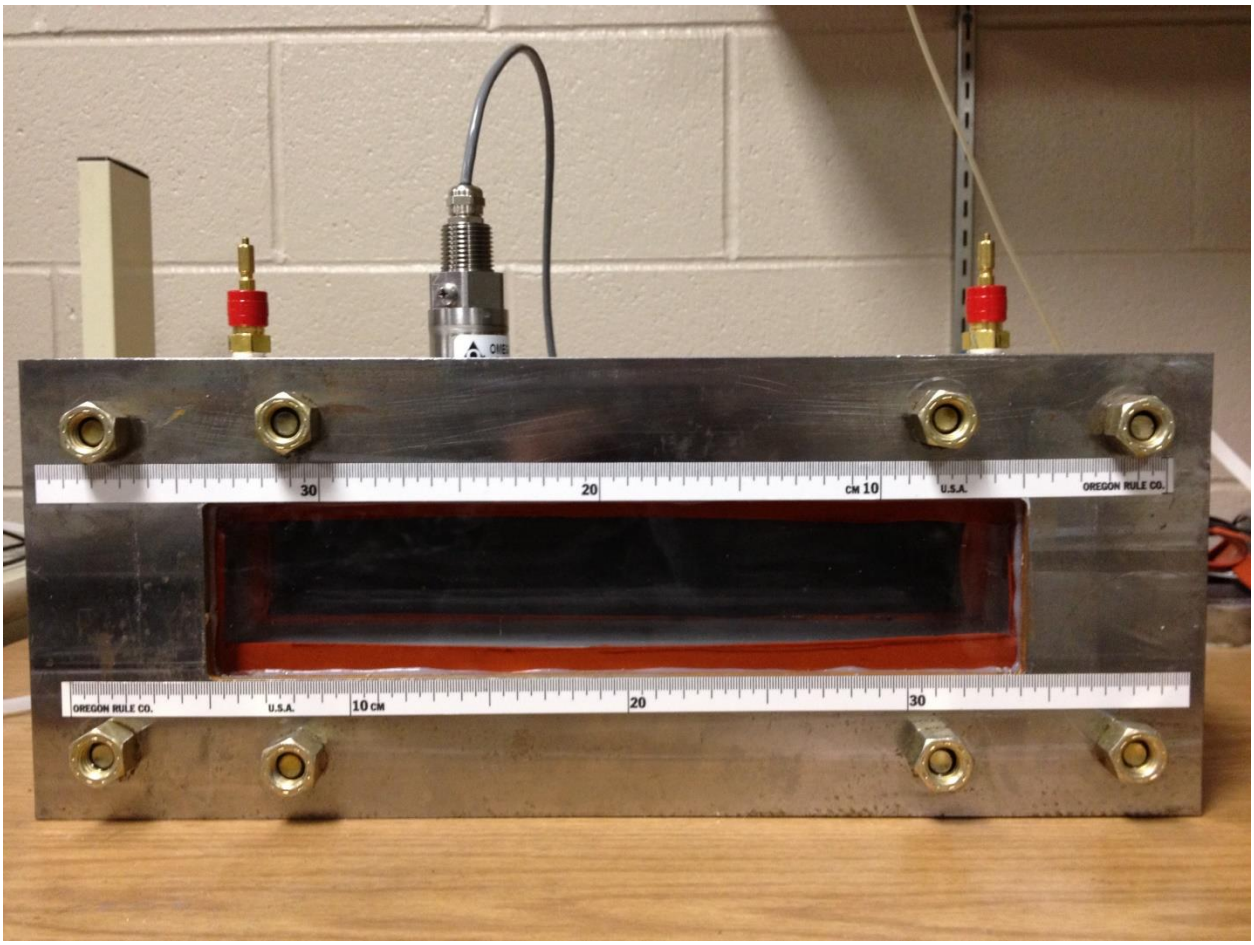

Figure I.2: MSU Constant-Volume (CV) combustion chamber apparatus.

Upon ignition with a spark plug, a spherical flamelet develops which rapidly grows in radius (surface area) and volume. This spherical flamelet grows faster in the axial direction, leading to the formation of a progressively more elongated "finger-shaped" flame. When the side-skirts of the finger flame come in contact with the cold wall, they extinguish and the flame area and flame speed both decrease rapidly. When the side-skirts near the leading edge, the flame flattens to a planar flame. An inward pointing cusp called the "tulip flame" is formed, which retains its topology until it is quenched wither by the cold wall or by collision with a flame that has been ignited on the opposite end. Figure I.3 shows the different topologies of the flame as it propagates along the length of the combustion chamber.

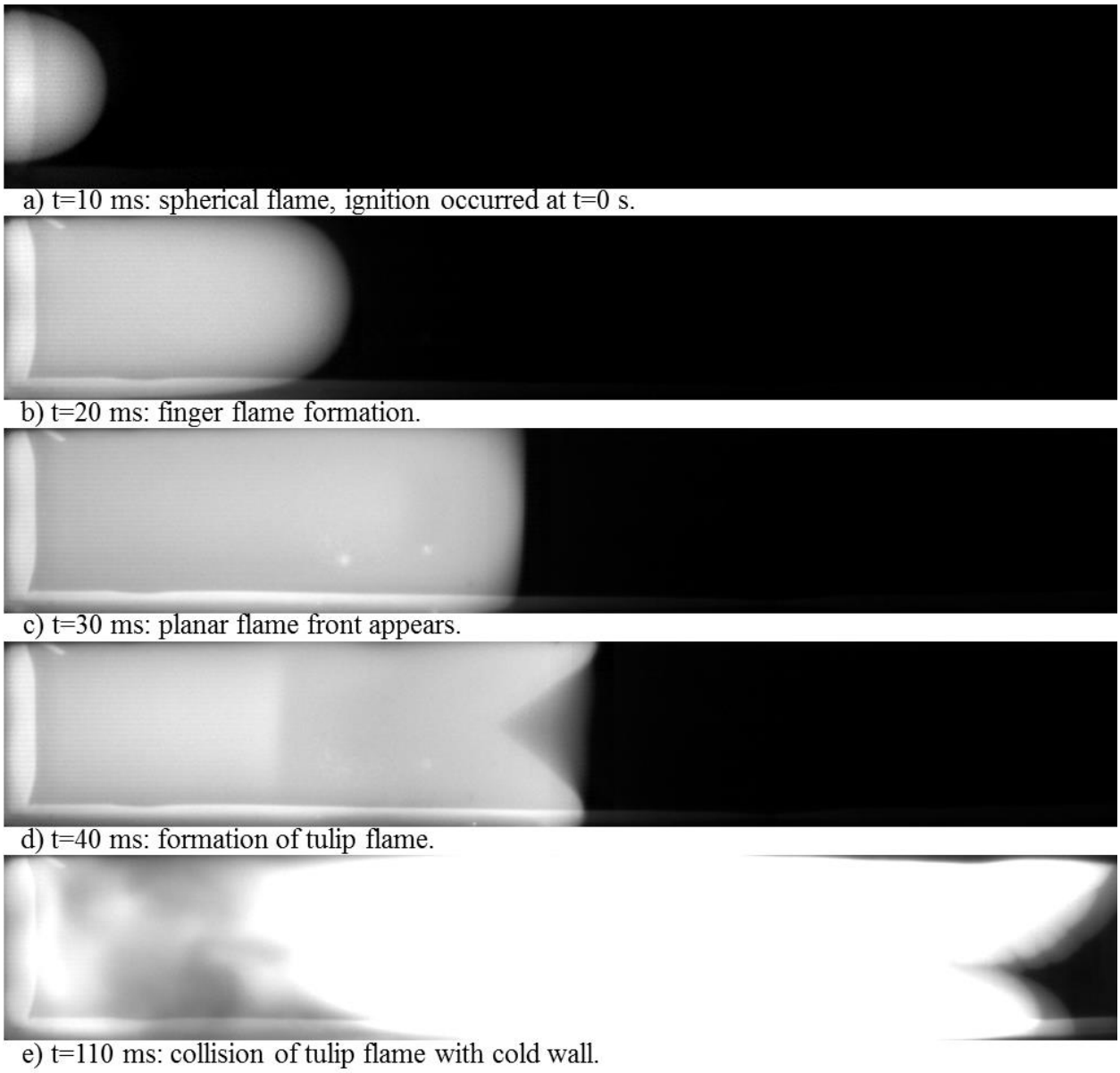

Figure I.3: Flame propagation along the combustion chamber, showing the different topologies. The fuel-air mixture is ignited by a single spark.

In this thesis, a detailed analysis of the flow-field is performed to study the influence of stagnation points, vortices and other flow features on the structure of the flame. Chapter 1 provides an introduction to premixed flames, and chapters 2 through 6 provide a detailed description of the experimental and numerical setup and results.

The study of microgravity diffusion flame spread has its primary applications in fire safety. The support structure and display panels of space habitats use combustible plastic materials, due to their low thermal/electrical conductivity and light weight and high strength. While the properties of flame spread over these plastics can be easily quantified for earth-gravity, the flame spread properties in microgravity are not readily available. The National Aeronautics and Space Administration (NASA) Glenn Research Center in Cleveland, Ohio studies microgravity flame spread through the Analysis of Thermo-diffusive and Hydrodynamic Instabilities in Near-extinction Atmosphere (ATHINA) initiative. The facility has a drop-tower, which can be used to study flame propagation in free-fall. The use of this drop-tower is both expensive and the free-fall microgravity environment lasts only between two to five seconds in total. Additionally, an aircraft flying in a parabolic trajectory has also be used. The aircraft, nicknamed the "vomit comet" typically provides about 30 seconds of microgravity during its descent phase. Similar to the case of the drop-tower, conducting tests on the aircraft is both expensive and provides only a maximum of 30 seconds of test time. The third method to test microgravity flame propagation is to use the Microgravity Science Glovebox, located aboard the International Space Station (ISS). This facility provides a true microgravity environment lasting several minutes. The experiment burn-time is constrained by the amount of oxygen available and the cost associated with sending samples to Low-Earth Orbit (LEO).

To simulate microgravity environment without using expensive methods (drop-tower, aircraft, space stations) and to provide a longer burn time, an apparatus was developed in which a solid fuel could be burned in a confined channel with its height small enough to suppress buoyancy effect, but not so small as to suppress the flame through heat loss to the walls. Versions of this apparatus are being studied in NASA Glenn Research Center, San Diego State University (SDSU) and at

Michigan State University (MSU). Each team's experimental apparatus has been designed slightly different and is intended for different purposes. This apparatus, called the "Hele-Shaw apparatus" does not provide a true zero-gravity environment, but simulates one by suppressing buoyant flow, and has the disadvantage of acting as a large heat-sink near the burning sample. However, it offers a longer test-time, easy interchangeability of test samples, varied sizes of samples, and can also be easily modified. A photo of the MSU Narrow Channel Apparatus is shown in Figure I.4.

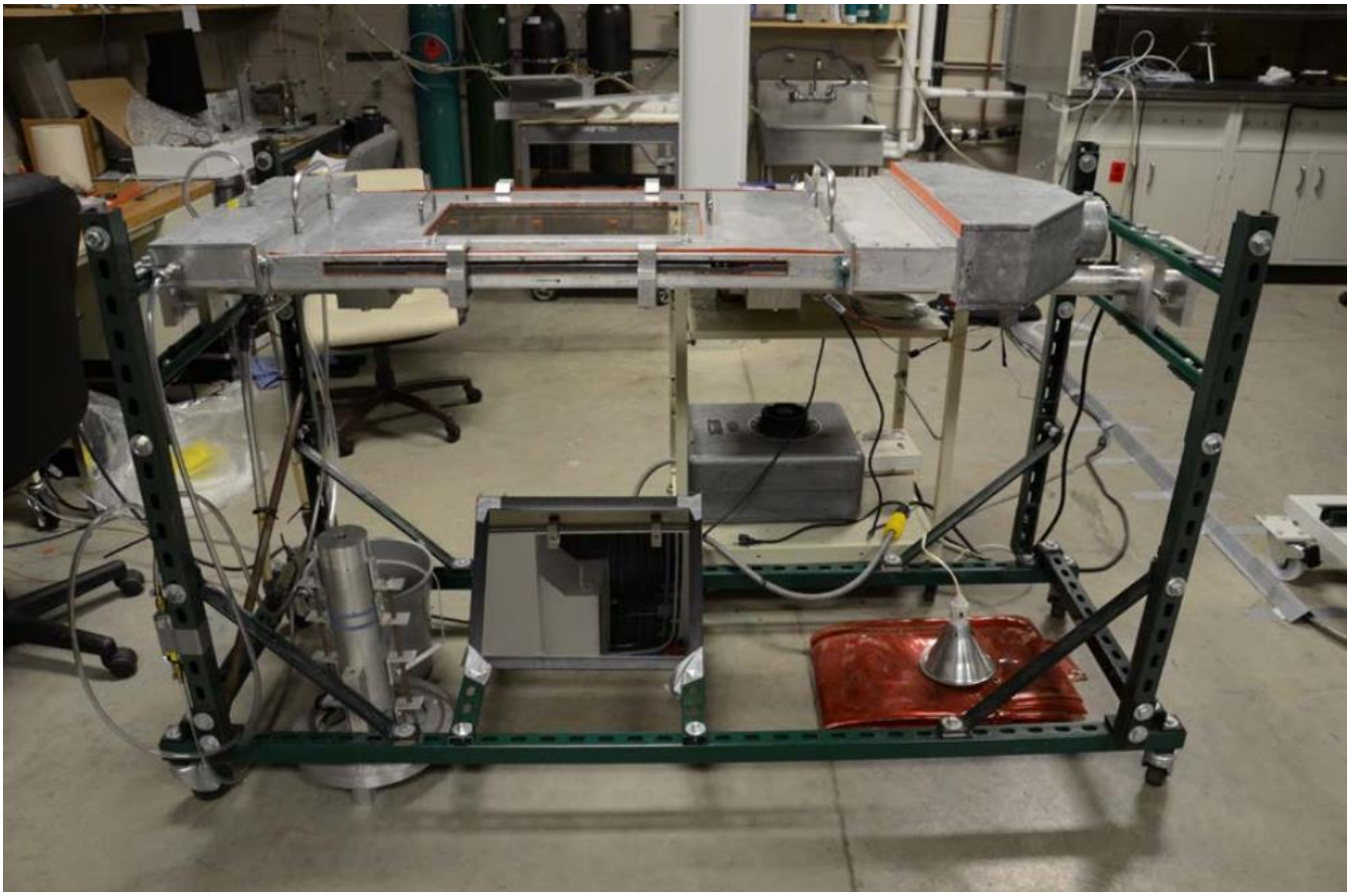

Figure I.4: MSU Narrow Channel Apparatus.

The apparatus has undergone progressive modifications over the years to refine the design and to also minimize unwanted airflow leak paths, heat loss to walls and to increase durability. The large sapphire-glass window on the top and sides offers a chance to optically record the flame spread using a video camera. This video is later post-processed to obtain the flame spread rate over the

solid plastic material. Ignition is achieved though Kanthal wires, and opposed flow of air is maintained by a mass flow meter connected to a pressurized air source.

The flame spread rate over a slab of PolyMethyl-MethAcrylate (PMMA) is quantified for varying opposed flow speeds and slab thicknesses. Three distinct regimes are observed for varying opposed flow speeds. These regimes are classified as follows – Normal Flame Spread, Flame Spread over Surface, and, Flamelet Regime. These three regimes are classified according to the type of flame spreading over the surface and also the shape of the burnt sample. Figure I.5 shows burnt samples with varying opposed flow speeds.

Figure I.5: Burnt PMMA samples with varying opposed air flow speeds.

In the above image, the air supply has been suddenly stopped to extinguish the propagating flame. This provides a method to visually investigate the profile of the sample being burnt. Typically, the entire depth of the sample is consumed (pyrolized) at high opposed-flow speed of air, and only the top surface is consumed at lower speeds. The flame shape also looks different depending on the

opposed flow speed and sample thickness. A detailed description of the experimental procedure and results is discussed in Chapter 7 of this thesis.

CHAPTER 1

PREMIXED FLAMES

A combustion system consists of two reactants, a fuel and an oxidizer. When these two reactants are mixed at the molecular level, the mixture is known as a premixed fuel-air mixture. Combustion in a premixed fuel-air mixture usually consists of a rapidly moving flame-front, which travels into the unburnt mixture with a finite reaction rate and at a characteristic speed. The two main classifications of premixed combustion, depending on their speed of propagation, are *deflagration* and *detonation*. When the flame-front propagates towards the unburnt mixture through the action of species and heat diffusion into the unburnt mixture and its speed of propagation is slower than the local speed of sound, it is called a *deflagration*. When the speed of flame propagation is faster than the local speed of sound, it is called a *detonation*. Detonation is sustained by the action of a shock wave just ahead of the flame-front, which causes the reactants to dissociate and recombine into products, which releases heat and further reinforces the shock.

The part of the reaction zone which releases thermal energy and (sometimes) light is called the flame. For a deflagration, the location and propagation of the flame-front in a premixed mixture is proportional to the reaction rate. A detailed and elaborate theory of deflagrations is available in the literature, although by no means can it be said that the subject of deflagrations is settled science. New ideas and techniques are constantly being developed for theoretical understanding and also for the numerical simulation of flames with detailed chemistry.

Premixed flames undergo numerous instabilities caused by the shape of the combustion structure, ratio of thermal and species diffusion rates, and intrinsic effects like the Darrieus-Landau

instability mechanism. A thorough discussion of these effects can be found in the notes of Clavin (1985).

Premixed flame propagation can be achieved in burners, and in open or closed channels. The flame structure can be defined by establishing a reference frame and defining a profile for the variables under consideration (temperature, species mass fraction). If the coordinate system is fixed to the moving flame front, the unburnt mixture will be seen approaching the flame-front with a speed equal to the flame speed, S_L. The spatial variation of the reactant concentration, temperature and reaction rate in this premixed, laminar flame-front is shown in Figure 1.1. The expansion ratio of the burnt gas is usually defined as σ, which is given here by ρ_u/ρ_b.

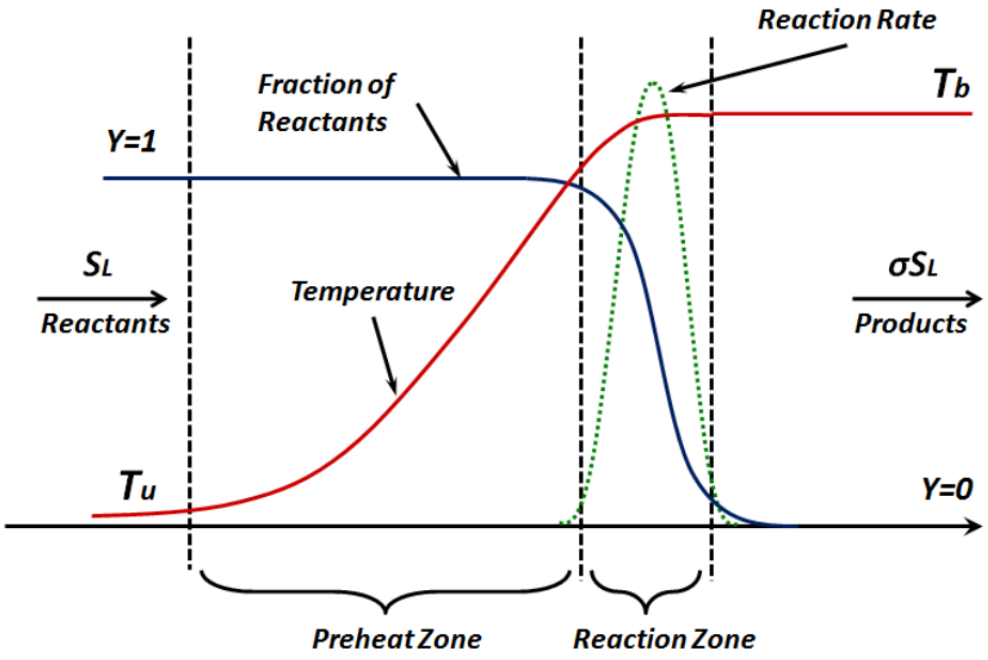

Figure 1.1: Structure of a premixed flame in one dimension. Figure adapted from Glassman (2007).

The two main zones are defined as preheat and reaction zones, dividing the flame-front into two regions, where the diffusion of heat and radicals occur at different intensities. In the preheat zone, the amount of heat released is very small and the reaction is practically negligible. As the observer moves closer to the reaction zone, the heat transported from the reaction increases, leading to a higher temperature and a faster reaction rate. The reaction occurs at a very thin zone (typically 1mm thick or less at atmospheric pressure). This region undergoes fast chemical reaction and due to the high reaction rate and heat release, the temperature and concentration gradients are very large. These large thermal and species concentration gradients drive the transport of energy and species into the upstream region known as the *preheat zone* and render the flame propagation process self-sustaining, as shown in Figure 1.1.

Laminar and Turbulent Premixed Flames

There are generally two types of premixed flames (deflagrations) depending on the nature of flow of the fluid: laminar and turbulent flames. The flow regime can be determined by the dimensionless number which is a function of flow velocity, kinematic viscosity, density and characteristic geometric dimension of the channel called the Reynolds number. In laminar flames, the combustion process, or flame propagation, is dominated by the chemical kinetics of the mixture: flame propagation occurs primarily through the mechanisms of diffusion of heat and chemical species. In turbulent flames, the velocity and scalar properties are subjected to rapid, random changes at a given point in space; therefore, the combustion process is strongly affected by it, in addition to the processes mentioned previously. The fluctuating temperature and species concentration caused by turbulence are the dominant forces influencing flame propagation in turbulent flames.

Combustion processes are characterized by highly exothermic chemical reactions, in which the reaction rate is a strong function of temperature. As mentioned previously, the combustion of a premixed mixture is strongly dependent on the chemical-kinetics of the mixture, thus the modeling of a detailed and accurate multi-step and multi-species reaction system represents a major challenge in the analysis of laminar flames.

Laminar Flame Speed

A detailed explanation is provided in this section for the propagation of a laminar flame through an unburnt mixture. First, a definition of laminar flame speed and laminar burning velocity is established. It is common to find ambiguities in the literature, in which laminar flame speed and laminar burning velocities are taken to have the same meaning, which is the velocity at which unburnt gas moves through the combustion wave in the direction normal to the wave surface.

These two flame speeds are defined below:

(i) The laminar burning velocity is defined as the velocity at which unburnt gases move through the combustion wave in the direction normal to the wave surface.

(ii) The laminar flame velocity is defined as the velocity of the flame with respect to a fixed outside observer.

In the case of a standing or stationary flame, like the flame in a Bunsen burner, the laminar flame velocity is equal to the laminar burning velocity. For example, the laminar flame velocity of methane-air and stoichiometric mixture at STP is 36.2 cm/s.

By contrast, for freely propagating flames, the laminar burning velocity is equal to the sum of the laminar flame speed and the flow velocity of the unburnt mixture. In this case one must carefully account not only for the intrinsic flame velocity (which depends on the local mixture conditions influencing thermal and mass diffusion) but also on the gas motion at each specific point in the mixture. This becomes a very complicated problem even in the simplified case of the propagation of an infinitesimally thin flame sheet.

The three main flame propagation theories are broadly classified as thermal, diffusion and comprehensive theories.

The first theory describing flame propagation was the thermal theory developed by Mallard and Le Chatelier (1883). They stated that the controlling mechanism of flame propagation is thermal diffusion from the burnt region to the unburnt region. This formulation defines the flame as a composite region comprising two zones, separated by a layer where ignition occurs. Ignition was postulated by Mallard and Le Chatelier (1883) to occur when the local temperature reached the ignition temperature and the quantity δ was described as the reaction zone thickness. This model is shown in Figure 1.2.

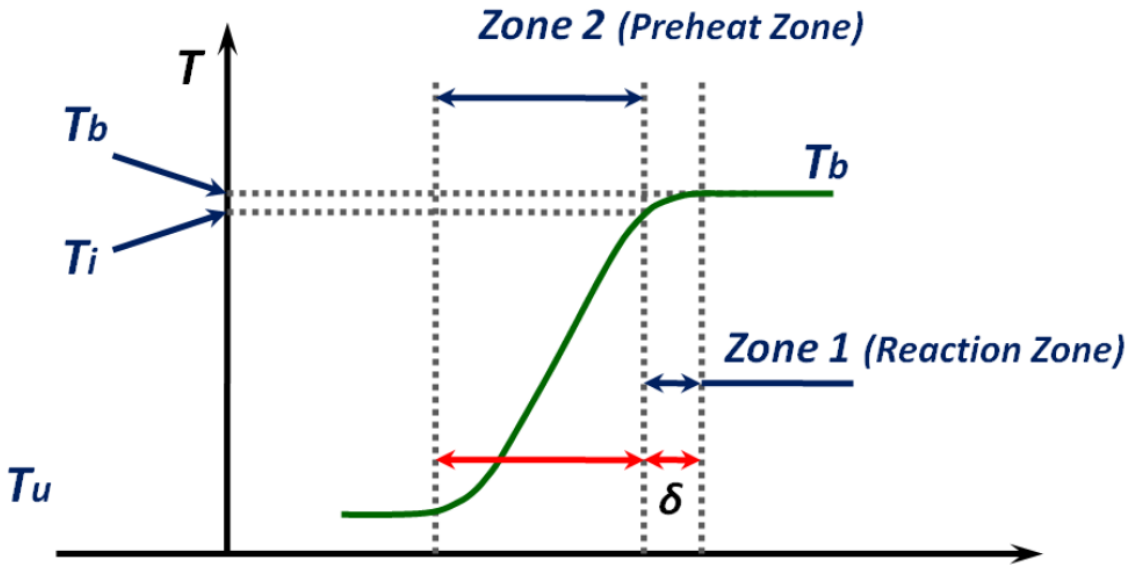

Figure 1.2: The Mallard and LeChatelier model. Figure adapted from Glassman (2007).

Improvements were made to the thermal energy model by Zeldovich and Frank-Kamenetskii (1938) more than half a century later. Their formulation included the diffusion of molecules and heat, but did not involve dissociation and the diffusion of free radicals. Tanford and Pease (1947) extended this theory further, stating that the mechanism for flame propagation depends only on

the diffusion of radicals and not on thermal diffusion as proposed in the earlier theories already mentioned.

These two theories of heat and radical diffusion drove the experimental research on the dependence of the flame velocity on the initial parameters, pressure and temperature, in order to examine the validity of the theoretical models of flame propagation. As is often the case, neither model was entirely correct.

Complicating matters still more, the basic problem of premixed combustion came to be viewed early in its history in two very distinct ways by two distinct types of scientists. In the one category were the chemists who tended to view combustion and flame propagation exclusively in chemical terms. These are the chemists, whose mindset and training reflected an exclusive emphasis on chemical reactions, reaction rate measurements and the relation of almost all problems of combustion to their origins in chemistry. Many of the older works in combustion reflect this philosophy. In the other category were physicists and applied engineers who were more comfortable with a field viewpoint, were not formally trained in chemistry, and who tended to view the flame front as a discontinuous "sheet" where chemistry happened, and heat was released, but whose detailed structure was of marginal importance to the far greater issue of mass consumption and burning rate. Many of the leading scientists in this camp came to combustion from fluid mechanics, where they had acquired great familiarity with the propagation of shock waves through gases: it was a simple extension of this theory to examine shock waves and discontinuous fronts with heat release: leaders in this approach included the afore mentioned Mallard and Le Chatelier, Rayleigh, and Prandtl and the German school (which contributed

mightily to the theory of shock waves and discontinuous fronts). The synthesis of these two schools of thought partially occurred when the fluid mechanicians began incorporating semi-realistic combustion models (Von Karman, etc.). However, in many respects the same fault lines exist in combustion to this very day.

The following observations follow from the two models of flame propagation –

- According to the thermal theory, increasing the initial pressure leads to a higher temperature. This leads to a faster rate of reaction and a higher flame speed in achieved.
- According to the diffusion theory, increasing the initial temperature leads to a higher rate of dissociation. The higher concentration of radicals produced by increased dissociation causes greater species diffusion leading to a higher flame speed.

A comprehensive theory combining the species and thermal diffusion theories was developed by Hirshfelder et al. (1954). A complex set of non-linear equations describing the diffusion and energy balance were developed that could be solved by numerical methods. The Arrhenius equation for the reaction rate, by definition, has a very small non-zero value at regions far upstream of the flame, where the local temperature is equal to the ambient temperature. This was modified to enable a zero reaction rate model at ambient temperature and considering the wall surface to act as a heat sink. The exact solution for laminar flame propagation requires the use of the fluid dynamics equations with modifications to accommodate heat release and species/thermal diffusion. The two theories are comprehensively discussed by Glassman and Yetter (2007). A brief review of the two theories is provided in the following section.

Mallard and Le-Chatelier Theory

The theory developed by Mallard and Le Chatelier states that the heat conducted from zone 1 in Figure 1.2 is equal to that required to raise the temperature of the unburnt mixture to the ignition temperature. The rate of temperature increase is assumed to be linear and is approximated to equal $[(T_f - T_i)/\delta]$. Here, T_f is the flame temperature, T_i is the mixture ignition temperature and δ is the reaction zone thickness.

The energy balance between the downstream inwardly convecting flow (i.e., into the flame front) and the upstream outwardly conducting thermal energy (i.e., into the unburned mixture ahead of the flame front) is given by the simple relation –

$$\dot{m}C_p(T_i - T_u) = \lambda(T_f - T_i)/\delta A. \qquad 1.1$$

Here, λ is the thermal conductivity of the mixture, $\dot{m}$ is the mass flow rate of the unburned gases into the combustion wave, T_u is the temperature of the unburnt gases and A is the cross sectional area of the flame segment under consideration. The combustion wave is considered to be one dimensional.

From the continuity equation, we have, for the steady mass flow rate, the expression

$$\dot{m} = \rho UA = \rho S_L A. \qquad 1.2$$

Here, ρ is the density and U is the velocity of the unburnt gas, which is equal to the laminar flame speed, S_L.

Upon using the mass balance equation with the energy balance, we obtain the result

$$\rho S_L C_p(T_i - T_u) = \lambda(T_f - T_i)/\delta \ . \qquad 1.3$$

Solving for the flame speed, we obtain:

$$S_L = \frac{\lambda(T_f - T_i)}{\rho C_p (T_i - T_u)} \frac{1}{\delta} \qquad 1.4$$

For a steady flow condition, the total mass rate entering the reaction zone must be equal to the rate of consumption of the reactants, thus:

$$\frac{\dot{m}}{A} = \rho U \rightarrow \rho S_L = \dot{w}\delta \ . \qquad 1.5$$

In Equation 1.5, ẇ represents the reaction rate in terms of the concentration of the reactants. Using this expression in the flame speed equation yields –

$$S_L = \left[\frac{\lambda(T_f - T_i)}{\rho C_p (T_i - T_u)} \frac{\dot{w}}{\delta} \right]^{\frac{1}{2}} \Rightarrow \left[\alpha \frac{\dot{w}}{\rho} \right]^{\frac{1}{2}} \qquad 1.6$$

Where, α is the thermal diffusivity. From the expression above, we obtain an expression for the mass consumed by the unburnt gas:

$$\rho S_L \approx \left[\frac{\lambda}{C_p} \dot{w} \right]^{\frac{1}{2}} . \qquad 1.7$$

Thus, the Mallard-Le Chatelier approach therefore yields the following result for the laminar flame speed:

$$S_L = const \times \left[\alpha \frac{\dot{w}}{\rho} \right]^{\frac{1}{2}} \ . \qquad 1.8$$

Equation 1.8 enables the estimation of laminar flame propagation speed for changes in the physical and chemical parameters. We note that in this analysis, the chemical variables appear implicitly in $\dot{w}$.

A similar approach was used by Linan and Williams (1994) based on Mikhelson's studies (1989) where the heat release in the reaction zone is equated to the energy conduction from the hot products to the cool unburnt gases. In this approach the total energy per unit mass that is conducted to the unburned mixture is given by

$$h = C_p (T_f - T_u). \tag{1.9}$$

The energy balance is calculated as

$$h\dot{w}\delta_L = \lambda(T_f - T_u)/\delta_L \tag{1.10}$$

where δ_L is the thickness of the reaction zone, which includes both region 1 and region 2 from the Mallard-Le Chatelier approach (see Figure 1.2). Combining the energy balance equations gives

$$C_p(T_f - T_u)\dot{w}\delta_L = \lambda(T_f - T_u)/\delta_L \quad . \tag{1.11}$$

Solving the above equation for the reaction zone thickness leads to

$$\delta_L = \left[\frac{\lambda}{C_p}\frac{1}{\dot{w}}\right]^{\frac{1}{2}} \tag{1.12}$$

Using Equation 1.5 derived earlier, we obtain:

$$S_L = \left[\frac{\lambda}{\rho C_p}\frac{\dot{w}}{\rho}\right]^{\frac{1}{2}} = \left[\alpha\frac{\dot{w}}{\rho}\right]^{\frac{1}{2}} \tag{1.13}$$

The expression derived above is the same as that derived by Mallard-Le Chatelier, but this derivation does not employ the ratio between the ignition temperature and initial/final temperature. In the Zeldovich, Frank-Kamenetskii and Semenov theory, the reaction zone acquired nominal structure. In this theory, which assumes an asymptotically narrow reaction rate region, the following expression appears in the exponential of the Arrhenius reaction rate term:

$$\frac{RT_f^2}{E(T_u - T_f)}. \qquad 1.14$$

This term was identified as the Zeldovich number, and is defined as

$$Ze = \frac{RT_f^2}{E(T_u - T_f)} = \frac{\delta_L}{\delta} \ . \qquad 1.15$$

Because *Ze* appears in the Arrhenius exponential and because it is generally large (of order 10), the chemical reaction term is extremely sensitive to changes in this parameter. In other words, it is one of the dominant parameters of combustion.

The expression for the laminar flame speed is now be derived as

$$S_L = \left[\frac{\alpha}{Ze}\frac{\dot{w}}{\rho}\right]^{\frac{1}{2}} \qquad 1.16$$

This expression allows a reasonably accurate global analysis of the flame speed with respect to changes in both the physical (fluid dynamic) and chemical parameters of the problem. We find that the reaction term is proportional to the pressure of the reactants according to

$$S_L \approx (P^{n-2})^{\frac{1}{2}}. \qquad 1.17$$

Here, n is the overall order of the reaction.

The laminar flame speed's dependence on the temperature is mainly dictated by the exponential in the rate expression w. This gives the expression:

$$S_L \sim \left[\exp(-E/RT_f)\right]^{\frac{1}{2}} \qquad 1.18$$

We note that the maximum reaction rate and heat release takes place close to the highest temperature if Arrhenius kinetics is indeed the controlling factor in the description of the flame chemistry.

Zeldovich, Frank-Kamenetskii and Semenov Theory

The analytical model of flame propagation suggested by Zeldovich, Frank-Kamenetskii and Semenov, serves as a more detailed method to determine the flame propagation speed. This model combines both the effect of thermal diffusion and the diffusion of species into the unburnt mixture on the flame speed. This model ignores the influence of the diffusion of chemical radicals and their effect on reaction rate.

The main underlying assumption in this model is that the ignition temperature is very close to the flame temperature. The ignition temperature is defined as the threshold temperature above which most of the reaction occurs. In addition, the specific heat and thermal diffusivity are both assumed to be constant over the entire flame region. This enables the use of the Lewis number, which is the non-dimensional ratio of the thermal and mass diffusion coefficients. When the rate of thermal and mass diffusion is identical, the Lewis number is unity. A detailed discussion of the influences of the Lewis number in premixed flames can be found in the book by Law (2006).

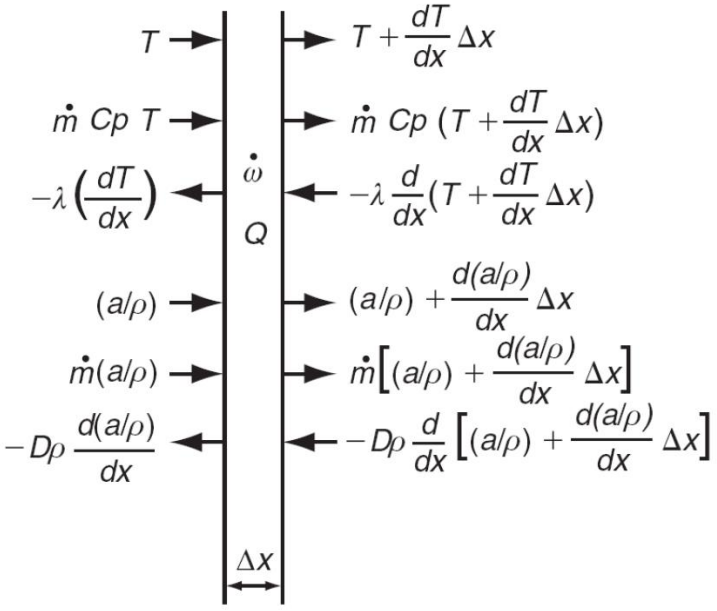

Figure 1.3: Balances across a differential element of laminar flame. Figure adapted from Glassman (2007).

From Figure 1.3 the flame is assumed to be a one-dimensional slice of thickness Δx. Here, 'a' is the mass of reactant per cubic meter, w is the rate of reaction and Q is the heat of reaction per unit volume. Since this is a steady propagation process, there is no accumulation of species or heat within the volume shown in Figure 1.3. The equations of mass balance, mass diffusion and energy balance equation are formulated within the limits of the unburnt and burned gases from $X = -\infty$ to $X = +\infty$. The combustion wave is considered to consist of two parts. The unburnt part in which there is no reaction and the reaction part in which the reaction and diffusion processes dominate and the convective term is neglected. In this theory, the inclusion and/or neglect of the various terms is intuitive since there is no justification provided for these approximations. The energy equation is centered at x = 0, which allows the local temperature at the origin to be specified as the ignition temperature.

Upon integration of the system of equations, the solution for the flame speed is obtained as follows:

$$S_L = \left[\frac{2}{a_0} \left(\frac{\lambda}{\rho_o C_p} \right) \left(A e^{-E/RT} \right) \left(\frac{RT_f^2}{E(T_f - T_0)} \right) \right]^{\frac{1}{2}} \qquad 1.19$$

Here, A is the pre-exponential factor in the Arrhenius equation and the subscript '0' refers to the initial conditions.

Flame Speed Measurements

Depending on the method of measurement and the accuracy requirement, the measurement of flame speed can be simple or complicated. Flat, adiabatic flames are difficult to obtain in the laboratory due to heat losses and gravity, hence the most common flame shapes are either conical or spherical, or, in the case of flames in tubes, they tend to become distorted fronts leaning further upstream further upward along the front. The most common methods used in the calculation of flame speeds are by Bunsen burner, cylindrical tube, spherical flame and the flat flame burner methods. These are discussed in detail below.

Bunsen Burner Method

In a Bunsen burner with long tubes, the velocity profile at exit is parabolic, leading to a variable burning velocity over the flame surface. For this case, an average method is used to determine the normal velocity component, U_n over the "flame cone" that the Bunsen burner flame produces. The normal velocity U_n is equal to the flame speed S_L. It is assumed that U_n is constant over the flame area A_f. If m is the mass flow rate of the gas, and ρ is the unburnt gas density, from mass continuity, we obtain:

$$U_n = \frac{\dot{m}}{\rho_u A_f} \qquad 1.20$$

When suitably shaped nozzles are used, the flow is uniform and the flame has straight edges. The flame speed can then be computed as:

$$U_n = U_u \sin \alpha_u \qquad 1.21$$

The structure of the flame in a Bunsen burner is shown in Figure 1.4. This method is not accurate, in general.

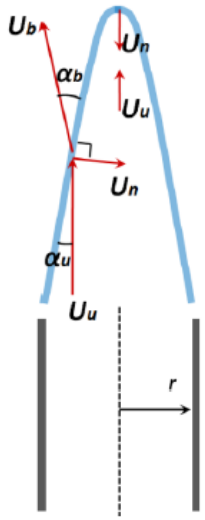

Figure 1.4: Bunsen burner flame. Figure adapted from Glassman (2007).

Cylindrical Tube Method

This method utilizes a cylindrical open tube, typically made of glass, sometimes quartz, where the premixed fuel-air mixture is ignited at the open end. The speed of flame propagation is measured optically. Due to buoyancy effects, the flame shape is not planar, thus the area of the flame is larger than the cross-sectional area of the tube. The combustion induces pressure waves which travel faster than the flame and induce a localized velocity in the unburnt mixture which can alter the speed of propagation of the flame front with respect to the laboratory coordinates. Additionally, heat losses to the walls of the tube can influence the flame speed as the non-quenched region mixes with the quenched region of the flame. Of course, this configuration is also subject to gravitational effects, which are somewhat circumvented by orienting the tube vertically and igniting at the top. Igniting the mixture below will, of course, produce a front with low density (burned gas) beneath high density (unburned gas) which is thermally unstable.

Spherical Flame Method

In this method, the premixed mixture is contained in a soap bubble and is ignited at the center, so that the flame propagates radially through the unburnt mixture. Since the gas is enclosed by the

soap film, the pressure remains constant. There is no heat loss to the outside since the soap bubble contains no heat sinks. The bubble grows as the premixed mixture burns: this rate of growth is measured optically. The flame speed can be measured as follows:

$$S_L = U_n\left(\frac{\rho_b}{\rho_u}\right) \qquad 1.22$$

Flat Flame Burner Method

This method of flame speed measurement is performed by supplying a combustible gas mixture to a series of thin, parallel tubes of diameter not larger than 1 mm. The mixture flow rate is adjusted to produce a thin flat flame resting on top of the burner surface. The flame speed is obtained by dividing the volumetric flow rate with the flame area. Since the flame is perfectly flat, it is the most accurate method of measuring the flame speed of a fuel-air mixture.

An excellent physically based discussion of these and other methods of flame speed measurement are provided in the classical book of Gaydon and Wolfhard (1979) which, despite its age, is an outstanding summary of the relevant experimental approaches to flame measurement.

Instabilities in Flame Propagation

Combustion in both open and closed channels is subjected to a number of instabilities which have been studied theoretically, computationally and experimentally. The three main types of instabilities which have the greatest impact on flame structure and propagation are listed below:

(i) The Landau-Darrieus instability, an intrinsic instability which occurs due to hydrodynamic effects. In essence, it can be shown that a flat, infinitesimally thin front, or flame sheet, is unstable to small perturbations.

(ii) Instability caused by the coupling of combustion and acoustics of the system. These instabilities are characterized by low-frequency oscillations in the longitudinal dimension of the channel.

(iii) Instability caused due to the coupling between combustion and specific acoustic modes. These instabilities are characterized by high frequency oscillations in the transverse dimension of the channel.

The last two types of instabilities are commonly classified as thermo-acoustic instabilities and the first one is referred to as a hydrodynamic instability. The three instabilities are discussed in great detail by Searby (2009) and by Law (2006). A short description is provided in the following section.

Landau-Darrieus Instability

All premixed flames are intrinsically unstable due to the hydrodynamic effects, which is caused due to the expansion of hot, combusted gas into the denser, unburnt mixture. A one-dimensional representation of an infinitesimally thin laminar flame is shown in Figure 1.5. The planar flame front is essentially a thin interface (a sheet) which separates the unburnt and burnt gases. The cold reactant gases at temperature and density, T_0 and ρ_0, are separated from the hot combusted gases of temperature and density, T_b and ρ_b. The flame front propagates at velocity S_L into the unburnt gas mixture. Upon combustion, the gases undergo thermal expansion and they exit the flame front at $U_b=S_L.(\sigma)$. The density ratio (σ) is almost equal to the temperature ratio for standard hydrocarbon fuels, since the pressure is nearly constant across deflagrations, i.e., $P_0 \sim P_b$.

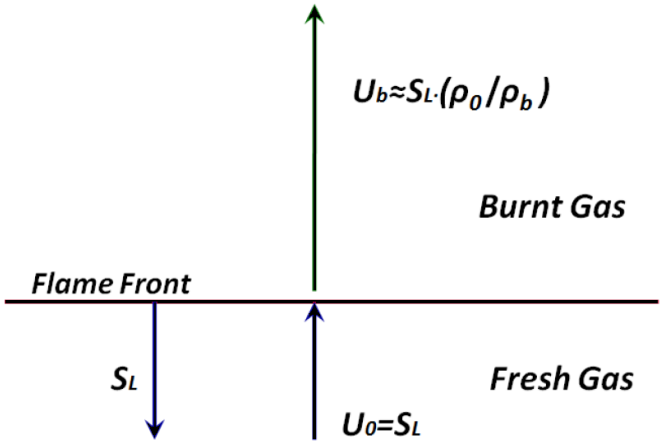

Figure 1.5: Propagating flame front.

To conserve the momentum, the velocity jump must be accompanied by a small increase in pressure which is typically around 1 Pascal, given by:

$$\delta P = \frac{1}{2}.\left(\rho_b U_b^2 - \rho_o U_o^2\right) \equiv \frac{1}{2}.\left(\rho_0 S_L^2\right)\left(\frac{\rho_o}{\rho_b} - 1\right) \qquad 1.23$$

When the flame front is inclined with respect to the axis of propagation, as shown in Figure 1.6, the propagation of the exhaust gases changes to conserve momentum.

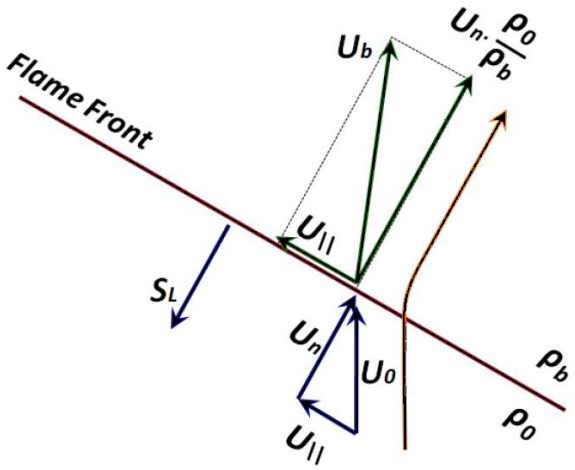

Figure 1.6: Inclined flame-front. Figure adapted from Glassman (2007).

The incoming flow of the premixed fuel-air mixture can be decomposed into vector components which are parallel and normal to the flame front as U_{ll} and U_n, respectively. If the flame front is the reference frame, then normal component of the incoming premixed mixture must be equal to the flame velocity, so that $U_n=S_L$. The burnt gas leaving the flame front will have a normal component equal to $U_n(\rho_o/\rho_b)$ (thermal expansion). The parallel component of the flow remains unchanged as there is no physical mechanism to sustain the parallel pressure jump that would be necessary to accelerate the parallel component of the flow. Upon vector addition of the parallel and normal components, the resultant vector direction now deviates from the outgoing normal. This causes the flow to change its direction after passing through the combustion wave if it is not perfectly normal to the flame-front sheet. Much of this discussion is essentially identical to the consideration of the flow structure across an idealized shock wave.

Consider now a flame which is not exactly planar, but is wrinkled at a wavelength λ, as shown in Figure 1.7. At the localized places where the streamlines are exactly normal to the flame-front, they are accelerated, but do not deviate, when they cross the flame. At places where the flame-front is inclined to the incoming mixture, the streamlines deviate to the rear normal of the flame

front. Although the streamlines in Figure 1.7 are locally correctly depicted, streamlines in a flow cannot cross each other and so they must curve to become parallel in the far downstream as shown in Figure 1.8.

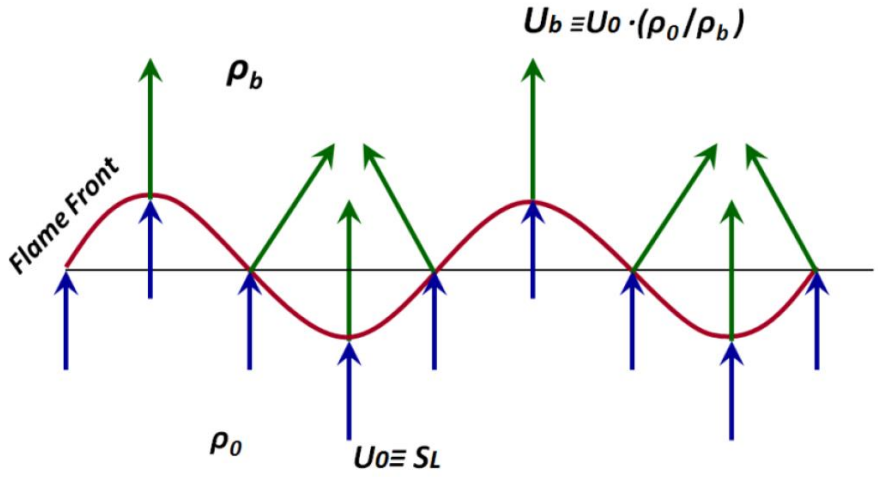

Figure 1.7: Local streamline deviation in a wrinkled flame. Figure adapted from Glassman (2007).

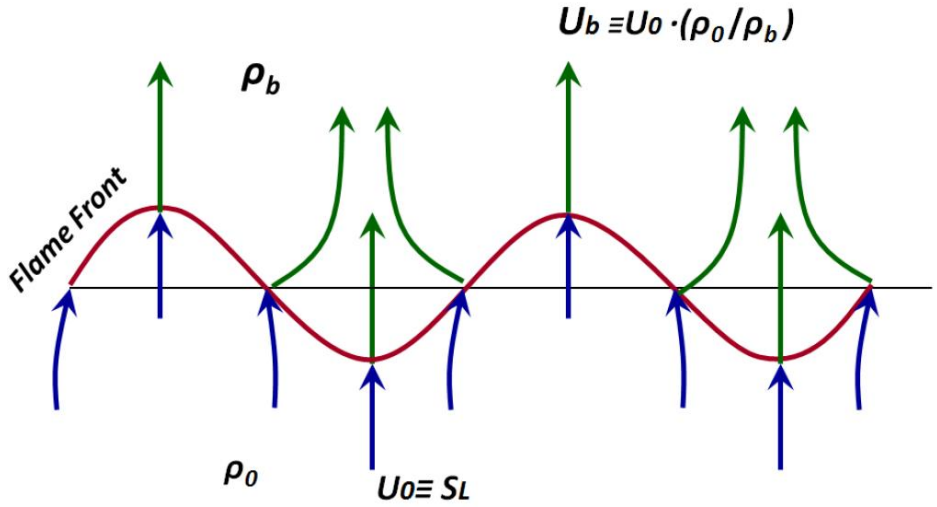

Figure 1.8: Global streamline deviation in a wrinkled flame. Figure adapted from Glassman (2007).

When the streamlines are curved, there are pressure gradients along the flow. This introduces perturbations which are not local. This non-locality of the presence of flame-induced pressure

gradients will not only alter the downstream flow, but also the upstream flow. This causes the gas expansion through a curved flame to converge at locations where the flame-front is concave and to diverge where the flame-front is convex, as shown in Figure 1.8. Due to mass conservation, the upstream flow is either accelerated or decelerated where the flame front lags behind or is ahead of the mean position, respectively. Since we have assumed that the propagation velocity is constant, the flame front becomes unconditionally unstable and the wrinkling will only grow with time, there being no physical process (or processes) in this model to oppose it.

Thermo-Diffusive Instability

The Zeldovich-Frank-Kamenetskii model of premixed flame propagation has high activation energy. For this reason, the chemical reactions are confined to a thin layer on the high-temperature side of the flame front. The mechanism of flame propagation is primarily influenced by the diffusion of the heat and species within the flame, whose thickness is δ. In the case of a curved or wrinkled flame-front, the gradients of temperature and species concentration are not parallel to the average direction of flame propagation and therefore the local flame velocity can change.

At a location where the flame-front is concave towards the unburnt mixture, the heat flux is locally convergent. As a consequence of this, the local flame temperature and the local propagation velocity increase. At a location where the flame-front is convex towards the unburnt gas, the heat flux is locally divergent. The result is that the local flame temperature and the local propagation velocity decrease. The influence of increased thermal diffusion is to stabilize the wrinkled flame.

The gradient of the thermal diffusion is shown by the blue arrows whereas the gradient of species concentration is shown by the green arrows in Figure 1.9. It can be seen that the species gradient and the thermal gradient point in opposite directions. At a location where the flame-front is concave towards the unburnt mixture, the species flux is locally divergent and thus the flux of reactive species into the reactive zone decreases leading to a decrease in the local propagation velocity. The influence of species diffusion is to destabilize a wrinkled flame. The net result of these two diffusive fluxes will depend on the ratio of the thermal and species diffusion coefficients, called the Lewis number:

$$Le = D_{th}/D_{mol} \qquad 1.24$$

If the Lewis number is greater than unity, the influence of thermal diffusion is dominant over species diffusion, hence the flame is thermo-diffusively stable, meaning the tendency towards

wrinkling is suppressed. There is, however, an additional stabilizing contribution that arises from the inclination of the streamlines within the preheat zone. This internal inclination of the streamlines creates an additional transport of heat and species that is convergent or divergent with respect to the average direction of propagation. It has the effect of contributing an additional term in the expression for the flame velocity. This term is always stabilizing, independent of the Lewis number, and it increases with the gas expansion ratio.

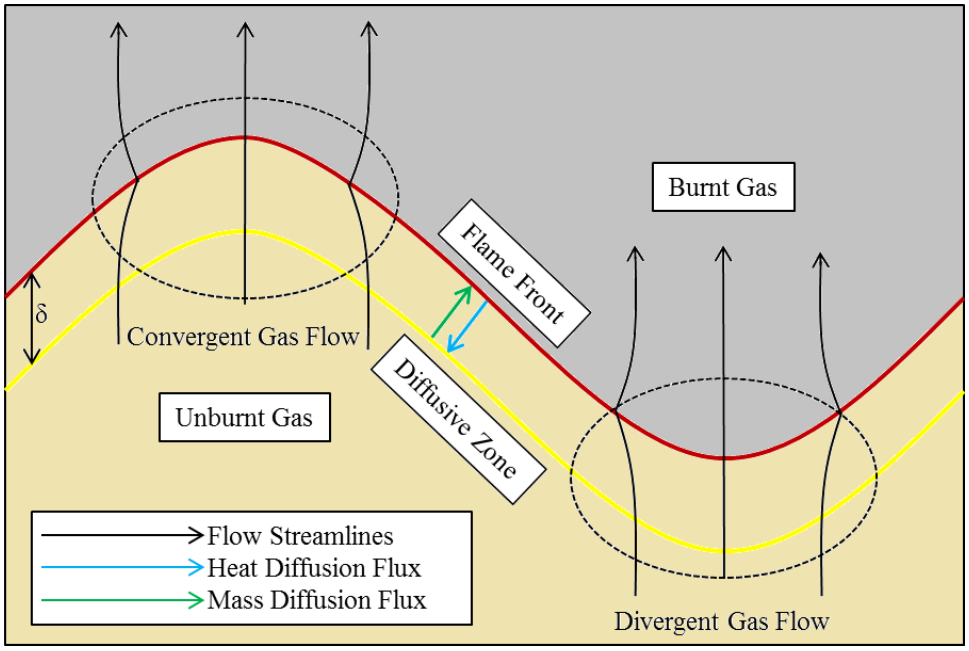

Figure 1.9: Wrinkled premixed flame structure. In the concave region of flame where the convergent gas flow prevails, the streamlines move closer together as shown. Here, the diffusion and mass flux are both divergent, while the upstream heat flow is convergent. Figure adapted from Glassman (2007).

Thermo-Acoustic Instability

Combustion in a constant volume chamber generates acoustic waves that can interact with the flame front and cause perturbations in the flames. These acoustic waves are usually reflected off of enclosing walls and internal obstacles. Instability mechanisms that produce such perturbations have been studied under different experimental conditions. Thermo-acoustic instabilities usually manifest themselves as flame distortions leading to increased flame surface area, increased flame propagation speed and peak pressure enhancement. Lining the combustion chamber walls with materials that absorb acoustic waves or using obstacles to deflect the acoustic waves can help to reduce the intensity of these acoustic instabilities.

Unsteady combustion is a strong source of acoustic noise, whose emission is governed by the conservation equations given by:

Mass Conservation:

$$\frac{D\rho}{Dt} + \nabla.\rho V = 0 \quad . \tag{1.25}$$

Momentum Conservation:

$$\rho\frac{DV}{Dt} = -\nabla p \quad . \tag{1.26}$$

Energy Conservation:

$$\rho C_p \frac{DT}{Dt} = \dot{q} + \frac{D\rho}{Dt} + \nabla.(\lambda\nabla T) \quad . \tag{1.27}$$

Equation of State:

$$\frac{P}{\rho} = \left(C_p - C_v\right)T = \frac{C_v}{C_p}a^2 \quad . \tag{1.28}$$

Here, D(·)/Dt is the material derivative, V is the gas velocity vector and *a* is the local speed of sound.

Combining the energy conservation and the equation of state, we obtain:

$$\frac{Dp}{Dt} = a^2 \frac{Dp}{Dt} + \left(\frac{C_p - C_v}{C_v} \right) \dot{q} \quad . \qquad 1.29$$

When an acoustic wave interacts with a flame-front, the heat released by chemical reaction will be a function of the acoustic pressure magnitude. This phenomenon was described by Rayleigh (1878) as follows –

> "If heat is periodically supplied and removed from a mass of vibrating air, the effect produced will depend on the phase of vibration. If the heat is supplied at the moment of highest condensation and removed at the moment of highest rarefaction, the application of heat would lead to a support of the vibration."

The Rayleigh criterion states that positive energy is transferred to the acoustic wave if the pressure and heat release fluctuations are in phase. By contrast, negative energy is transferred to the acoustic wave if the pressure and heat release fluctuations are out of phase.

The two major types of coupling between an acoustic wave and the combustion process are pressure coupling and acceleration coupling, which are discussed in greater detail below.

Pressure Coupling

The standard form of the chemical reaction rate in the Zeldovich-Frank-Kamenetskii model (1938) using Arrhenius law is described below:

$$\Omega = A\rho Y^{\frac{-E_a}{RT}} \quad . \qquad 1.30$$

Here A is the pre-exponential factor, Y is the mass fraction of the limiting reactant, E_a is the activation energy and ρ is the reactant density.

According to the above expression, the reaction rate is directly proportional to the density of the reactants. Since the reactant density is proportional to its pressure if the reactants obey ideal gas law, this leads to a variation in the reaction rate with changes in density caused by the pressure waves (which leads to reaction/acoustic coupling). The propagation of acoustic waves also causes an increase in the local temperature because an acoustic wave is largely adiabatic, which implies that any local increments of heating are retained in the mixture to increase local temperatures. For reactions with high activation energies, the heat release is primarily sensitive to the temperature oscillation that is produced by the acoustic waves.

The coupling of acoustic pressure waves and the chemical reaction depends on the acoustic frequency, the velocity and the Lewis number of the reactant. The use of the one-step Arrhenius equation to model the reaction leads to a mismatch between the theoretical results and experimental investigations performed on planar methane-air flames subjected to acoustic oscillations. In other words, the one-step chemical reaction does not seem capable of modeling the details of the acoustic-reaction coupling.

Acceleration Coupling

The local velocity field in an acoustic wave imparts a localized acceleration to the flame front, which leads to a change in the reaction rate. The flame-front is also influenced by other acceleration fields such as gravity due to the differences in the densities of the fluids separated by the flame-front. One of these influences was previously mentioned, namely the upward propagating flame in a glass (quartz) tube, which is an unstable configuration.

When the localized velocity of the pressure wave is oriented towards the unburnt mixture, the size of the reaction cell will increase. When the localized velocity of the pressure wave is oriented towards the burnt mixture, the size of the reaction cell will decrease. The total reaction rate of the

combustion process is directly proportional to the average size of the reaction cell, hence the acceleration coupling between the flame-front and pressure wave exerts a major influence on the reaction rate of the flame.

CHAPTER 2

PREMIXED FLAMES IN CONFINED CHANNELS

Premixed flame propagation in confined channels was first studied to investigate accidental ignition and subsequent propagation of fires in coal mines, which typically had a methane-rich atmosphere. The first observation of flame propagation in tubes was reported by Mallard and Le Chatelier (1883). Later, photographically documented study of premixed flame propagation in closed tubes was carried out by Ellis (1928). In this pioneering work, Ellis studied the propagation of premixed methane-air flames in circular tubes, and in particular, the transition in flame shape from an outward pointing (or concave to the burnt gas) flame front to an inward pointing flame cusp, for tube area ratios of greater than two. This inward pointing flame cusp was called a "tulip flame" by Salamandra et al. (1959). Subsequently, several detailed experiments were performed for half-open tubes by Clanet and Searby (1996) and closed tubes by Starke and Roth (1986), Guenoche (1964) and Dunn-Rankin et al. (1988). The image of the formation of a tulip flame is shown in Figure 2.1, taken from Clanet and Searby (1996). The image is a superimposition of three images, showing the distinct topologies associated with flame propagation in confined channels. Premixed flames in confined channels undergo distinct changes in their structure as they propagate. Ignition is followed by a growing spherical flamelet. This flame grows faster along the axis of the combustion chamber, which leads to an elongated flame structure, known as the "finger flame", which is shown in Figure 2.1a. When the sides of the finger flame touch the walls of the combustion chamber, the flame area rapidly reduces, and the leading edge of the flame flattens to form a "planar flame" shown in Figure 2.1b, which then collapses to form an inward pointing cusp-shaped flame called the "tulip flame", shown in Figure 2.1c.

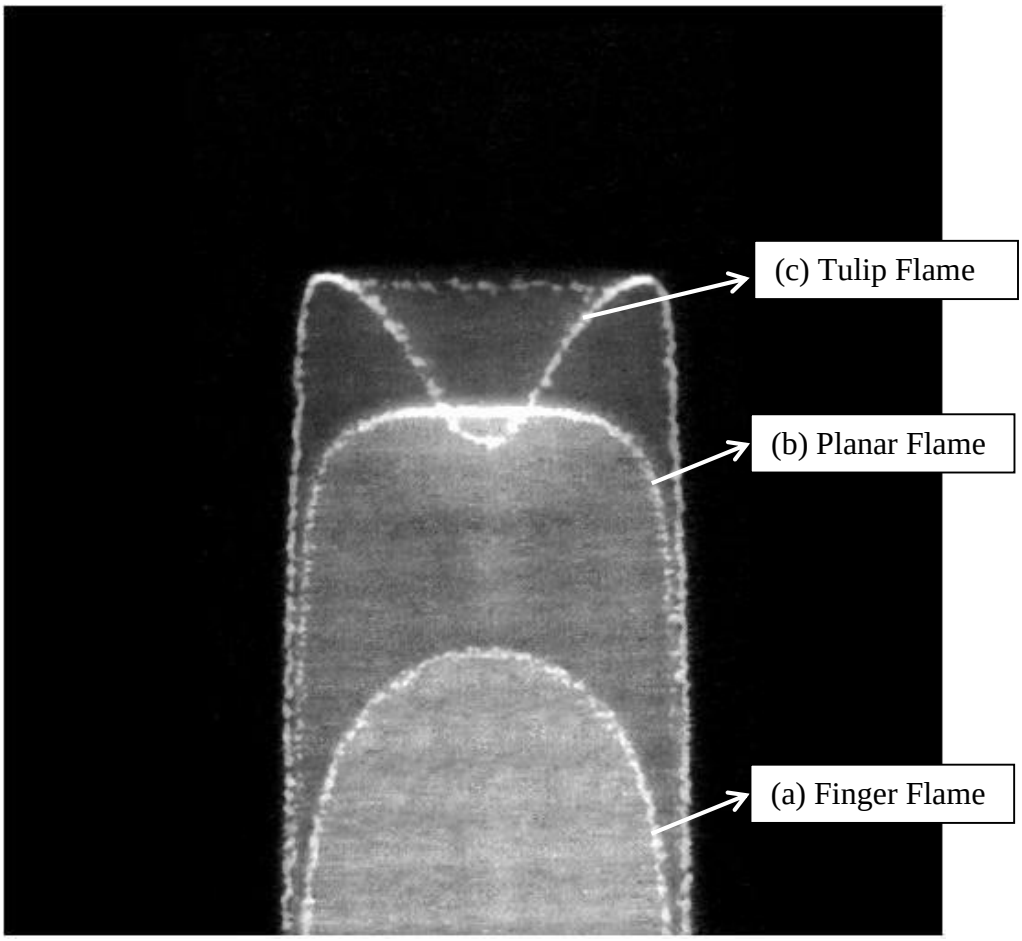

Figure 2.1: Superimposition of three images showing the different topological configuration of premixed flames in confined channels. Clanet and Searby (1996).

This topological transition occurs for premixed flames in closed and half-open tubes with both circular and rectangular cross-sections, where the aspect ratio (L/D) is greater than 2.

Different explanations for this transition of flame structure have been hypothesized, such as the effect of Darrieus-Landau and Taylor instabilities by Clanet and Searby (1996), Gonzales et al. (1992), N'Konga et al. (1993), McGreevy and Matalon (1994) and Dold and Joulin (1995); interaction of the flame front with its self-generated pressure wave by Guenoche (1964); viscous flow interaction with the flame front by Ellis (1928), Starke and Roth (1986) and Marra and Continillo (1996); and the vertical fluid flow interaction with the flame front by Dunn-Rankin and

Sawyer (1985), Rotmann and Oppenheim (1986), Matalon and Metzener (1997) and Kaltyev and Reidel (2000).

CHAPTER 3

EXPERIMENTAL SETUP, TEST METHODOLOGY AND DATA ACQUISITION

The experimental apparatus consists of an apparatus constructed out of aluminum and glass, which encloses a cuboidal combustion chamber measuring 12 inches long, with a square cross-section whose sides measure 2 inches for a total volume of $2\times2\times12 = 48$ in^3. The combustion chamber has two rectangular walls of glass, and the other four walls (2 square+2 rectangular) are made of aluminum. This enclosed chamber is instrumented with pressure transducers, spark plugs and inlet/outlet valves. The design and construction of the MSU constant volume (CV) combustion chamber is described in detail in Appendix A.

The test procedure involves filling the combustion chamber with a prescribed fuel-air mixture. Upon equilibration, the mixture is ignited with a spark plug. The pressure data along with optical imaging of the flame propagation is recorded electronically. The combustion chamber is initially filled with compressed air and tested for leakage each time it is disassembled and reassembled. The procedure used in performing a specific, individual test is as follows –

1. The combustion chamber is assembled to the required configuration and tested for leaks using compressed air.
2. The exhaust valve is closed and fuel and air are injected into the combustion chamber to the required equivalence ratio.
3. The fuel-air mixture is allowed to settle inside the combustion chamber for a period of 30 minutes to obtain a fully premixed mixture.
4. The mixture is ignited using at least one spark plug. The pressure and a video of the flame propagation is recorded and stored electronically.

5. The combusted gases are removed by flushing the system with compressed air for a period of 10 minutes and the cycle is repeated for a new set of experimental conditions.

The waiting time for the diffusion of fuel in air to obtain a fully premixed mixture and the time required to remove combusted gases from the combustion chamber by flushing compressed air through the system was determined after performing tests for various mixing and flushing times. The minimum time required for repeatable test results was empirically ascertained.

The amount of fuel that must be injected to obtain the required equivalence ratio is obtained using Dalton's law of partial pressure, which states that the total pressure exerted by the mixture of non-reactive gases is equal to the sum of the partial pressures of individual gases. Thus,

$$\frac{P_i}{P_{total}} = x_i \quad . \tag{3.1}$$

Using this equation, we calculate the final pressure of the combustion chamber after filling it with fuel and air. Depending on the fuel used, the initial air pressure is either maintained at ambient pressure or a partial vacuum is created in the combustion chamber in order to maintain a final total pressure that is close to atmospheric pressure.

The optical measurements were conducted by focusing the camera on the glass side of the combustion chamber. For the optical measurement of flame propagation, one of the glass plates of the combustion chamber is closed to produce a dark background for the flame. When using the Schlieren technique, collimated light is allowed to pass through either side of the glass plates to form an image of the flame structure. The camera records the experiments at either 5,000 or 20,000 frames per second (FPS) depending on the flame speeds and test conditions. In order to reduce noise and capture the accurate structure of the flame, background light is eliminated by running the tests in a dark room. The pressure data are recorded at 10 kHz and stored along with the ignition

data. Once the experiment is completed, the recorded images are post processed in MATLAB to obtain the instantaneous position of the flame along with the flame speed. The MATLAB program used to post-process the recorded images is described in Appendix C.

CHAPTER 4

EXPERIMENTAL RESULTS

A stoichiometric mixture of methane and air is used as the combustible mixture in all of the experimental tests. This is done to ensure that the results of different combustion chamber configurations and ignition conditions can be compared with each other. Based on Dalton's law of partial pressure, for stoichiometric methane-air mixtures, the final pressure of the combustion chamber is calculated to be 111.96 kPa. The initial condition is obtained by flushing the system with compressed air. Methane is pumped into the combustion chamber at ambient pressure until the final pressure is 111.96 kPa. The inlet and exhaust valves are closed. The mixture is allowed to settle for thirty (30) minutes to allow complete mixing to form a fully premixed fuel-air mixture. The structure and propagation of flames under a variety of test conditions was studied. In order to maintain consistency between different test results, the pressure transducers are recalibrated every ten (10) cycles of usage. To ensure an accurate mixture ratio inside the combustion chamber, an Omega PX43EO-25GI pressure transducer, with an accuracy of 0.1% over the range of 25 psi, is used to measure the amount of methane injected into the combustion chamber.

Single Spark Ignition

In the single spark ignition setup, the combustion chamber was filled with stoichiometric methane air mixture at an initial pressure of 1 bar. The premixed fuel air mixture was ignited by a single spark source. A record of the pressure and flame propagation was made. The video was post-processed in MATLAB to obtain the position of the flame front for every frame.

Upon ignition by a spark plug, a growing spherical flame kernel was initially formed. The flame-front grew faster along the length of the tube when compared to the width, which led to the elongation of the flame. In this burning stage, the flame area grew rapidly to form a "finger" shaped flame front. When the sides of the finger flame touched the cold walls, the side skirt extinguished, the surface area of the flame rapidly decreased and it progressively flattened to take the shape of a planar flat flame. The planar flame subsequently changed its shape to eventually form an inward pointing cusp near its center; this shape has been traditionally called the "tulip-flame". The flame-front then maintained its tulip shape as it propagated along the remaining length of the tube until it was extinguished by the cold wall on the opposite end of the tube. Small but obvious distortions to the tulip flame were caused, apparently, by the combined influences of pressure waves and gravity. The optical record of the flame propagation is shown in Figure 4.1 for every 10 milliseconds time intervals from ignition until extinction.

t=0 ms, Ignition.

t=10 ms, Spherical flame.

t=20ms, Finger-flame formation.

t=30 ms, Planar flame.

t=40 ms, Formation of tulip flame.

t=50 ms, Propagation of tulip flame.

t=60 ms

t=70 ms

Figure 4.1: Flame propagation along the tube, showing the evolution of the flame structure.

Figure 4.1 (cont'd)

t=80 ms

t=90 ms

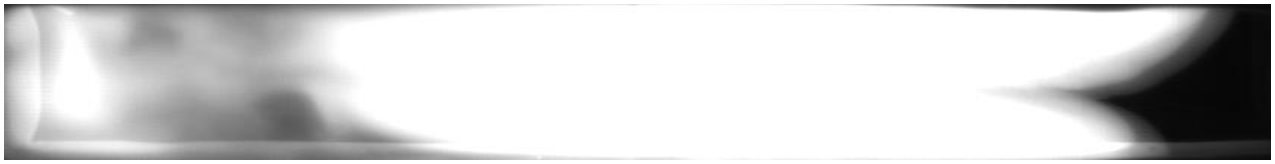

t=100 ms

t=110 ms, Collision with cold wall

As shown in these images, upon ignition, the spherical flame-front grows rapidly outward. Approximately ten (10) milliseconds (ms) after ignition, a nascent finger flame develops. At t = 30 ms, the finger flame skirt is quenched by the cold wall and the flame surface area rapidly decreases. This causes the flame to slow down and the flame front collapses to form an inward pointing cusp called the "tulip flame" at t = 40 ms. The flame front eventually collides with the cold wall at the opposite end of the tube at t = 120 ms while preserving its tulip shape. The schlieren imaging of the ignition and flame propagation event is shown in Figure 4.2.

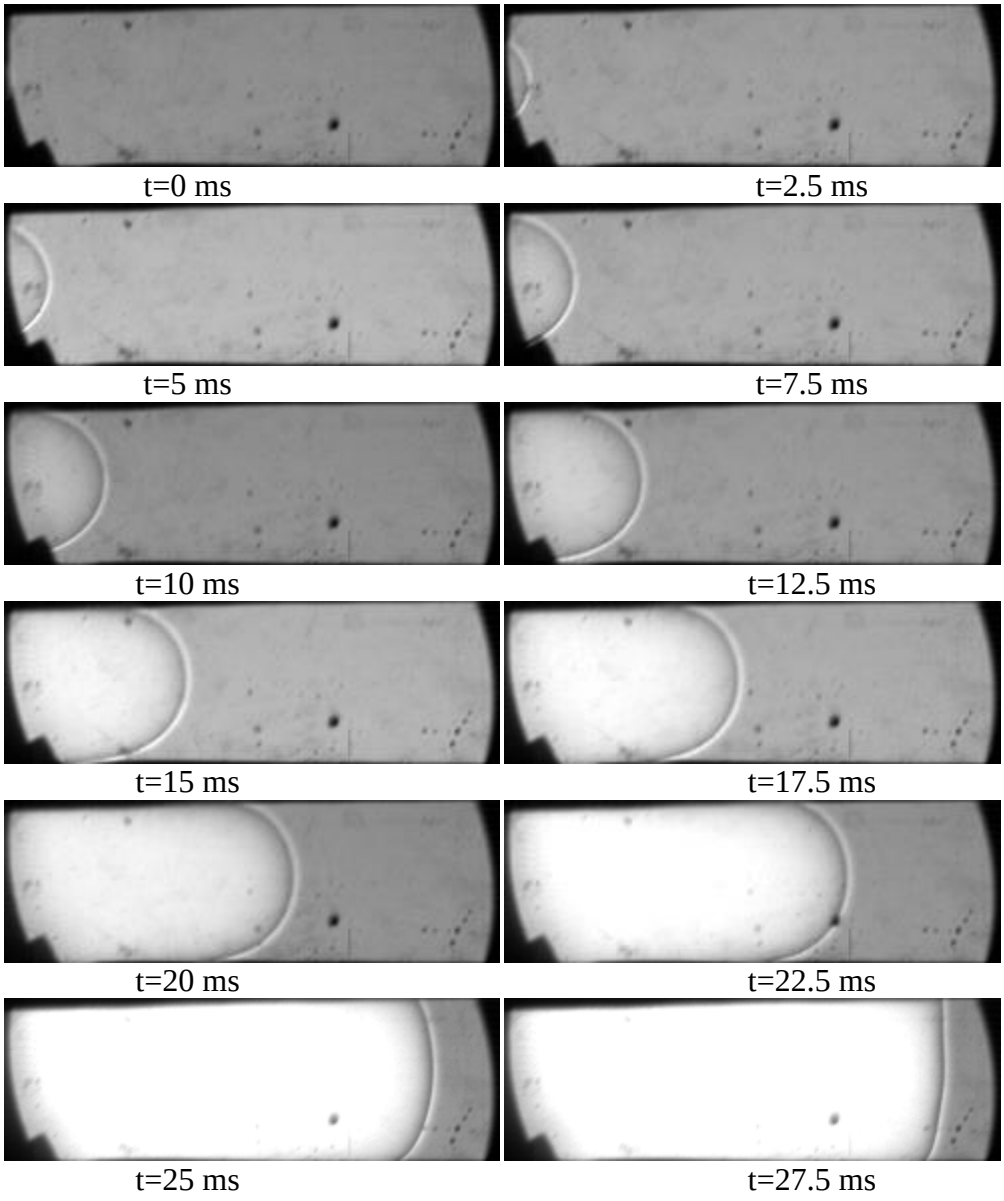

Figure 4.2: Schieren image of flame propagation.

We observe that ignition by the spark plug is followed by a rapidly expanding spherical flame front, which can be observed in the time interval 2-10 ms. The tip of the flame travels faster, however, than the sides of the flame that eventually approach the walls. This leads to the formation of an elongated “finger flame”, which can be seen at 15 ms in Figure 4.2. The sides of the finger flame are quenched by the cold wall and cause the flame surface area to decrease rapidly. A planar flame shape occurs at 27.5 ms.

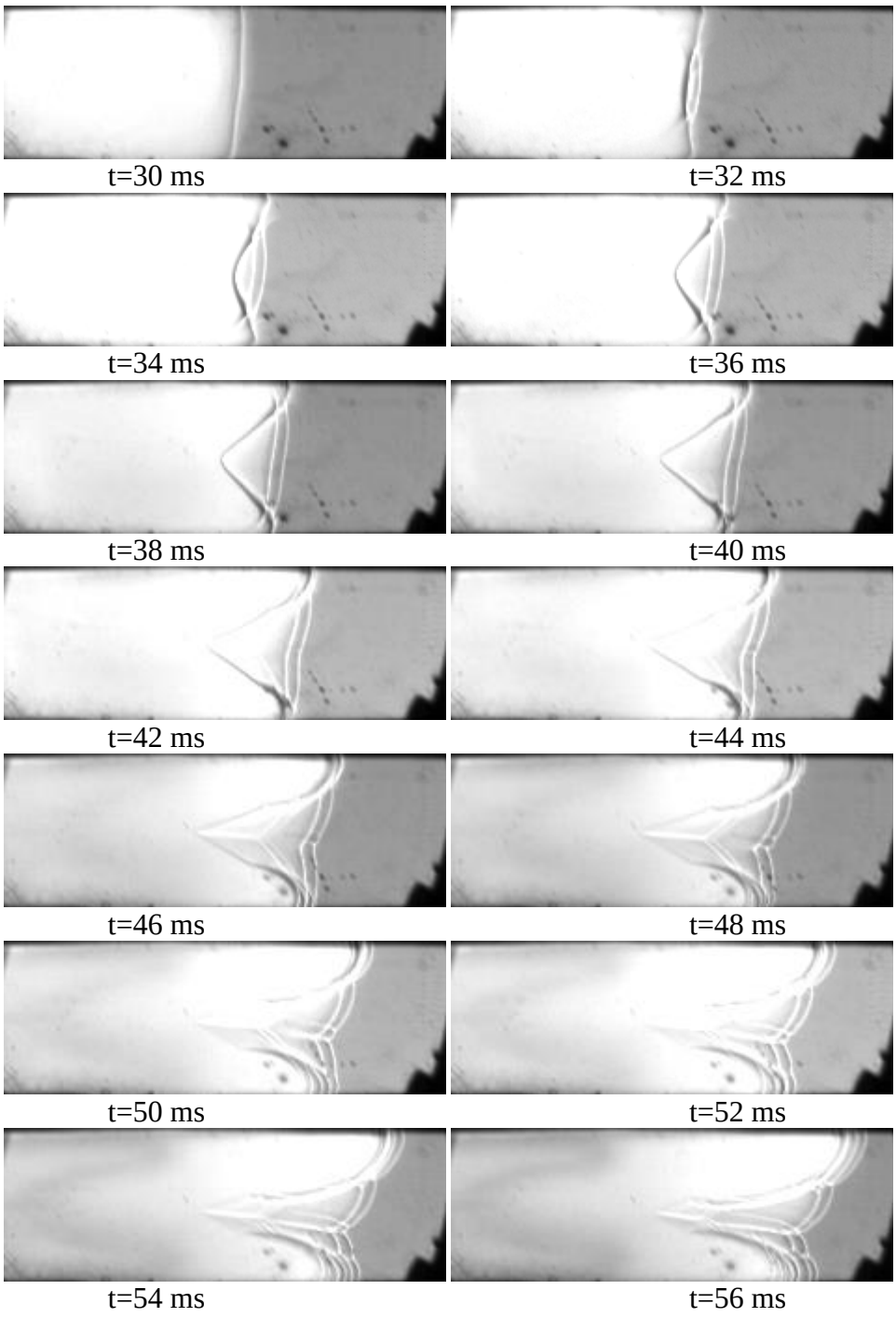

Figure 4.3: Schlieren image of tulip flame formation.

The transition from a planar flame front to a tulip flame takes place in a time interval of the order of 10 ms. At t = 38 ms (in Figure 4.3), we observe the 3-D structure of the tulip, which is an inward

pointing cusp at the center from which four “petals” emerge. The two vertical lines near the outer edge of the lobe are the flame close to the glass walls. At t = 50 ms, the tulip shape undergoes a distortion to its structure, likely from the influence of thermo-acoustic instabilities and gravity. This causes the formation of smaller cells that grow and propagate along the lobes of the tulip flame. The effect of gravity driven buoyancy causes the upper lobe of the tulip flame to travel slightly faster than the lower lobe.

The normalized position of the flame front is shown in Figure 4.4. The various stages of flame front structure are marked. Stage I indicates the ignition event followed by the growth of the spherical flame. Stage II begins with the formation of the finger flame. Stage III indicates the transition from a finger flame to a planar flame. The planar flame which subsequently changes to a tulip flame is shown in stage IV.

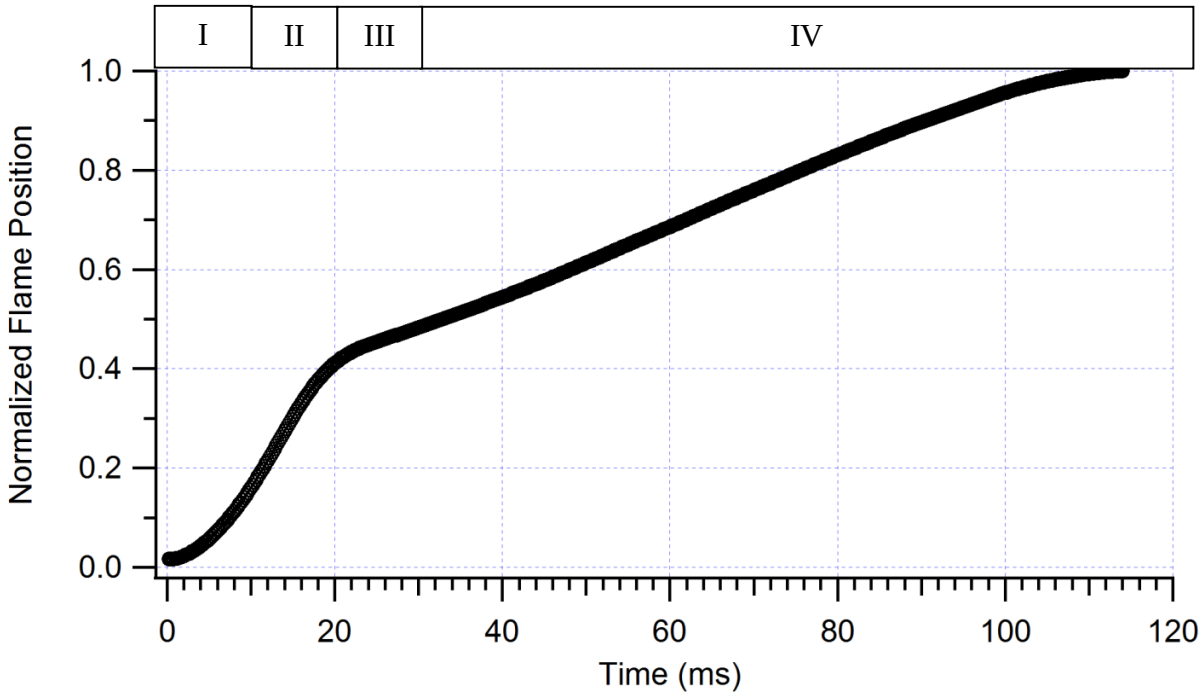

Figure 4.4: Flame position vs. time, showing the four stages of flame propagation (I=ignition, II=finger flame, III=transition to planar flame, IV=propagating tulip flame).

We note that it is possible to define a fifth stage of eventual quenching as the tulip fame structure is extinguished by the cold downstream wall. This distinction, however, is presently eschewed but is discussed later in this thesis. The normalized flame position data shows the mean position of the flame front for each instant of time. The flame position changes rapidly from 0 to 20 ms, after which the rate of change in the mean flame position is slower. The flame speed data are obtained by calculating the time-derivative of the flame position as shown in Figure 4.5.

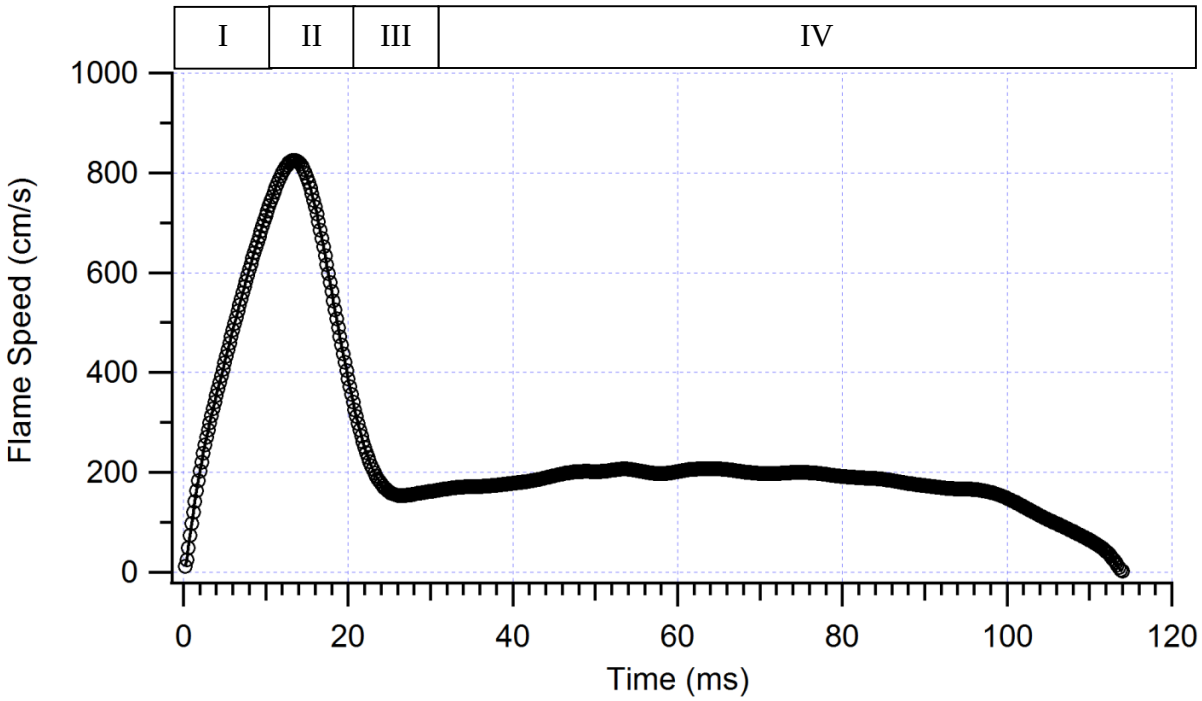

Figure 4.5: Flame speed vs time.

The flame speed plot in Figure 4.5 indicates that the fastest physical flame speed occurs shortly after ignition. The spherical flame kernel accelerates towards the unburnt mixture. Its surface area increases correspondingly. At t = 15 ms, the surface area of the flame-front reaches its maximum. The speed of the flame-front starts to decrease as the flame shape becomes planar. At t = 25 ms, the flame transforms to a tulip shape. The speed of propagation remains approximately constant until it is quenched by the cold wall on the opposite end of the tube at t = 118 ms.

The instantaneous flame speed for the normalized position on the tube is shown in Figure 4.6. It is observed that the transformation of the flame front from planar to tulip shape takes place at roughly half the length of the tube. The speed of propagation of the flame front is approximately constant after the tulip shaped flame front has formed.

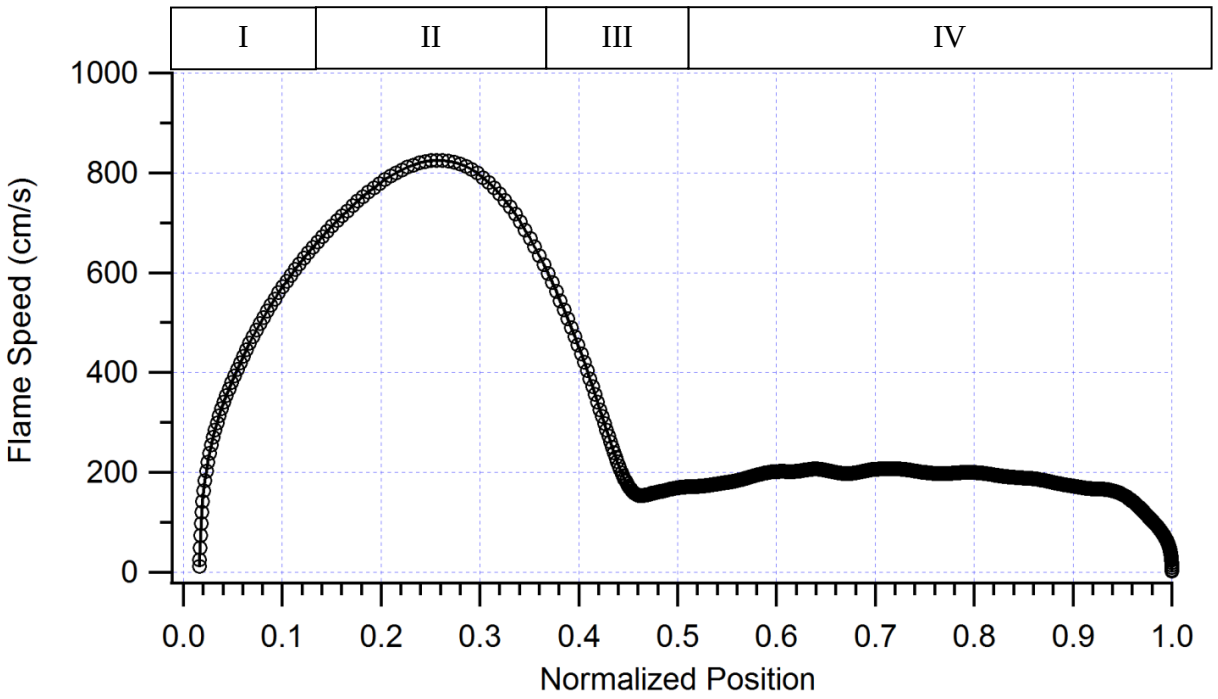

Figure 4.6: Flame speed vs normalized position. Note that the transition to the tulip structure takes place slightly before the flame-front has reached the streamwise center of the channel.

Dual Spark Ignition

The dual spark ignition setup consists of two spark plugs on the opposite ends of the tube along its length. This allows the influence of ignition from multiple sources to be studied in detail. Both spark plugs are flush mounted on the combustion chamber. The exact time of the spark discharge can be electronically controlled through a delay circuit. Experiments are conducted for spark delay timings of 0, 10, 20, 25, 30, 40, 50, 60, 75, 885 and 110 ms. The flame front from the initial spark is influenced differently based on the stage of propagation inhabited by the established flame. The ignition from the opposite end has a greater influence when the tulip shape is fully developed than when the initial flame is still a spherical or planar flame that is rapidly evolving. The experiments for 0, 25 and 50 ms spark delay are discussed in greater detail in the following sub-sections.

Dual Spark Ignition – 0ms delay

In this experiment, the two spark plugs are fired at the same time, and two separate flame fronts are formed which travel towards each other. The amount of energy deposited by each spark is the same as that released by a single spark. The optical record of the flame propagation is shown in Figure 4.7. We observe that the different stages of flame propagation are preserved when compared to a single spark ignition. In other words, the sequence of events is largely the same. Shortly after ignition, a spherical flame front is formed at each end of the combustion chamber near the spark plug. The accelerating spherical flame fronts transform into planar flame fronts after which the tulip flame shape is formed. The time taken for complete combustion is approximately equal to half the time taken for the single spark case.

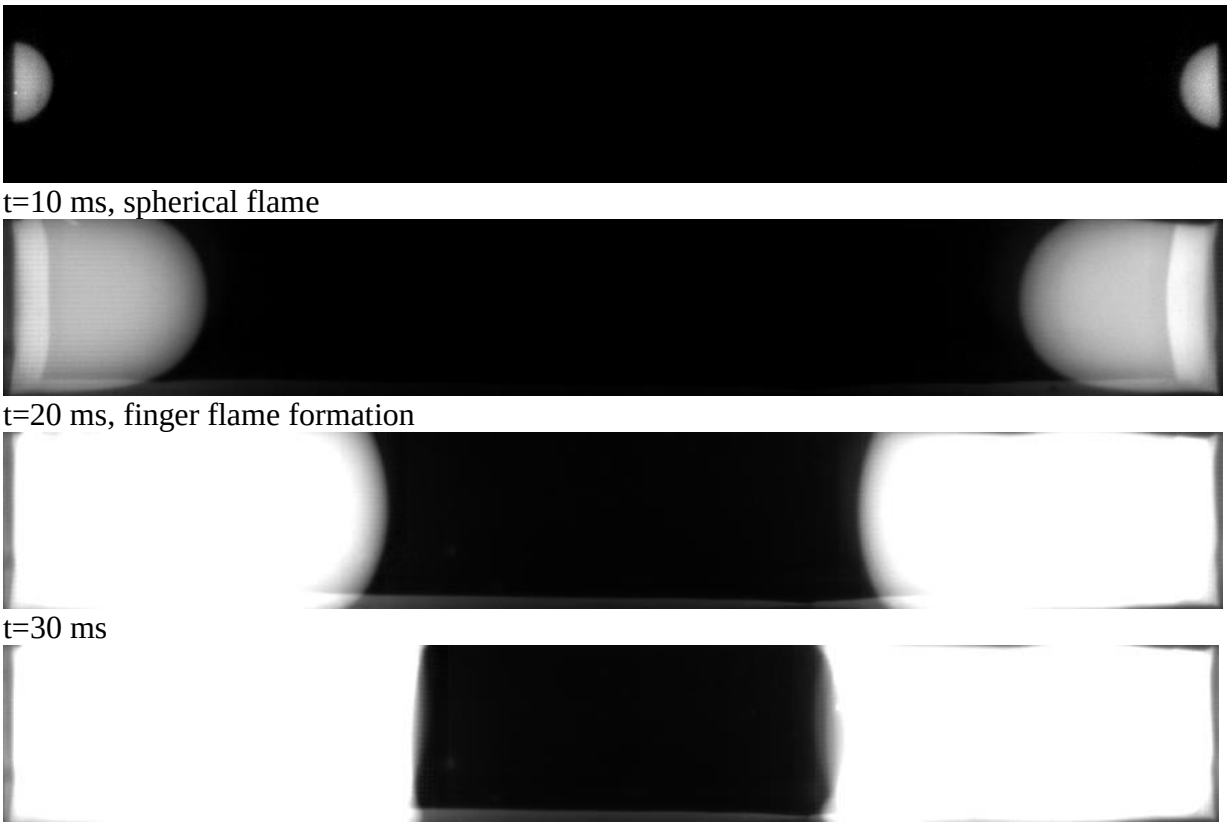

Figure 4.7: Flame propagation along tube, dual spark with 0 ms delay.

Figure 4.7 (cont'd)

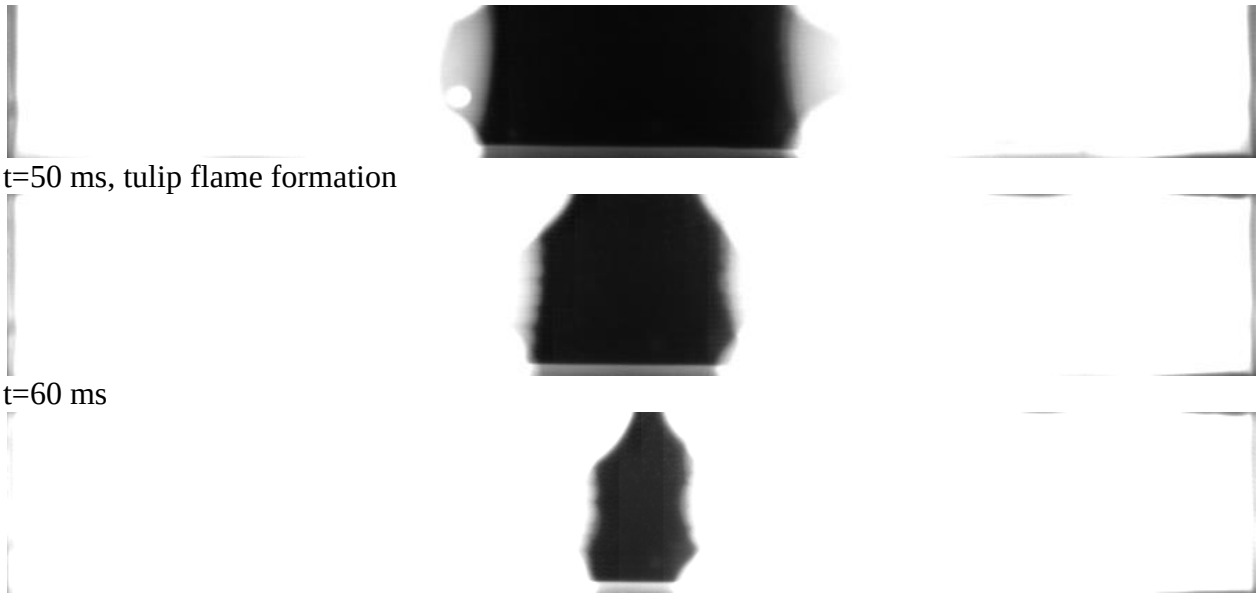

t=50 ms, tulip flame formation

t=60 ms

t=70 ms

The normalized position of the flame fronts, and the flame speeds are shown in Figure 4.8. The flame travelling from the left end of the tube to the right end is called flame L-R, whereas the flame travelling in the opposite direction is called flame R-L. We observe from Figure 4.8 that the traces for both the flame fronts follow a similar profile as they propagate from each end of the tube to the middle of the channel. The flame fronts collide with each other at half the length of the tube at the normalized position, 0.5.

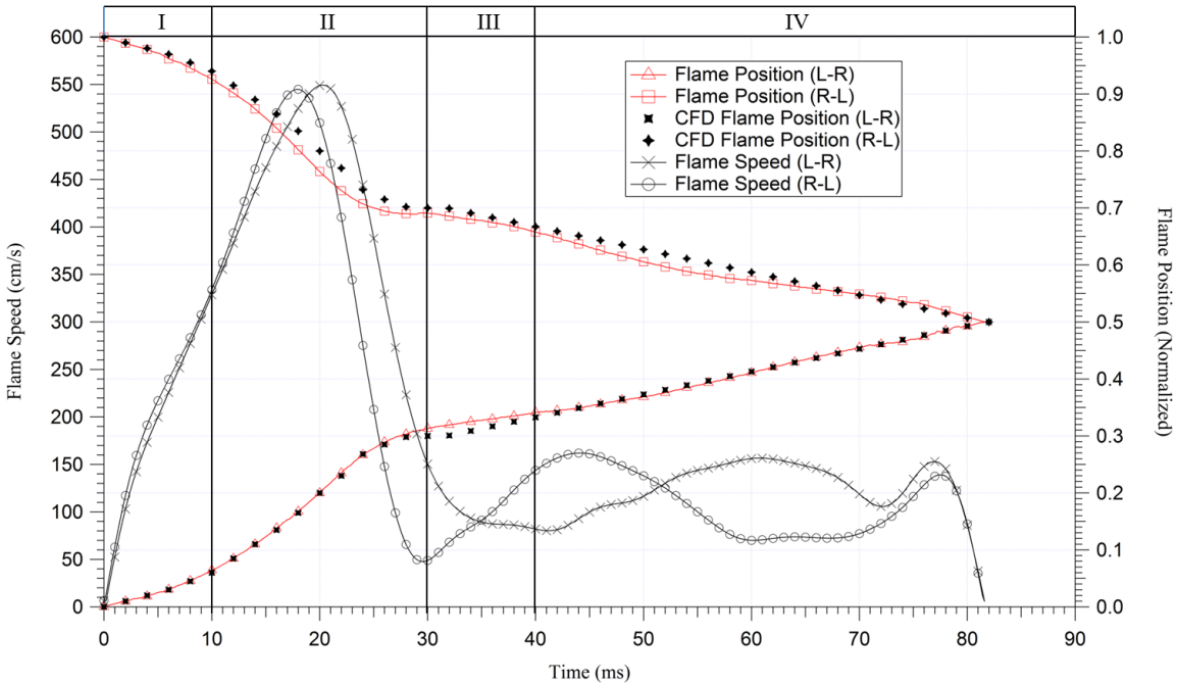

Figure 4.8: Normalized flame front position and flame speed versus absolute time for two sparks fired simultaneously.

Flame R-L ignition takes place at X=1 in the normalized scale and flame L-R ignition takes place at X=0 in the normalized scale.

It is observed from the data that the flame speed profile is similar to the single spark combustion process. The sequence of observations is as follows: (1) The ignition event is followed by an accelerating spherical flame on both ends of the combustion chamber; (2) The spherical flame undergoes elongation along its length to form a finger shaped flame front; (3) The side skirts of the finger flame are then quenched by the cold walls to create a planar flame front, (4) This causes a decrease in the flame surface area and also reduces the speed of propagation; (5) The planar flame then transforms to a tulip structure, which preserves its shape and speed until the two flames collide with each other; (6) An oscillating behavior is observed in the speed of propagation of the tulip flame caused by small changes in the shape of the tulip as it propagates along the axis of the channel in the combustion chamber.

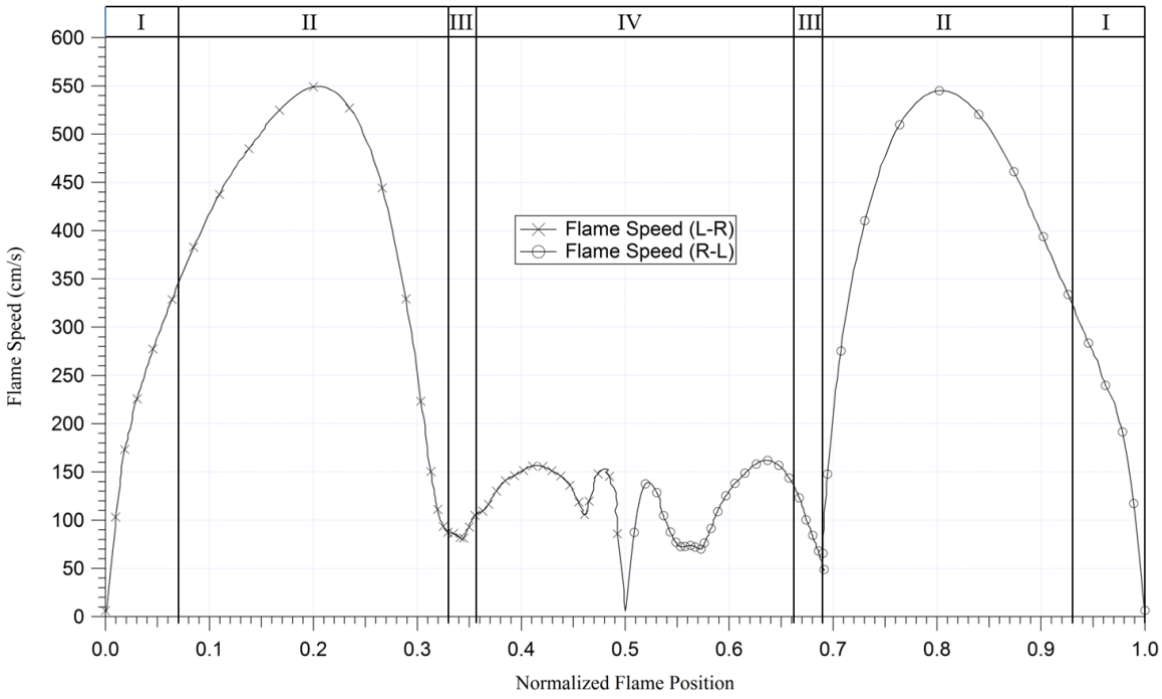

Figure 4.9: Flame speed vs normalized flame position.

We now discuss some of the details of this combustion process. Upon ignition, the spherical flame shape is maintained for the first 10 ms. Thereafter, the fingering flame front grows faster along the channel axis, accelerating strongly in the process until 20 ms at which instant the front speed is 550 cm/s. At 30 ms from the start of ignition, the side skirts of both finger flames are extinguished by the cold walls and the flames rapidly flatten, becoming planar. The flame fronts then evolve almost immediately into inward pointing cusp shapes, which are fully developed at 40 ms while maintaining an average front speed of 120 m/s. The opposing flame fronts subsequently maintain their tulip shape even when they undergo contact with each other. They finally extinguish at an elapsed time of 82 ms from the start of ignition. Flame extinguishment occurs at the geometric center of the tube.

The position and speed of the flame fronts are shown in Figure 4.8. The different topological structures of the flame are divided into four stages, as indicated in the figure. Stage I represents the formation and growth of the two spherical flames. Stage II begins with the elongation of the

flamelet along the channel axis, and is called the finger flame stage. Stage III delineates the transition from finger flame to tulip flame, while stage IV denotes the propagation of the tulip flames. A fifth stage, when the flames strongly interact with each other during the mutual annihilation process can be defined but this topic is not addressed in detail in this thesis. Since there are two oppositely propagating flame fronts, the flame front formed by the ignition of the spark plug on the left side of the axis is termed (L-R) whereas the flame front formed by ignition of the spark plug on the right side is termed (R-L). This flame naming convention is used throughout the remainder of this thesis. The instantaneous flame speed as a function of the normalized spatial coordinate, which is the instantaneous front position divided by the channel length, is shown in Figure 4.9. The fronts attain a peak speed of 550 cm/s, observed during the propagation of the finger flame, which occurs at approximately 20% along the axial length. The tulip flame fronts collide with each other and annihilate one another at the center of the channel.

Dual Spark Ignition – 25ms delay

In this experiment, the two spark plugs are fired with a delay of 25 ms. The spark plug on the left side of the combustion chamber is fired first followed by the one on the right side. The optical record of the flame propagation is shown in Figure 4.10.

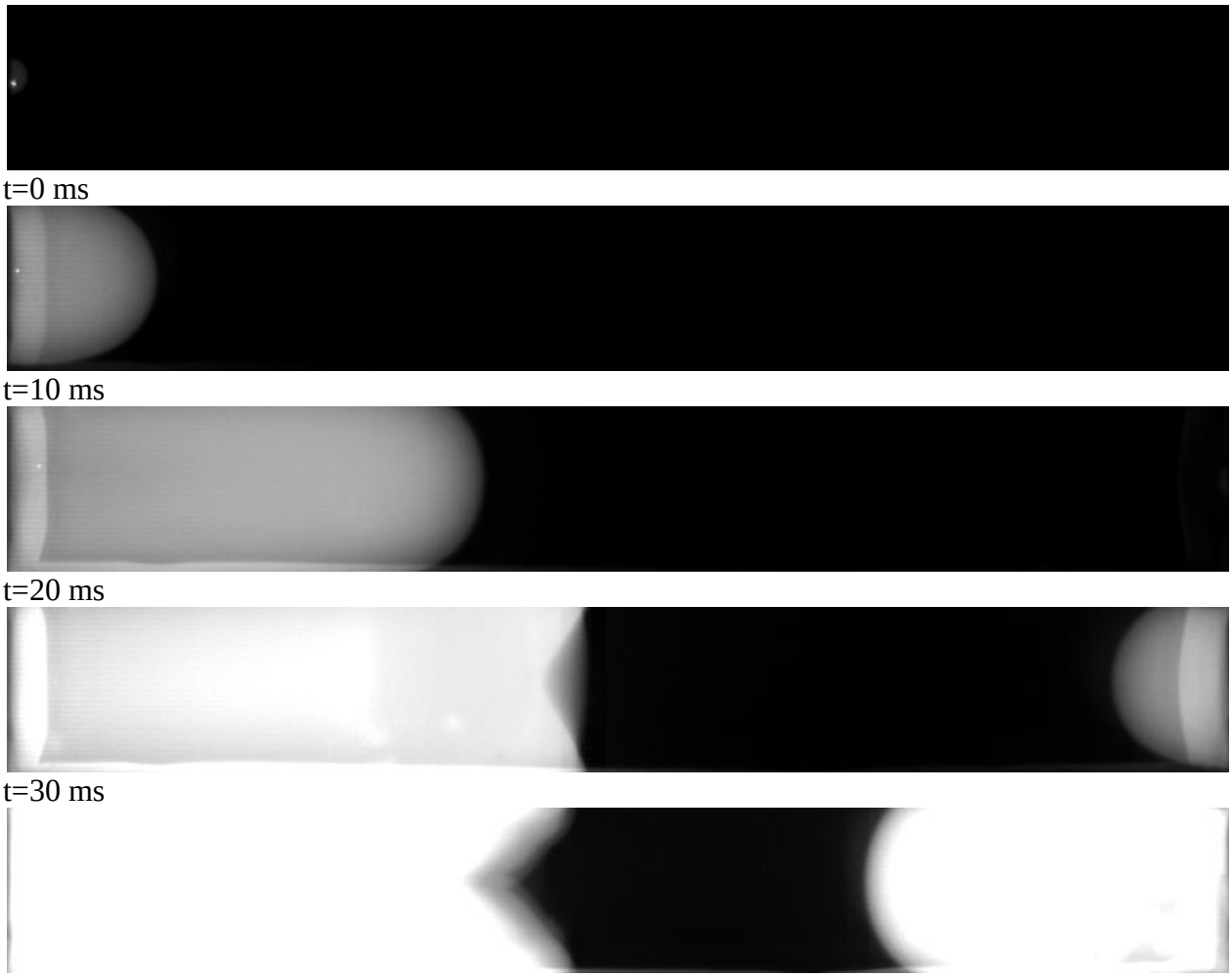

Figure 4.10: Flame propagation along tube, dual spark with 25 ms delay.

Figure 4.10 (cont'd)

t=50 ms

t=60 ms

The ignition event is followed by a growing left side spherical flame front, which undergoes transition to a finger flame. At 25 ms, the side skirts of the finger flame begin to extinguish at the cold wall, with the front speed strongly decreasing, nearly as rapidly as it initially increased, from its maximum value of 790 cm/s. At this instant, 25 ms, the second spark plug is ignited.

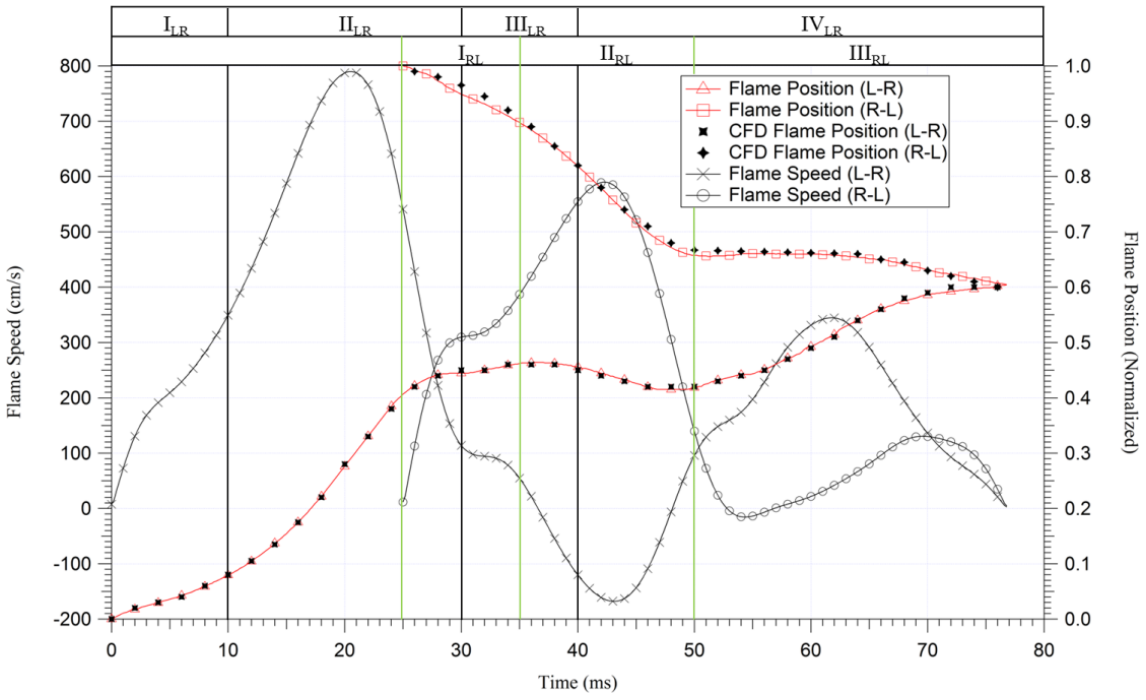

Figure 4.11: Flame position and speed vs time for the case of a 25 ms delay in spark timing between flames L-R and R-L respectively.

A growing spherical flame front is formed at the right side of the combustion chamber. Presently, this spherical flame front exerts a minimal influence on the continuing propagation of flame L-R. As the flame R-L transitions from a spherical flame to a finger flame, a net transport of unreacted gas occurs away from this flame front, towards the unburnt side. This expansion flow, which acts like a leftward-directed piston, causes flame L-R to attain a ***negative*** velocity with respect to the combustion chamber (laboratory) coordinate system, peaking at 180 cm/s toward the left wall. In other words, the flame L-R briefly moves in reverse. As the side skirts of the finger flame R-L begin to extinguish upon contact with the cold channel walls, the flame speed of the R-L flame front decreases rapidly and the L-R tulip flame again proceeds forward (at t = 48 ms) with a positive though strongly diminished flame speed. The flame front of the L-R tulip flame reaches its second peak value of 350 cm/s shortly before the transition of the R-L flame front into a tulip structure. The position and speed of the two flame fronts are shown in Figure 4.11. The instantaneous flame speed versus the normalized length of the tube is shown in Figure 4.12. The peak speed of flame L-R is 790 cm/s and that of flame R-L is 590 cm/s. The two flame fronts collide with each other at a normalized distance of 0.6 from the left side of the combustion chamber at which location they annihilate one another.

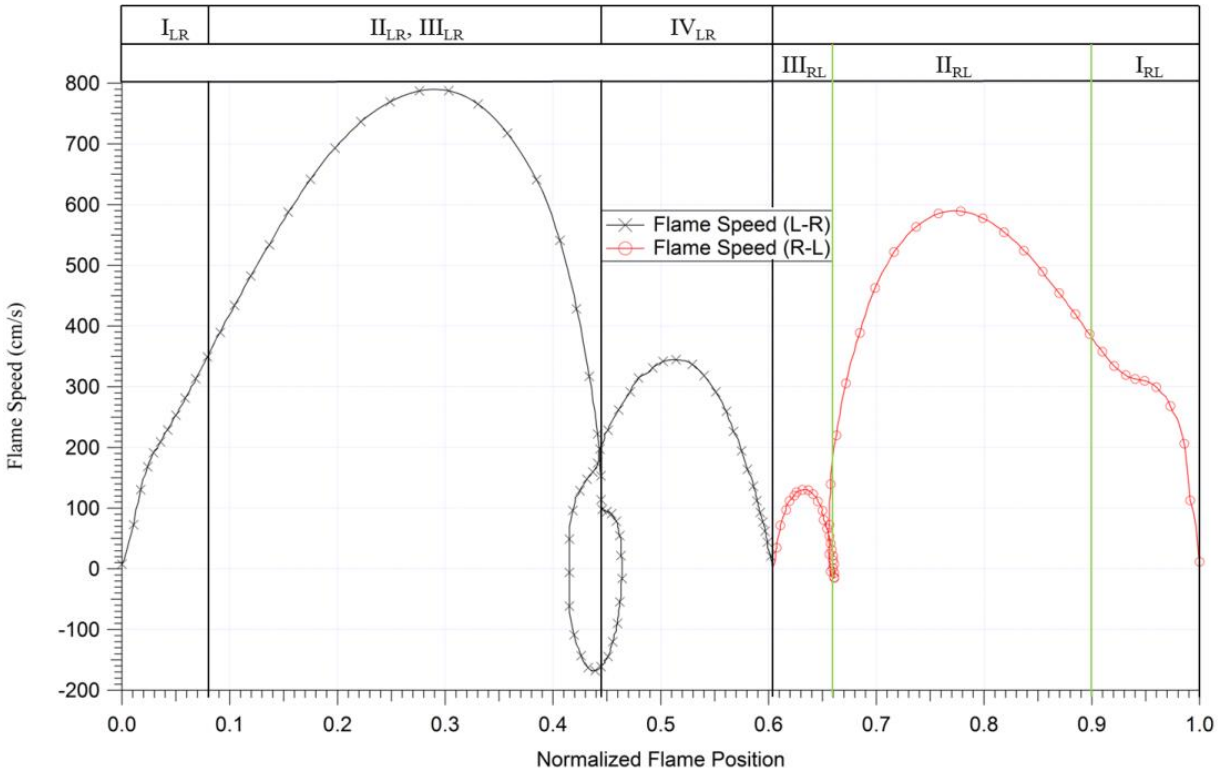

Figure 4.12: Instantaneous flame speed vs normalized position in the channel. Here X = 0 is the left side of the channel, and X = 1 is the right side of the channel.

Dual Spark Ignition – 50ms delay

t=0 ms, Ignition of spark I

t=10 ms, Finger flame formation

t=20 ms

t=30 ms, Planar flame

t=40 ms, Tulip flame formation

t=50 ms, Ignition of spark II

t=60 ms, Finger flame formation

Figure 4.13: Flame propagation along tube, dual spark with 50 ms delay.

Figure 4.13 (cont'd)

t=70 ms, Planar flame

t=80 ms, Tulip flame formation

t=90 ms, Flame collision

In this experiment, the two spark plugs were programmed for a 50 ms delay between firing. The left spark plug was fired first, followed by the right spark, 50 ms later. The optical record of the flame propagation is shown in Figure 4.13. Upon ignition, the L-R flame front followed the same topology evolution sequence as that of a single spark flame until 50 ms. At this instant, the tulip flame L-R has travelled a normalized distance X = 0.58 along the length of the channel. The second spark ignition event produces little influence on the flame LR until t = 60 ms. At this instant, the flame R-L transitions from a spherical flame to a finger flame, accelerating in the process. This leads to flame L-R attaining a negative front speed in the laboratory coordinate system.

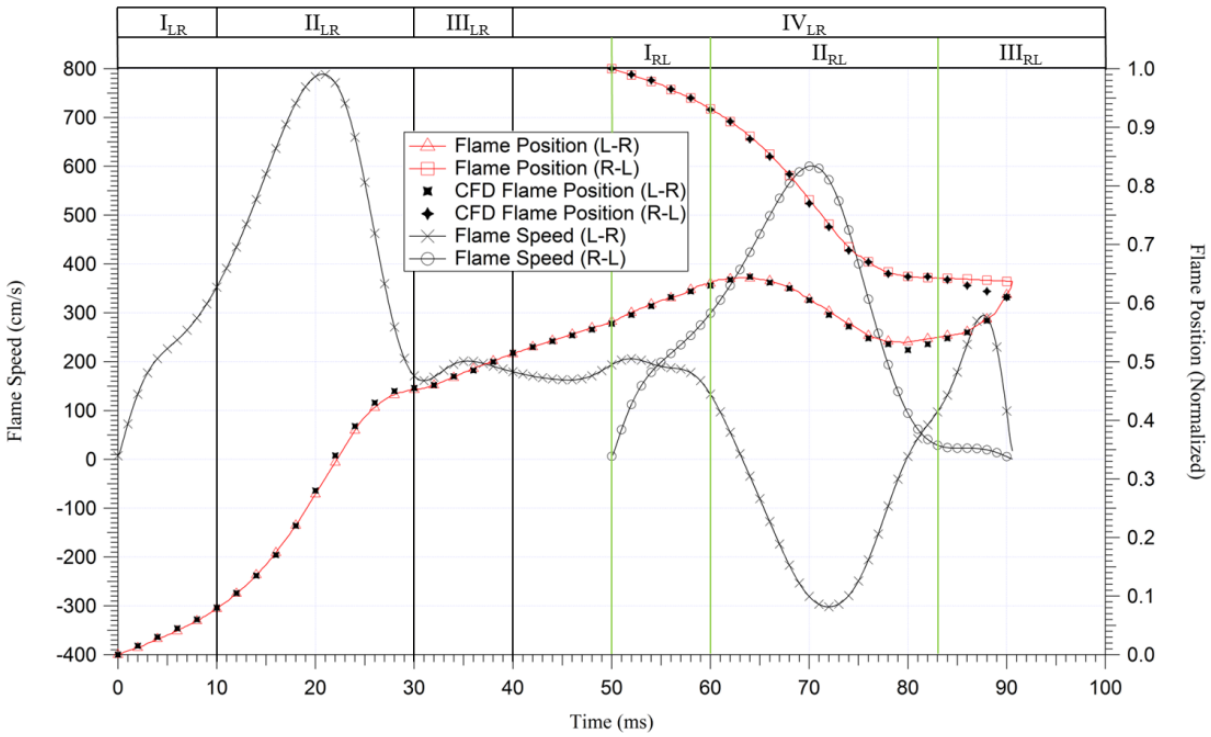

Figure 4.14: Flame position and flame speed vs time.

The peak front speed of flame R-L (600 cm/s at t = 70 ms) approximately coincides with the peak negative front speed of flame L-R (300 cm/s at t = 72 ms). Thereafter, the front speed of flame R-L rapidly decreases until it is extinguished by flame L-R. Flame L-R reverses its direction of propagation at t = 80 ms, and attains a second positive flame speed peak of 300 cm/s at t = 88 ms. This occurs when the flame R-L undergoes a transition from finger to planar and then tulip flame stages. Thereafter, the front speed of flame L-R decreases until it is extinguished (annihilated) by collision with flame front R-L. The flame front speeds and normalized positions of the two flames are shown in Figure 4.14. The instantaneous flame speeds along the normalized length of the combustion chamber are shown in Figure 4.15. Flame L-R has three flame speed peaks - 800 cm/s at t = 20 ms, -300 cm/s at t = 70 ms and 300 cm/s at t = 88 ms. Flame R-L has one flame speed peak: 600 cm/s at t = 70 ms.

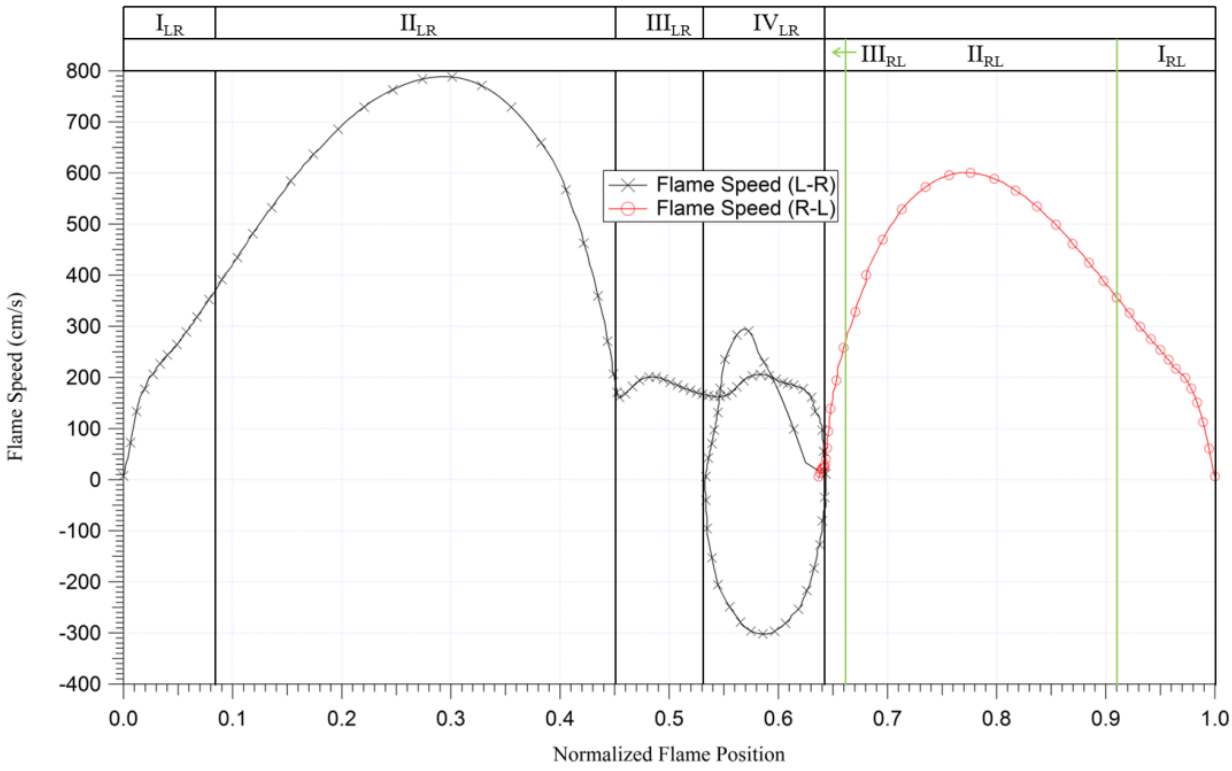

Figure 4.15: Instantaneous flame speed vs flame front position in the channel. X = 0 is the left side of the channel, and X = 1 is the right side of the channel.

Spark Delay Comparison

The total time required for complete combustion for various firing delays for the second spark is shown in Figure 4.16. For a single spark case, combustion is complete at 108 ms after ignition: we use this time as our global normalization because all of the two-spark cases are faster. For a spark delay of 0 ms (simultaneous firing), the normalized time for combustion is 0.76 (i.e., complete combustion occurs in 76% of the time taken for single spark ignition). The combustion time reaches a minimum value for a spark delay of 10 ms. Here, complete combustion occurs in 70% of the time taken for single spark ignition. A delay of 10 ms physically corresponds to firing the second spark when the flame L-R is undergoing transition from a spherical to a finger flame front. In the range 10 – 25 ms delay the overall burn time is very nearly constant, suggesting that firing the second spark *before transition* to the planar/tulip flame is a viable burn time minimization strategy. Upon transition of the flame L-R from a finger flame to a tulip flame, the normalized time taken for complete combustion increases linearly from 0.73 to 0.96.

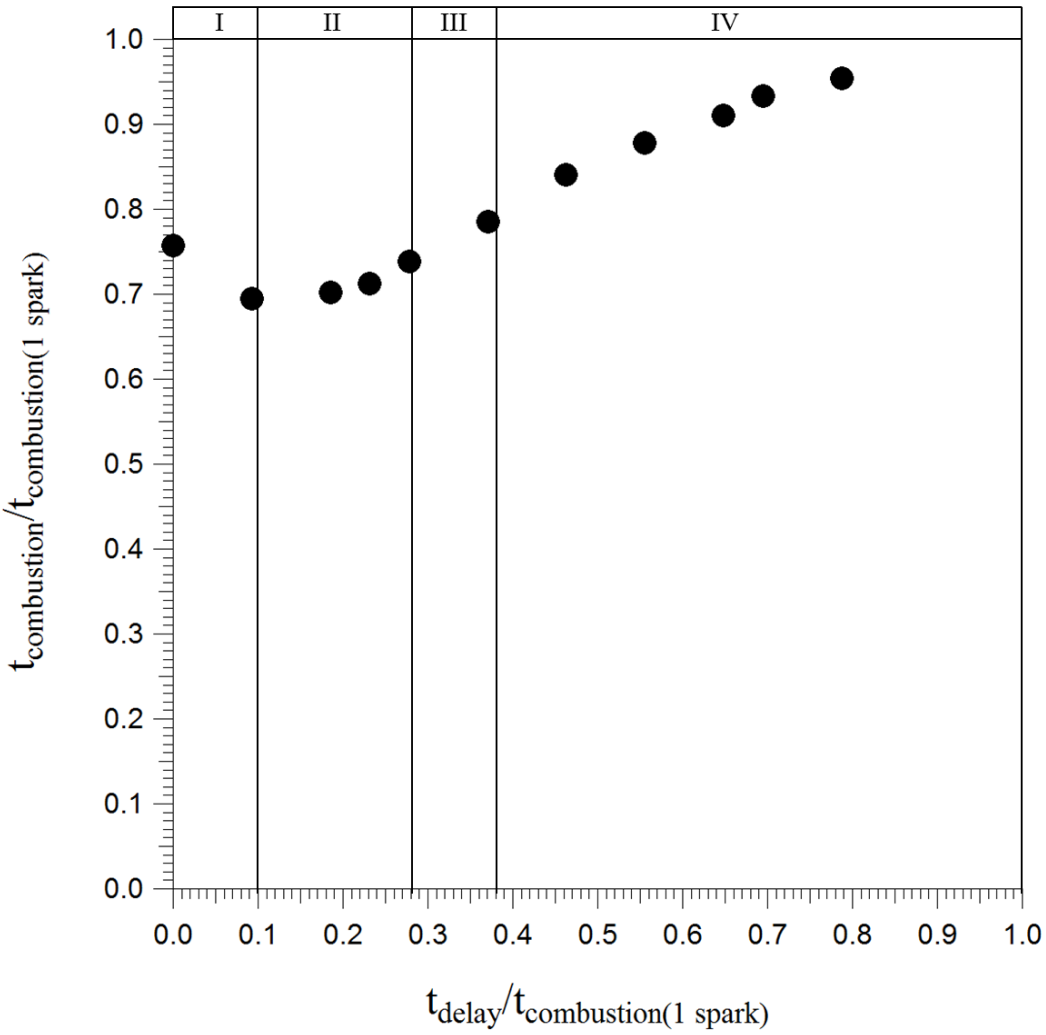

Figure 4.16: Normalized combustion time vs normalized spark delay time indicating a minimum time of combustion between 10 ms and 25 ms firing delays.

CHAPTER 5

NUMERICAL RESULTS AND TOPOGRAPHICAL ANALYSIS

The numerical simulation of the constant volume combustion process was performed to obtain the flow field inside the combustion chamber for different stages in the combustion process and to obtain the effect of flow field on the flame structure. A detailed description of the computational model is included in Appendix B, along with mesh independence and boundary condition study. A 2-D combustion chamber measuring 12″ long and 2″ high (i.e., AR = 6), consisting of structured quadrilateral cells each with a uniform edge of 1/128 cm (12.8 grid points per mm) was used as the computational domain. This was sufficient to resolve flame widths and flow details as demonstrated by numerical evaluation with a halved mesh width. The control volume V was initialized with a stoichiometric mixture of methane and air. A single-step Arrhenius reaction rate mechanism was employed. The walls surrounding the control volume, surface area A, were initialized as a no-slip boundary with constant temperature 293 K, i.e. isothermal and not adiabatic walls. The combustion process was initialized by patching a localized spot near the physical spark location at the left wall to 2100 K, as seen in Figure 5.1.

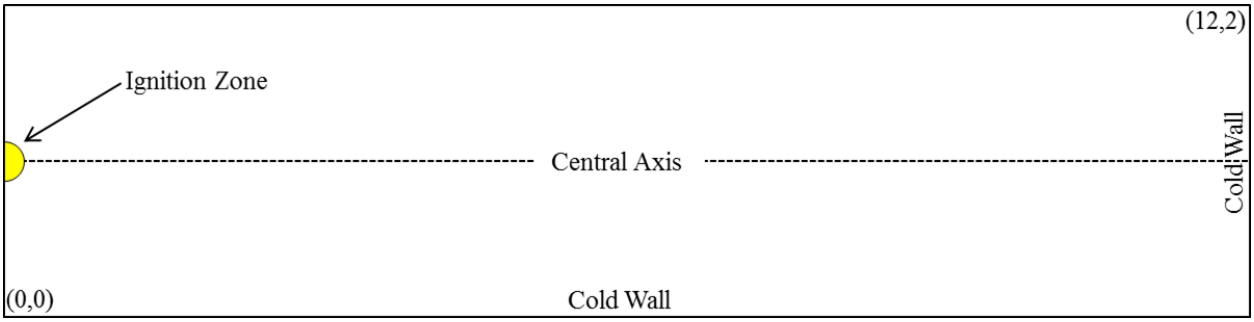

Figure 5.1: Numerical 2-D model of the combustion chamber.

The propagation of the flame from ignition until the formation of the tulip flame is shown in Figure 5.2 as a contour plot of temperature. The formation and propagation of the tulip flame in both the

spatial and temporal dimensions was compared with the experimental measurements. A comparison was also made between numerical solutions obtained using the explicit solver and an implicit solver, which indicated that the trigger for the formation of the tulip flame is not strongly dependent on the influence of pressure waves in moderate AR channels. In this feature there is compliance with the theoretical approach of Matalon and McGreevy (1994) and McGreevy (1993) in which the model assumes that the characteristic pressure wave propagation time is negligibly small compared with all other time scales (e.g., flow, chemical reaction). Therefore, the pressure change in the moderate AR chamber is, for the purposes of this investigation, a continuous function of time.

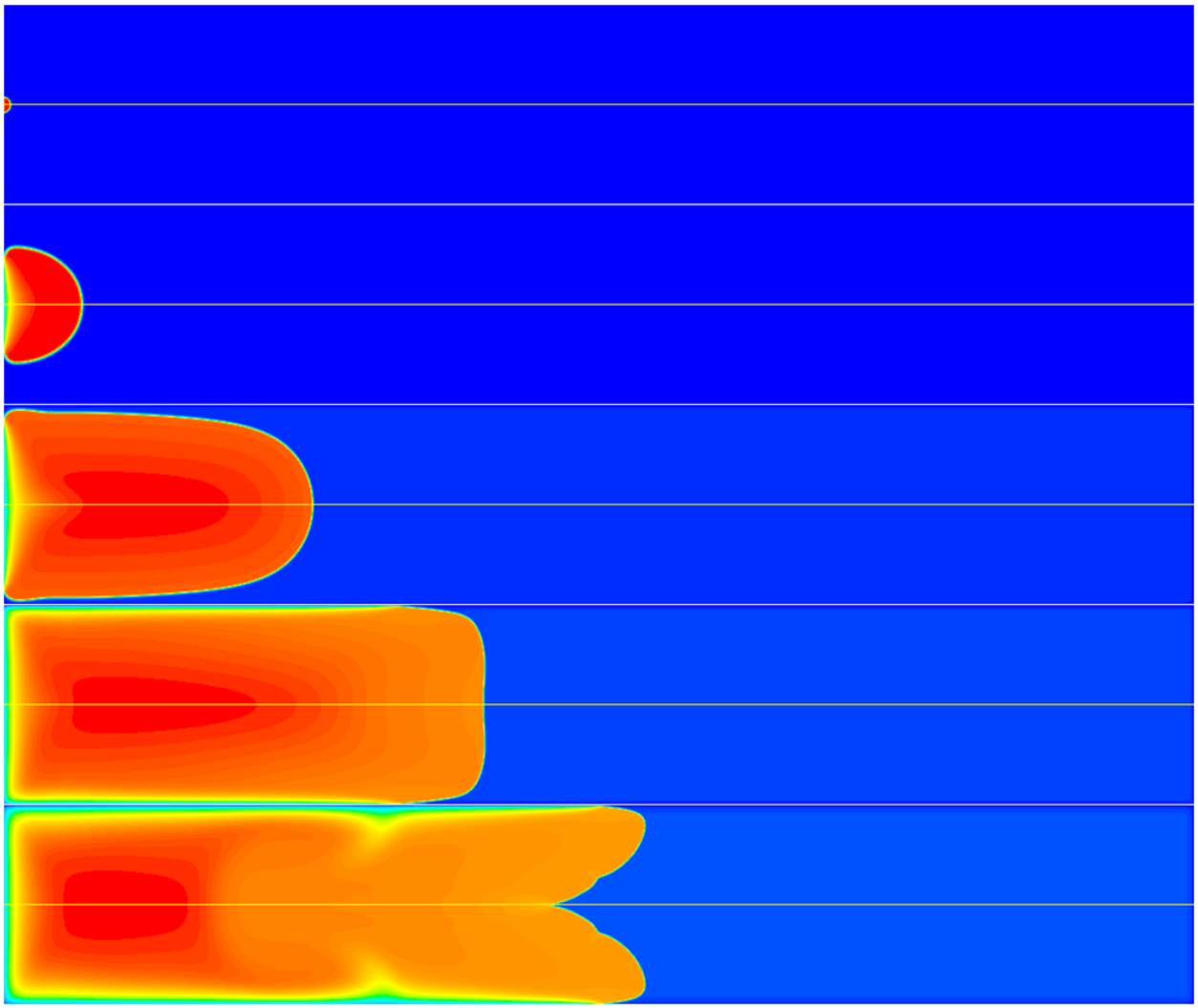

Figure 5.2: Numerical images of flame propagation in a stoichiometric mixture of methane and air taken as "stills" from the numerical simulation of the 2-D flame propagation process. The approach to a planar front is seen, as is the formation of the tulip structure and its propagation at a nearly constant velocity. For images (a) – (e) we have the normalized times $\bar{t}$= (0, 0.05, 0.125, 0.25, 0.35) where time is normalized with total combustion time.

A detailed analysis of the flow field of the burned gas during the expansion and subsequent quenching of the finger flame skirts by the cold wall shows a reversal in the direction of the local velocity field as the finger flame skirt nears the wall. A stagnation point along the centerline, also called a saddle point in our discussion, is formed near the left end of the tube where ignition occurred, marked with a blue dot in Figure 5.5. As will be shown here, this stagnation point propagates through the burnt mixture towards the flame front. The normalized position and

velocity of the flame front and stagnation point is shown along with numerous other curves in Figure 5.3.

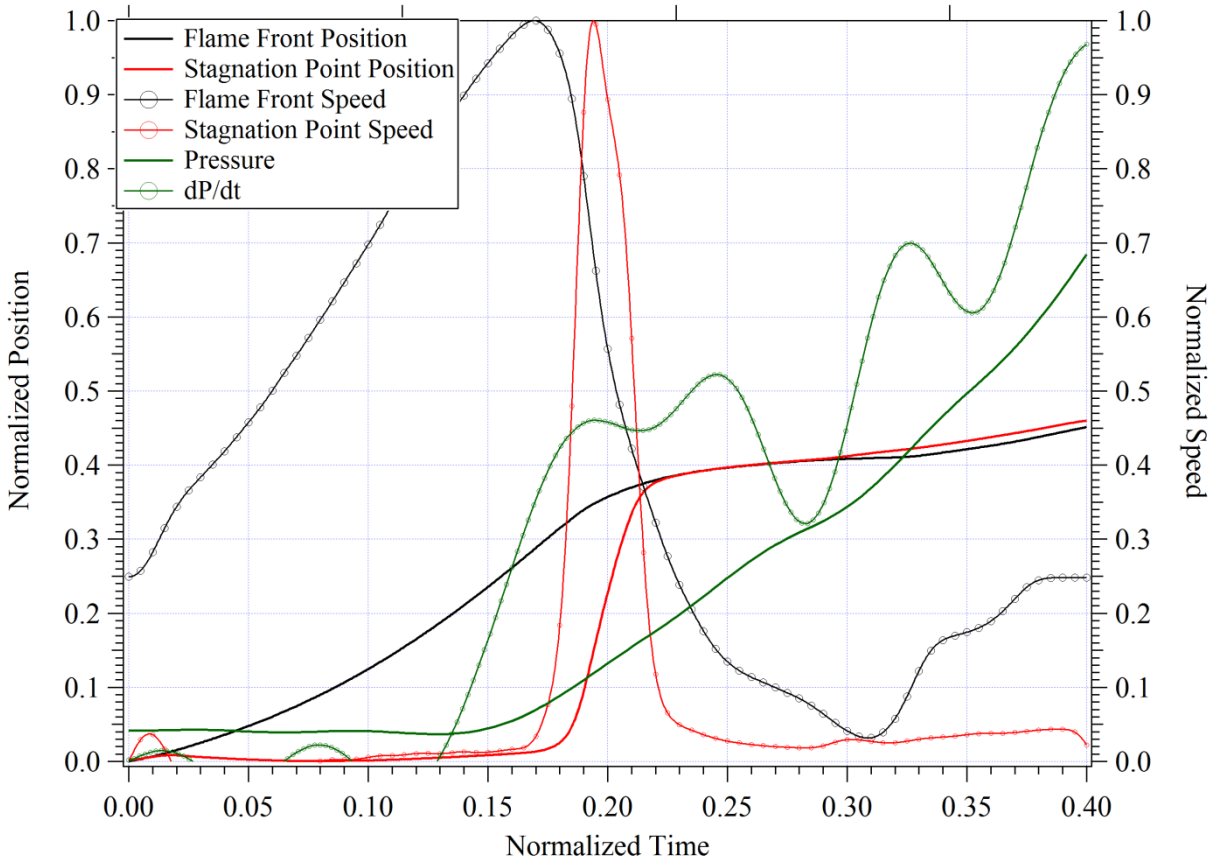

Figure 5.3: Normalized plot of the position and velocity of the flame front and the stagnation point as well as the pressure $\bar{p}(\bar{t})$, pressure change rate ($d\bar{p}/d\bar{t}$), stagnation front speed and flame front speed versus normalized time (t) in the channel. Flame position and speed are normalized with their maximum values.

Prior to the intersection of the saddle point with the flame front, the burned gases propagate towards, while the unburned mixture propagates away from, the flame front: this is the case during the initial stages of flame propagation (i.e., the spherical and finger flame stages). The speed of the flame front during the first two stages is higher than the local velocity field. In fact, as shown in Figure 5.3, the flame speed is high and continually increasing during the initial stages of combustion. The view is different in flame front coordinates, where the unburned gas moves

towards the flame front and the burned gases move away from the flame front towards the back of the channel. As the speed of the flame decreases toward the end of the finger flame stage, there is a reversal of direction for the burned gases and a subsequent reduction in the velocity magnitude in the unburned mixture.

Each tip of the finger flame skirt (there is one above and one below the centerline of the channel) induces the formation of a recirculation vortex. This vortex travels along the length of the tube as the finger flame collapses into a planar flame to eventually form the tulip flame. The recirculation flows on the upper and lower sides of the flame front create the stagnation point, which, as already noted, originates near the location of flame ignition. As the burn advances and the finger flame flattens and becomes a planar flame, the singular point accelerates towards the flame front. Dunn-Rankin (1988) has stated that "the recirculation produces the initial trigger for a Darrieus-Landau instability which subsequently grows to the full tulip". This statement is indeed predominantly true: the recirculation is crucial to the development and evolution of the flame structure. However, we do not believe the L-D mechanism is responsible for the evolution of the flame front into the tulip shape.

After the stagnation point intersects the flame front it passes through and emerges in front of the propagating flame. The structure of the stagnation point remains the same, with all of the velocity vectors near it pointing in the identical directions as before. This stagnation point then propagates in front of the flame in the unburned gas mixture but no longer accelerates with respect to the flame front, as shown by the flame front position and stagnation point position curves in Figure 5.3. The horizontal velocity component originating near the stagnation point and to its left is leftward, i.e., into the trailing flame front. For these three reasons, the tulip shape changes very little in this stage of combustion which, as a result, is rather steady as shown by the flame speed plot for the latter

half of the combustion event between normalized positions 0.45 and unity. In laboratory coordinates, the flow emanating from the stagnation point along the axis and behind it is opposed to the propagation direction. The position and velocity comparison between flame front and singular point is shown in Figure 5.3.

The nature and physical position of the singular point is consistent with the change of flame shape from "mushroom" to "tulip": when the stagnation point is behind the flame front its horizontal velocity is directed toward the flame front producing a higher centerline velocity that increases the flame centerline speed relative to the sides (skirts) closer to the wall which lag by comparison as the flame finger bulges toward the unburned gases ahead of it. This action serves to generate the flame's mushroom or finger shape. After the formation of the flame finger, the skirts begin to vanish while the recirculation cells grow in intensity and the flame becomes flatter. In this stage of burning, any enhanced centerline flow generated by the stagnation point toward the flame is overwhelmed by the backward velocity of the burned gases from the flame: the flame becomes successively flatter as the stagnation point approaches closer to the flame sheet. By contrast, when the stagnation point is in front of the premixed flame, its horizontal velocity opposes the center of flame relative to its sides enabling the formation of the cusp shape called the tulip flame. This action, it is clear, is consistent with the morphogenesis of the flame shape from finger (mushroom) to cusped (tulip).

Compatibility of Numerical and Experimental Results

Since the numerical simulations use one-step chemistry, the predictions of the numerical work will generally be qualitative. In order to ascertain whether the numerical simulation was adhering to the basic features of the experiment we evaluated channel pressure and flame shape evolution as the two principal of bases of our compatibility comparison. In order to make this comparison we normalized the computational duration with the maximum time (the burnout time) with abscissa $\bar{t}$=t/t_max. We also normalized the experimental and numerical pressures with their maximum values in our comparison. Shown in Figure 5.4 are the pressures evaluated numerically and from the pressure transducer.

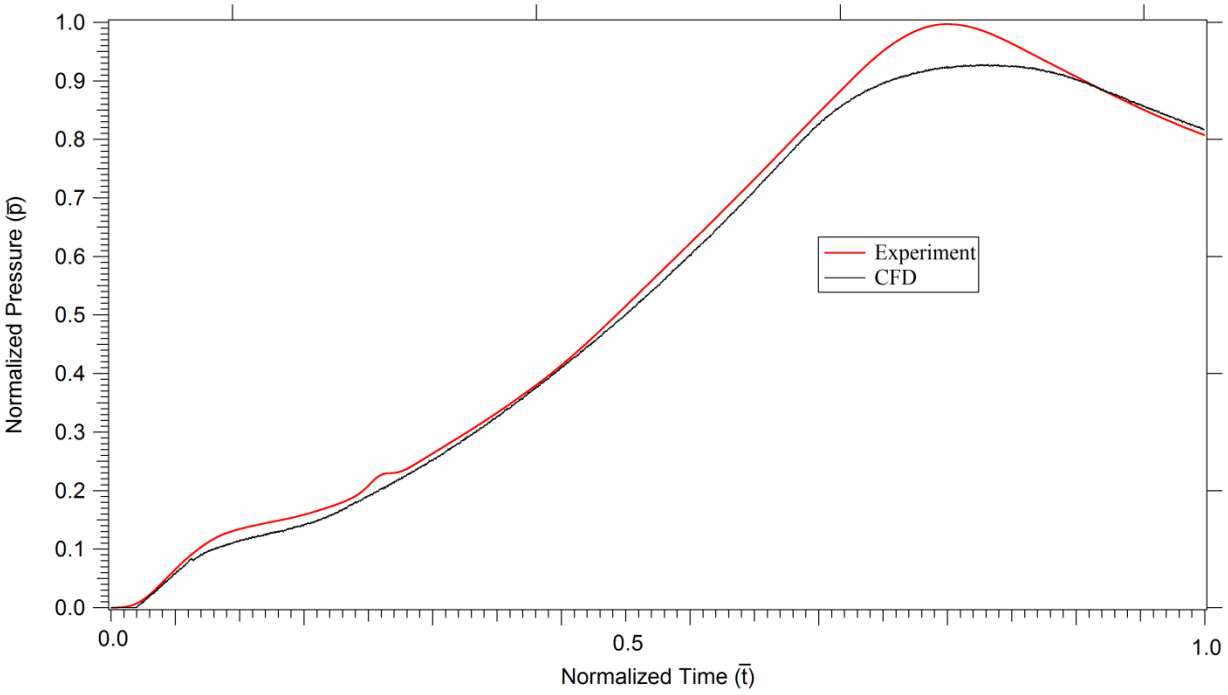

Figure 5.4: Plot of normalized pressure $\bar{p}$ versus normalized time $\bar{t}$ of combustion in the channel. This plot establishes a quantitative correspondence between experiment the simulation.

From the comparison it is seen that they are close and they display the same trends throughout the combustion process. The non-dimensional times of the peaks are virtually simultaneous and the $\bar{p}(\bar{t})$ oscillations in the "before" and "after" stages are also nearly identical. Regarding flame shape

evolution, the experiment shows that the flame is flat at 25 % of the total burn time, whereas the numerical solution yields a flat flame at 24 % of the total burn time. The experiment and the one-step chemistry simulation are therefore describing the same global sequence of events, properly spaced non-dimensionally with respect to the characteristic overall burn time.

Topological Analysis of Fluid-Flame Interaction

Using the velocity field obtained computationally, an analysis of the flow field structure was performed to determine its influence on the flame. The classification of fluid topology according to its Euler characteristic of the surface 'χ' applicable to a complex fluid flow using critical point concepts was developed by Perry and Chong (1987).

Under this methodology, the Euler characteristic for a surface in the flow field is represented by $\chi_{surface} = \chi_{sphere} - 2\Sigma Handles - \Sigma Holes = \sum Nodes - \sum Saddles$. In an alternative methodology, presented by Foss, the Euler characteristic equation can be written in a more easily used form:

$$\chi_{surface} = (2\sum N + \sum N') - (2\sum S + \sum S'). \quad (5.1)$$

In Equation 5.1, the half nodes (N') and half-saddles (S') appear on the perimeter (boundary) of the *2-D* surface under consideration whereas the nodes (N) and saddles (S) appear in the interior of the control volume.

During the propagation of the flame in a closed combustion chamber, the half-saddles and half-nodes describe the nature of singular points at the walls. The saddle created during ignition, an internal singularity, propagates towards the flame only after the flame skirts are quenched by the side walls. The propagation of this saddle point, along with the generation of other nodes, half-nodes, saddles and half-saddles is examined in detail.

Spherical Flame: Upon ignition, a hemispherical flame front develops, whose radius rapidly increases along with the fluid flow velocity inside the control volume. The flow streamlines superimposed onto the reaction contour are shown in Figure 5.5.a. A stagnation point formed at the instant of ignition moves very slightly rightward along the centerline as the spherical flame

grows. Using the streamline as a guide, we can identify the various topological features marked on Figure 5.5.a. There are two nodes, three half-nodes, three half-saddles and one saddle. The Euler characteristic number for the control volume is calculated from Equation 5.1 as $\chi = 2$. A recirculation vortex, created close the wall in the unburned mixture after ignition, is attenuated by the boundary layer.

Finger Flame: The spherical flame expands faster along the length of the combustion chamber compared to its sides. This elongation of the flame front causes it to resemble a finger. The ends of the side skirts where the premixed flame is quenched generate two singular points (half-nodes *N'*) which propel the saddle point along the centerline axis of the channel. The finger flame topology contains two nodes, two half-nodes, two half-saddles and one saddle point as shown in Figure 5.5.b. The Euler characteristic of the finger flame flow field is computed from Equation 5.1 as $\chi = 2$.

Planar Flame: The flame front flattens as the singular point moves closer to the flame front. It is exactly planar at the instant when the reaction front and the singular point (saddle) coincide. A recirculation pattern is created in both the burned and unburned mixtures as the side-skirts are quenched by the cold side walls. This transforms the half-nodes in the burned gas region into a free standing pair of nodes and half-saddles (*S'*). The control volume contains four nodes, four half-saddles and one saddle. The Euler characteristic is computed from Equation 5.1 as $\chi = 2$, see Figure 5.5.c.

Tulip Flame: The stagnation point eventually moves *through* the flame front and travels at a fixed distance from the tulip cusp at the centerline of the channel as the flame moves towards the far (right) end of the channel. This increases the velocity of the unburned mixture travelling towards the centerline of the flame (tulip cusp) which acts as a source for flame stretch. The flame area

now increases to its tulip value, the propagation speed of the front is nearly constant, and this entire structure moves as a coherent unit until the final (extinction or quenching) stage of the combustion process in the channel. The control volume contains four nodes, four half saddles and one saddle. The Euler characteristic is computed from Equation 5.1 as $\chi = 2$, see Figure 5.5.d. See also Figure 5.3, which shows that the flame front and saddle point separation remains constant after the saddle passes through the flame.

The Euler characteristic of the fluid flow in the combustion chamber remains constant throughout the flame propagation process irrespective of the shape of the flame front. The number and type of singular points changes for different stages during flame propagation but the flow topology, in terms of the Euler characteristic χ, remains invariant.

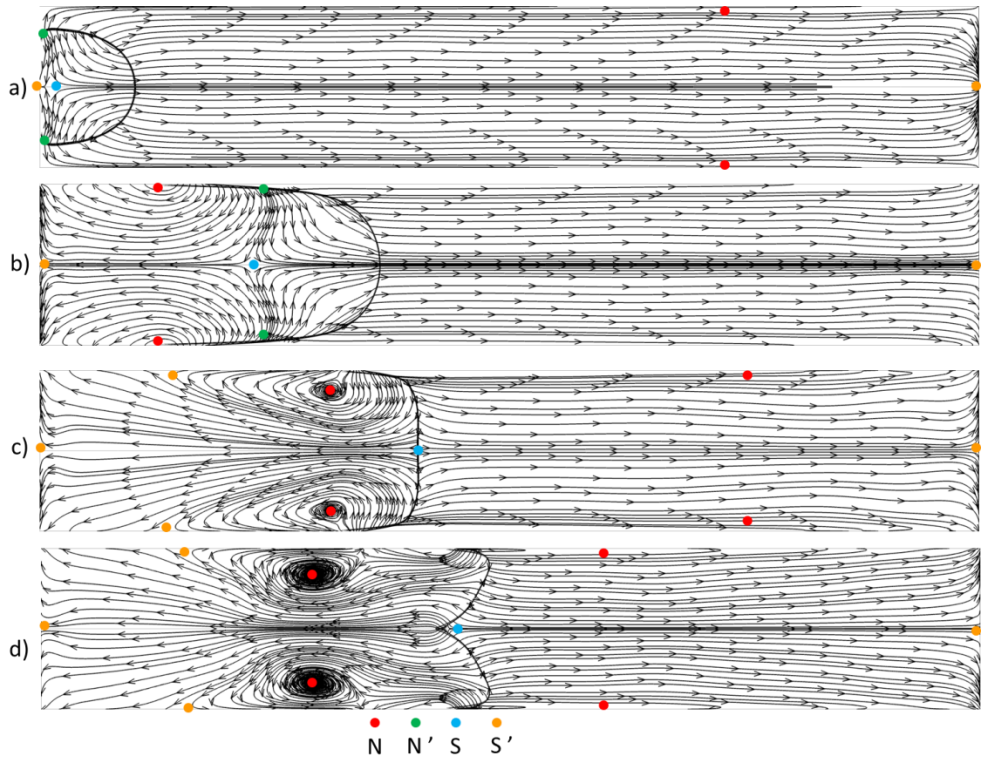

Figure 5.5: Plots of the streamlines in the channel at various instants during the combustion process. a. Ignition stage; b. Finger flame stage; c. Planar flame stage; d. Propagating tulip flame stage. Shown in each figure are the nodes (N), saddles (S), half-nodes (N') and half-saddles (S'). The Euler characteristic remains constant for the entire combustion process at $\chi = 2$.

Numerical Results and Topographical Analysis – 2 Sparks

Numerical Results and Topographical Analysis – 2 sparks

The 3-D numerical simulation model consists of a combustion chamber measuring 30 cm long and having a 5 cm x 5 cm cross-section, which is identical with the experiment. The domain contains 48 million cells of cubic elements measuring 0.25 mm on each side. The walls of the combustion chamber are modelled as isothermal with their temperature set at 300K. A flame-front tracking code, using a scalar variable, c, to track the progress of reaction from unburnt to burnt mixture is used to model the burning process as derived by Zimont (2000). The unburnt mixture has a value of $c = 0$ and the completely burnt mixture has a value of $c = 1$.

In this article, the flame front location is marked by the cells where the value of the reaction progress variable is 0.5. Three cases of 2-spark combustion, with ignition delay 0, 25 and 50 ms were studied. The simulation results were compared with experimental and 2-D models (with Arrhenius chemistry), and were found to be topologically accurate. The detailed three-dimensional structures of the tulip flame formation and the flow field evolution inside the burnt and unburnt regions was obtained from the numerical simulation, and will be discussed in detail below. The flow velocity streamlines are shown on a plane, which runs along the length of the combustion chamber, and cuts the square cross-section diagonally.

Spark Delay – 0ms

Here, the sparks are initialized by patching a spherical region of radius 2 mm having burnt gas conditions (i.e., elevated temperature corresponding to combusted gases in a premixed flame) on both ends of the CV combustion chamber. The numerical code runs until the opposing tulip flames collide with each other. The average static pressure and progress variable are monitored through the numerical simulation. An isometric view of the flame front for select times is shown in Figure 5.6. The position of the flame front obtained experimentally and numerically is shown in Figure 4.8**,** which provides a direct comparison with the experimentally recorded flame front position. From Figure 4.8, it is observed that the numerical solution reproduces the spatial and temporal propagation of the flame with high accuracy. Both the qualitative and quantitative features of the flame front propagation process are accurately rendered by the model. These numerical results are post-processed to deduce the flow-field conditions inside the combustion chamber and to study the evolution and propagation of stagnation points.

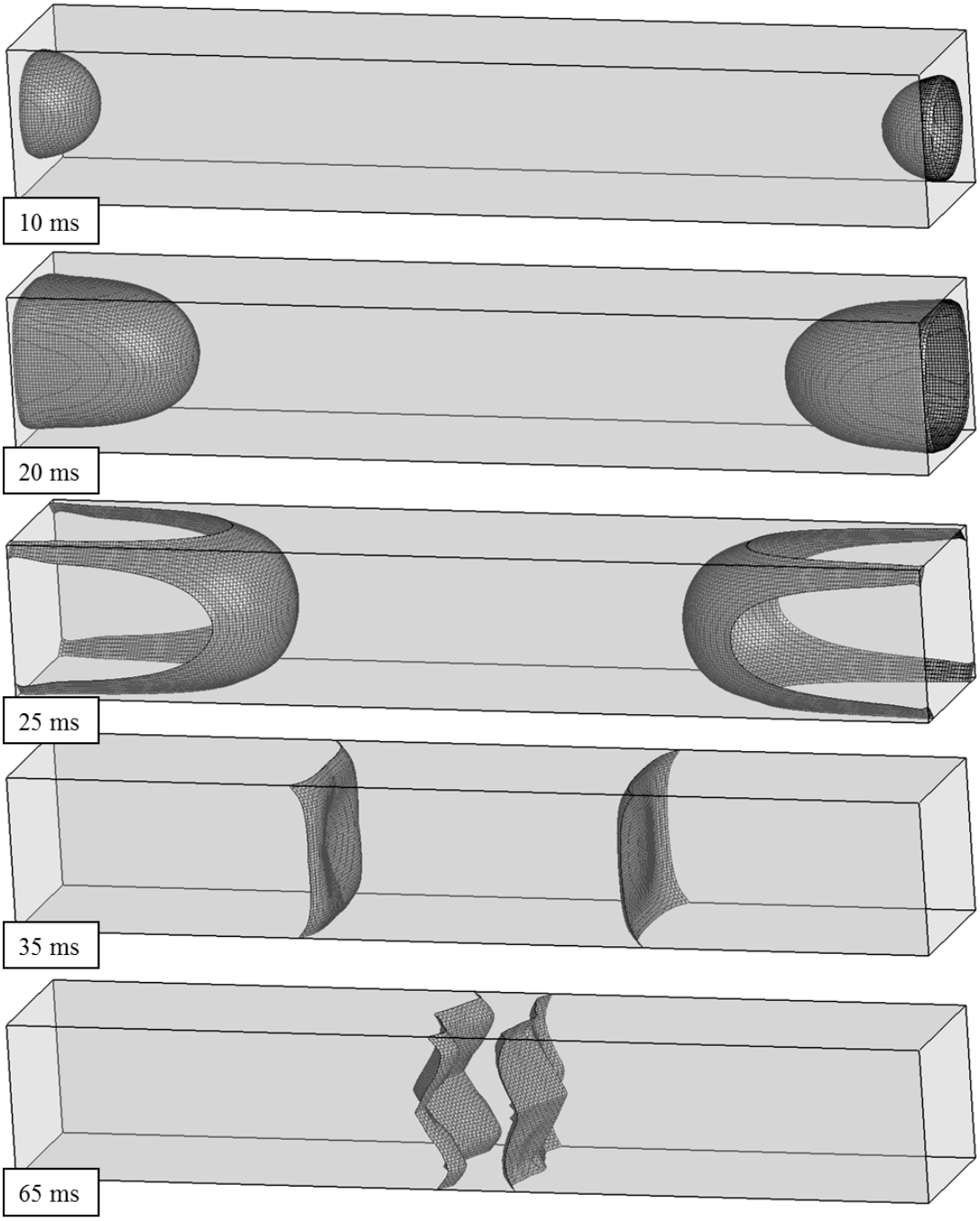

Figure 5.6: Isometric view of the flame front.

Spark Delay – 25 ms

Here, as in the previous case, a spark is initialized at the left side of the combustion chamber and after 25 ms, another spark of radius 2mm is initialized at the right side. The average static pressure and progress variable are monitored. The orthogonal view of the flame front propagation for select time intervals is shown in Figure 5.7. The position of the flame front obtained experimentally and numerically is shown in Figure 4.11. From the figure, it is observed that the numerical simulation accurately reproduces the spatial and temporal characteristics of the laboratory flame front.

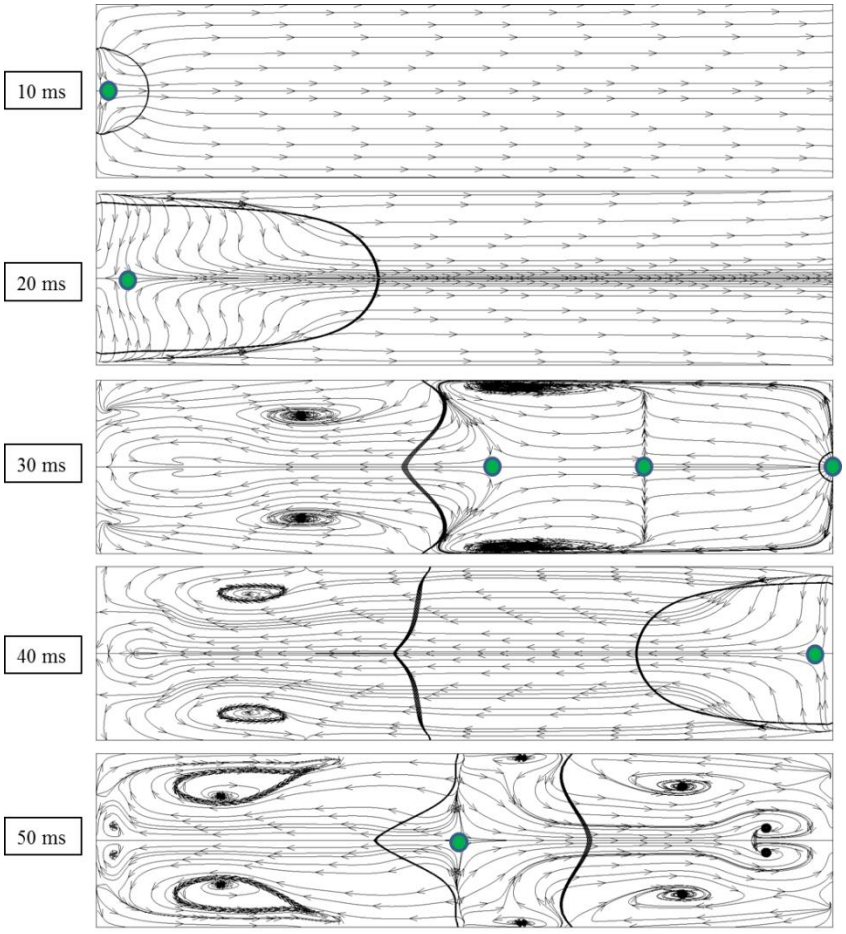

Figure 5.7: Orthogonal view of flame front with streamlines.

Spark Delay – 50 ms

Following the procedure of the previous two sub-sections, the 50 ms delay case was also examined numerically. The orthogonal view of the flame front propagation for select time intervals is shown in Figure 5.8. The position of the flame front obtained experimentally and numerically is shown in Figure 4.14.

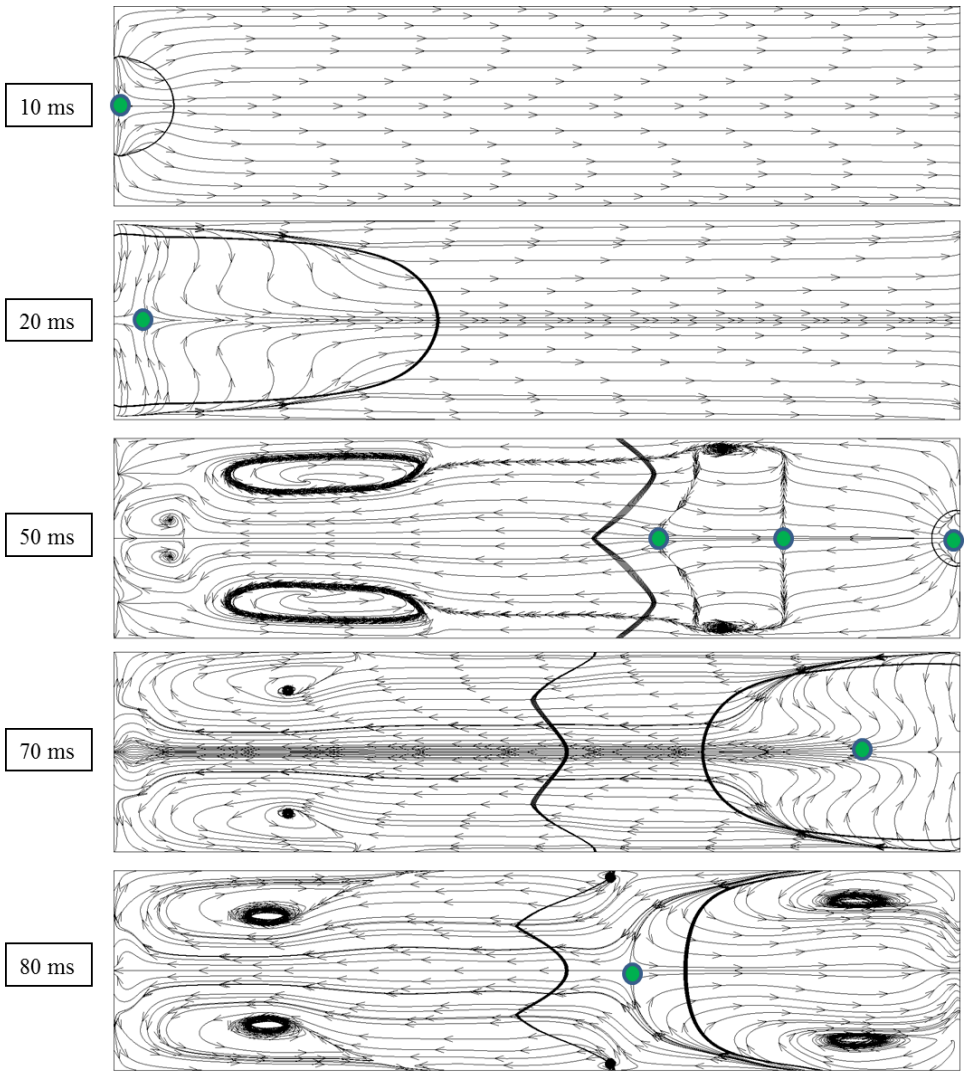

Figure 5.8: Orthogonal view of the flame front with streamlines.

CHAPTER 6

DISCUSSION OF EXPERIMENTAL AND NUMERICAL RESULTS

Spark Delay – 0ms

We discuss two aspects of the numerical simulations. One of these aspects is the direct comparison of the experimental and numerical results. The other is a detailed discussion following Hariharan and Wichman (2014) of the structural features of the flow field associated with this CV flaming process.

We begin with the direct comparison of the experimental and numerical results. Figure 4.8 shows that the flame positions are nearly identical throughout the CV burn, with differences only occurring when the flame undergoes its most dramatic accelerations and decelerations up to the time it undergoes transition into a tulip flame. The numerical solution is symmetric, whereas very slight asymmetries are observed in the experimental results. We note, however, that despite minor differences, not only is the quantitative flame position very accurately predicted, but the qualitative appearance of the flame fronts is very accurately rendered. The numerical flame fronts undergo initial expansion, finger flame acceleration, flame skirt induced slowdown, transition to tulip flame shape, tulip flame propagation at slower speed, and finally extinction (annihilation). All of these characteristic physical events align timewise in the combustion sequence. The pressure fields can also be directly compared. The average static pressure inside the combustion chamber for the experimental and numerical results, normalized to the experimental pressure is shown in Figure 5.4.

We now discuss the details of the numerically simulated flow features, in terms of our previous work (Hariharan and Wichman (2014)). In Figure 6.1 we see the streamlines of the flow fields inside the combustion chamber along the diagonal cross section.

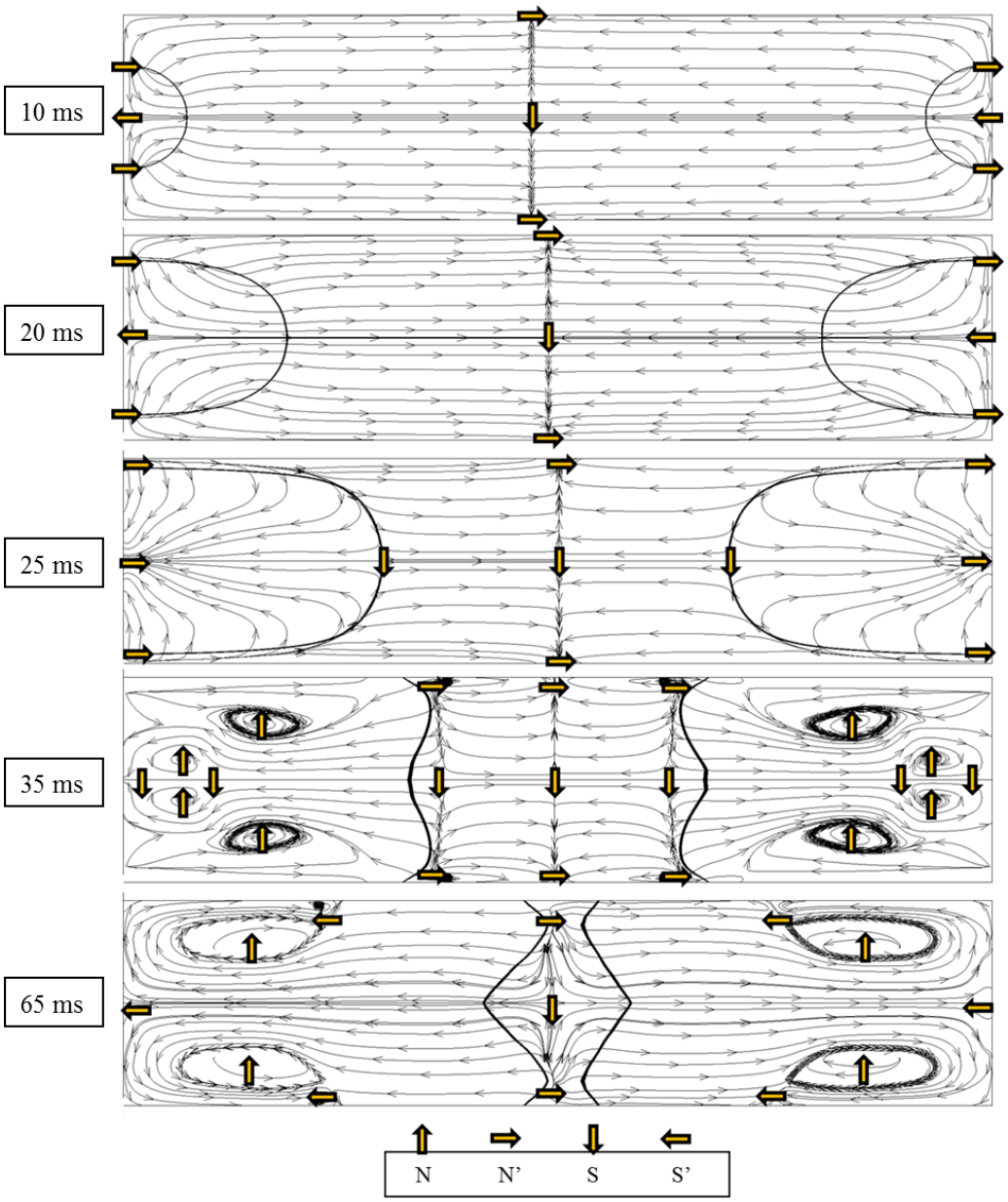

Figure 6.1: Streamlines and flame front position for 0ms spark delay.

The characteristic topological features of the flow field are marked. As described in Hariharan and Wichman (2014) the classification of the fluid topology according to its Euler characteristic of the

surface 'χ', which is applicable to a complex fluid flow using critical point concepts, was developed by Perry and Chong (1987). Under this methodology, the Euler characteristic for a surface in the flow field is represented by $\chi_{surface} = \chi_{sphere} - 2\Sigma Handles - \Sigma Holes = \sum Nodes - \sum Saddles$. An alternative methodology was presented by Foss (2004). Here, the Euler characteristic equation can be written in a more readily used form:

$$\chi_{surface} = (2\sum N + \sum N') - (2\sum S + \sum S'). \quad (6.1)$$

The preceding classification will be used to name the topological features for the rest of this article. At t = 10 ms, there are two half-saddles located near the ignition points. There is a saddle created at the centerline along the axis of the combustion chamber. Two half nodes are created close to the cold walls at the center of the combustion chamber and four more half-nodes are created where the flamelet collides with the cold wall. The Euler characteristic for the flame topology for this spherical flame is $\chi = 2$. At t = 20 ms, the topological features remain the same and the Euler characteristics remains $\chi = 2$. At t = 25 ms, there are two saddles located axially at the flame front location, and also a saddle at the centerline. There are also two half-nodes located close to the ignition points axially. Four additional half nodes are located at the side-skirts of the flame, where the flame front touches the cold wall. Two half nodes and one saddle are positioned at the center of the combustion chamber. The Euler characteristic for this flame topology remains $\chi = 2$. At t = 35 ms, the two saddles, which were previously located axially on the flame front, move in front of it. The two half nodes near the cold walls also have moved from behind to the front of the flame. Additionally, there are four half-saddles created just behind the flame front. There are four nodes located at the recirculation vortices, and four saddles behind the recirculation vortices. Additionally, there are four half-nodes created at the cold wall near the ignition points. The Euler characteristic of the flame front topology, however, is still $\chi = 2$. Later, at t = 65ms, there is one

saddle and two half-nodes located near the center of the combustion chamber. There are two half saddles located at the centerline axis near the ignition points. Four nodes are located at the recirculation vortices and four half-saddles are located just in front of the recirculation vortices. The Euler characteristic of this flame topology is $\chi = 2$.

It is interesting to note that in the one-spark study of Hariharan and Wichman (2014) the Euler characteristic was always $\chi = 2$ and for symmetric two-spark case, that value is maintained. It is not clear to us exactly what this implies because, as we shall see, the asymmetric cases to be discussed below do not have constant Euler characteristics during any stage of propagation. Until we learn more about this particular aspect of the flow field, the discussion is largely speculative and suggestive rather than quantitatively predictive. However, in all of our discussions of this topic one fact stands out among all others: the transition from a flame front whose curvature is initially toward the ignition point, to a flat flame front that then morphs into a 'tulip' flame is accompanied by the movement of the stagnation point behind the flame to the flame front to a nearly fixed position in front of it, respectively. This centerline stagnation point always performs this motion during the transition into a tulip flame and thus, we associate its formation and motion indelibly with the transition process.

Spark Delay – 25 ms, 50 ms

Detailed topographical analyses of the 25 ms and 50 ms spark delay simulations are not performed as the flow field becomes complicated once the second spark is ignited. However, the locations of the saddle points along the centerline of the combustion chamber are tracked throughout the combustion process and are shown in Figure 5.7 and Figure 5.8.

CHAPTER 7

MICROGRAVITY DIFFUSION FLAMES

The study of microgravity diffusion flame spread has its primary applications in fire safety. The support structure and display panels of space habitats use combustible plastic materials, due to their low thermal/electrical conductivity and light weight and high strength. While the properties of flame spread over these plastics can be easily quantified for earth-gravity, the flame spread properties in microgravity are not readily available. The National Aeronautics and Space Administration (NASA) Glenn Research Center in Cleveland, Ohio studies microgravity flame spread through the Analysis of Thermo-diffusive and Hydrodynamic Instabilities in Near-extinction Atmosphere (ATHINA) initiative. The facility has a drop-tower, which can be used to study flame propagation in free-fall. The use of this drop-tower is both expensive and the free-fall microgravity environment lasts only between two to five seconds in total. Additionally, an aircraft flying in a parabolic trajectory has also be used. The aircraft, nicknamed the "vomit comet" typically provides about 30 seconds of microgravity during its descent phase. Similar to the case of the drop-tower, conducting tests on the aircraft is both expensive and provides only a maximum of 30 seconds of test time. The third method to test microgravity flame propagation is to use the Microgravity Science Glovebox, located aboard the International Space Station (ISS). This facility provides a true microgravity environment lasting several minutes. The experiment burn-time is constrained by the amount of oxygen available and the cost associated with sending samples to Low-Earth Orbit (LEO).

To simulate microgravity environment without using expensive methods (drop-tower, aircraft, space stations) and to provide a longer burn time, an apparatus was developed in which a solid fuel could be burned in a confined channel with its height small enough to suppress buoyancy effect,

but not so small as to suppress the flame through heat loss to the walls. Versions of this apparatus are being studied in NASA Glenn Research Center, San Diego State University (SDSU) and at Michigan State University (MSU). Each team's experimental apparatus has been designed slightly different and is intended for different purposes. This apparatus, called the "Hele-Shaw apparatus" does not provide a true zero-gravity environment, but simulates one by suppressing buoyant flow, and has the disadvantage of acting as a large heat-sink near the burning sample. However, it offers a longer test-time, easy interchangeability of test samples, varied sizes of samples, and can also be easily modified. To investigate the spread of diffusion flames over thick PolyMethyl MethAcrylate samples in microgravity conditions, a Narrow Channel Apparatus (NCA) is used. The NCA consists of a duct with a sample holder with a variable top wall height to restrict the effect of buoyancy. The schematic representation of NASA's NCA is shown in the figure 7.1 below.

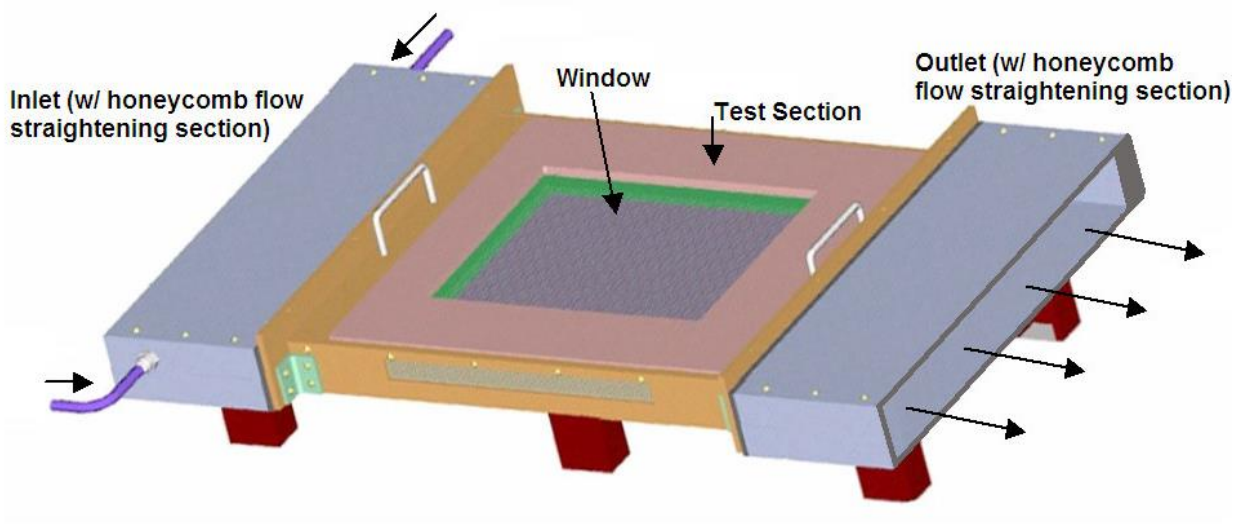

Figure 7.1: Narrow Channel Apparatus representation.

The NCA consists of three parts – inlet plenum, sample section and outlet chamber. The inlet plenum consists of aluminum housing with ports provided for the inlet of air from the mass flow controller to maintain specific flow rates. Glass bead diffusers and a honeycomb mesh are used in the inlet plenum to ensure a laminar air stream enters the sample section.

The sample section, which is attached to the inlet plenum, consists of an aluminum base with a glass plate on the top and sides to enable visual observation of the flame spread. The sample is held in place using an insulated base made of fiberboard material. Sufficient space is provided between the inlet plenum and sample to ensure the incoming flow is fully developed. An ignition wire is placed just above the trailing edge of the PMMA sample to enable ignition. The optical window consists of a quartz glass plate which is flush-mounted on the aluminum frame. Optional side windows are used to track the side-view profile of the flame. The test section is attached to the outlet chamber, which consists of an aluminum chamber. The outlet chamber is used to sample exhaust gas for unburnt hydrocarbon and CO/CO_2 analyzers. The outlet chamber is connected to the fume hood to expel the exhaust gas.

To restrict buoyancy, the top glass plate of the test section is lowered such that the gap between the top surface of the PMMA sample and the glass plate is 5mm. The mass flow rate of air required to maintain a specific average velocity is computed and supplied by the mass flow controller. The representation of the diffusion flame spread is shown in Figure 7.2.

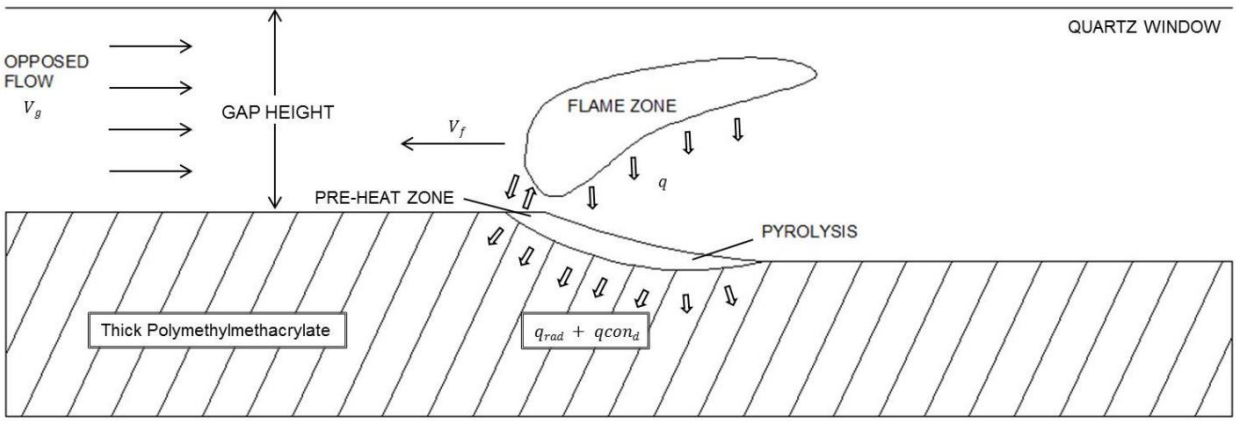

Figure 7.2: Representation of the diffusion flame spread over thick PMMA in a NCA.

This project continues the previous experimental research done at Michigan State University by Oravecz (2001) and Tanaya (2004). Prior to the research at MSU, theoretical analyses of thin solid fuel combustion were conducted by deRis (1969) and Fernandez-Pello and Williams (1995, 1997). Additionally, works by Wichman and Williams (1983) present a simplified model, based on the results of deRis, that applies to solid fuel flame propagation with an opposed oxidizer flow.

Experimental Procedure

The sample surface is first cleaned with a soft cloth to remove dust, and it is placed on the insulation surface. The gap between the sample and insulation surface is eliminated upstream by using an adhesive tape. This ensures that the air flow over the insulation/sample is smooth and continuous. It also holds the sample in place. The Kanthal ignition wire is placed at the downstream edge of the sample, suspended just above the sample surface. The required flow velocity is entered in the LabView interface, which calculates and sets the required volume flow rate of air in the mass flow controller. Once the mass flow controller reaches steady state, the Kanthal wire is connected to the auto-transformer which causes the sample to pyrolyze and ignite. The ignition wire is left connected to the autotransformer for exactly one minute, after which it is disconnected and physically removed from the NCA. The total time the ignition wire is turned on is kept constant, irrespective of the time taken by the sample to ignite to ensure constant heat is used to ignite the sample. In general, thicker samples and higher flow rates take longer to ignite when compared with thin samples and low flow rates.

Experiments to quantify the spread rate are performed by both varying the opposed flow oxidizer speed for a fixed duration and changing it once the flame reaches steady state and by holding a single opposed flow speed until the entire sample is consumed. The spread rate data are then compared for both multiple flow rates per sample and single flow rate. The time taken to reach a steady state condition after a change in flow rate is calculated experimentally to be approximately 20 minutes for a change of 20 cm/s. This time can further be reduced if the difference in the flow rate between subsequent data points is not drastic. Typically, the change in the flow rate between subsequent data points is 1-2 cm/s.

Experimental Results

The PMMA samples are machined to be 2 inch wide and 5 inches long. Markings are made with a razor blade at fixed distances in order to calibrate the camera and to reduce parallax error. The PMMA samples tested are either clear or black dyed. The samples are 0.25, 0.5 and 1 inch thick and the mass flow controller has the capacity to supply air between 0 and 70 cm/s at 1cm/s increments.

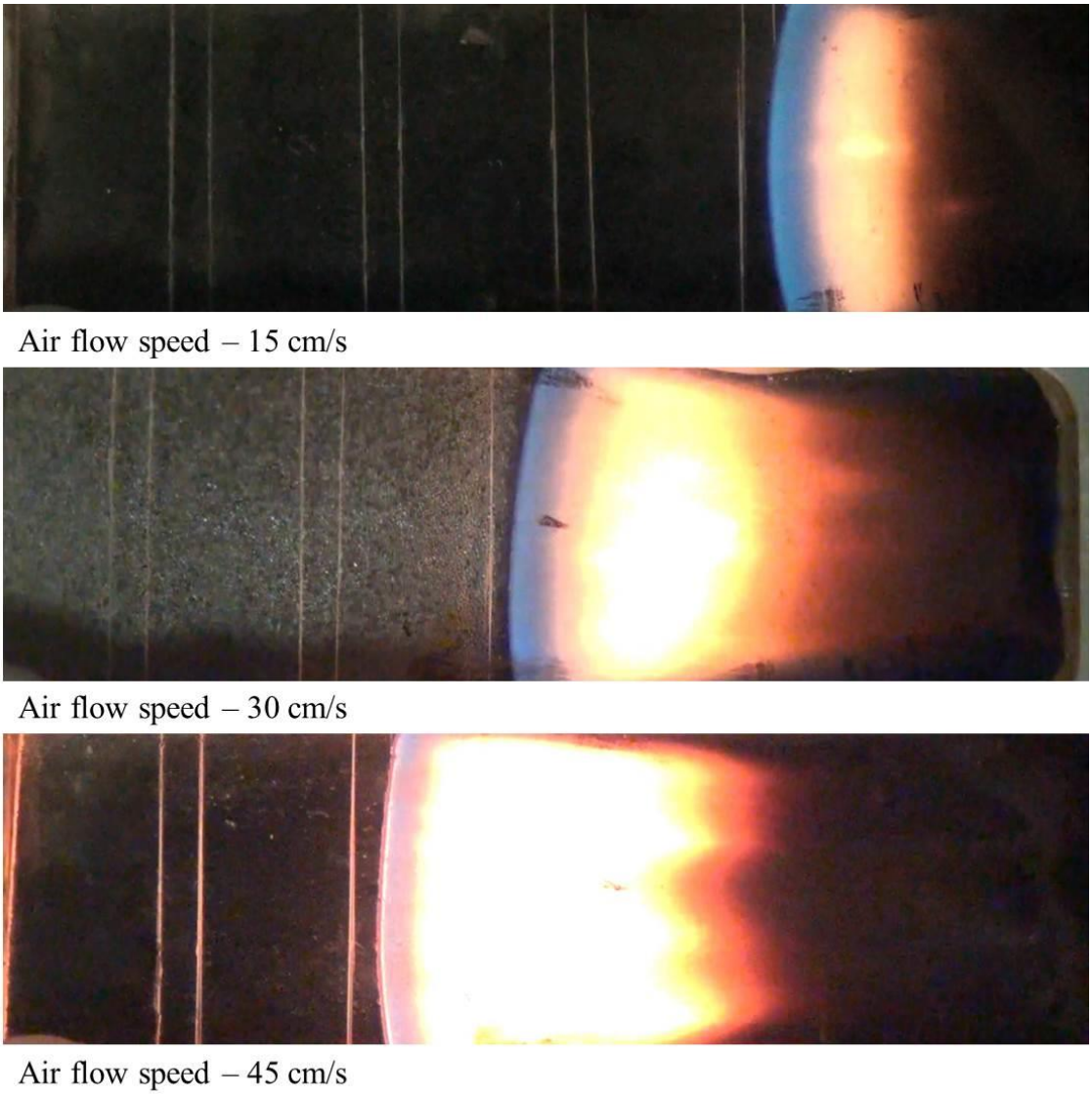

Figure 7.3: Diffusion flame over PMMA samples at different flow rates.

The snapshot image of the video recording is shown in Figure 7.3. It is observed that the flame spread rate, length of visible flame and the flame profile changes with change in the opposed flow velocity.

Three distinct regimes are observed for varying opposed flow speeds. These three regimes are classified as follows – Normal Flame Spread; Flame Spread over Surface; and Flamelet Regime. The three regimes are classified according to the type of flame spreading over the surface and also the shape of the burnt sample. Figure 7.4 shows the picture of the burnt sample for a test which has been abruptly extinguished from certain opposed flow speed (26 cm/s). This enables detailed analysis of the pyrolysis profile at different oxidizer flow speeds.

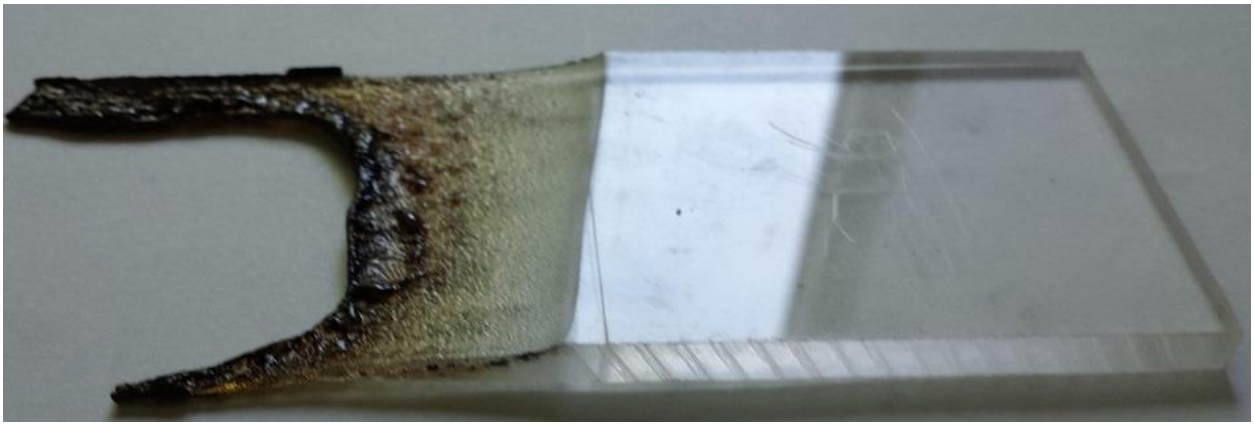

Figure 7.4: Burnt sample of PMMA for 26 cm/s opposed flow speed.

The pyrolyzing surface is angled uniformly with the horizontal and the entire thickness of the sample is burnt off. This can be seen in the above figure. The flame is anchored just behind the pyrolyzing tip. The unpyrolyzed residue on the two sides of the samples is the result of heat transfer between the PMMA and the insulation. The flow velocity, which produced the characteristic pyrolysis profile, is designated as the normal flame spread regime.

Figure 7.5 shows the picture of a burnt sample for a test that has been abruptly extinguished from a certain flow speed (12 cm/s). This enables a detailed diagnostic of the burn profile at different speeds.

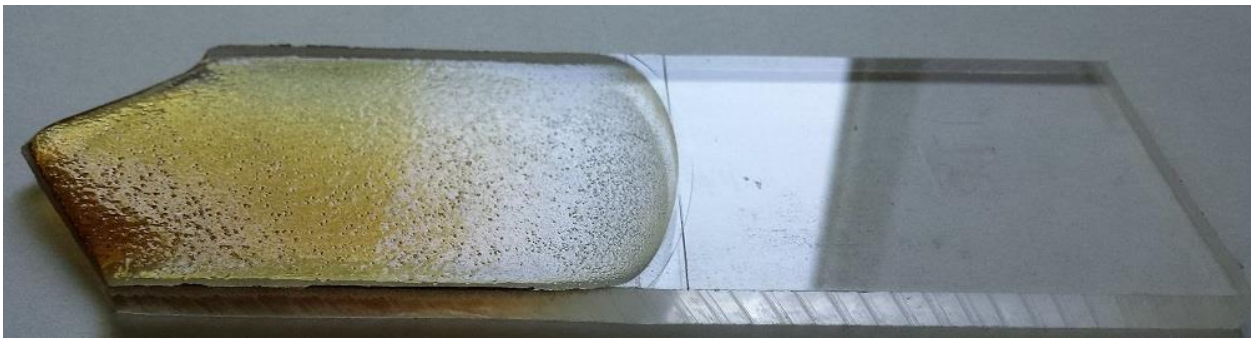

Figure 7.5: Burnt sample of PMMA at 12 cm/s.

The pyrolysis occurs only at the top 1 mm of the sample, leaving behind a 5 mm thick unpyrolyzed surface behind the flame front. The flame spreads over the sample surface at a higher speed when compared to normal flame spread. The primary reason the sample behind the flame is unpyrolyzed is the reduced availability of oxidizer, which reduces the intensity and length of the flame. The smaller flame is experimentally observed to have a vertical tilt, which further reduces heat transfer downstream of the flame. The regime under which the flow velocity produces the characteristic surface is classified as “Flame Spread over Surface”. It is experimentally observed that this regime exists only over a narrow range of flow velocities of air. The flame spread rate observed during this regime is higher than the other two regimes and the flame length is also the lowest.

Figure 7.6 shows the picture of a burnt sample for a test that has been abruptly extinguished at a certain flow speed (6 cm/s). This enables a detailed diagnostic of the burn profile at different speeds.

Figure 7.6: Burnt sample of PMMA at 6 cm/s.

The flamelet regime occurs when the opposed flow rate is reduced below a threshold value when the flame width reduced and a flamelet forms. This is observed in Figure 7.7.

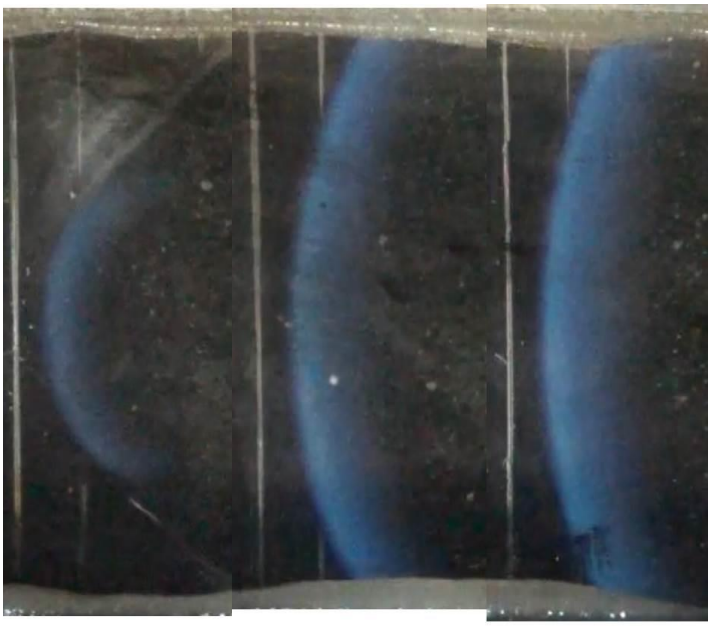

Figure 7.7: Flame spread at reducing flow rates, showing transition between flame propagation over surface to flamelet regime.

The flamelet formed during this regime spread upstream at a very slow rate, when compared with the other two regimes. The flamelet appears to dig into the sample, instead of moving forward.

The flamelet continues to dig in until it reaches the bottom of the sample, upon which it bifurcates and moves upwards as two flamelets. Once the two flamelets reach the top surface of the sample, they recombine to form a new flamelet. This process repeats as the flamelet spreads forward slowly. The flamelet formed is unstable and a minor variation in the opposed flow rate of oxidizer can either quench the flamelet, when the flow velocity reduces, or stop the downward pyrolysis, if the flow velocity increases.

The flame spread rate for ¼", ½" and 1" thick clear, cast PMMA samples are shown in Figure 7.8, Figure 7.9 and Figure 7.10.

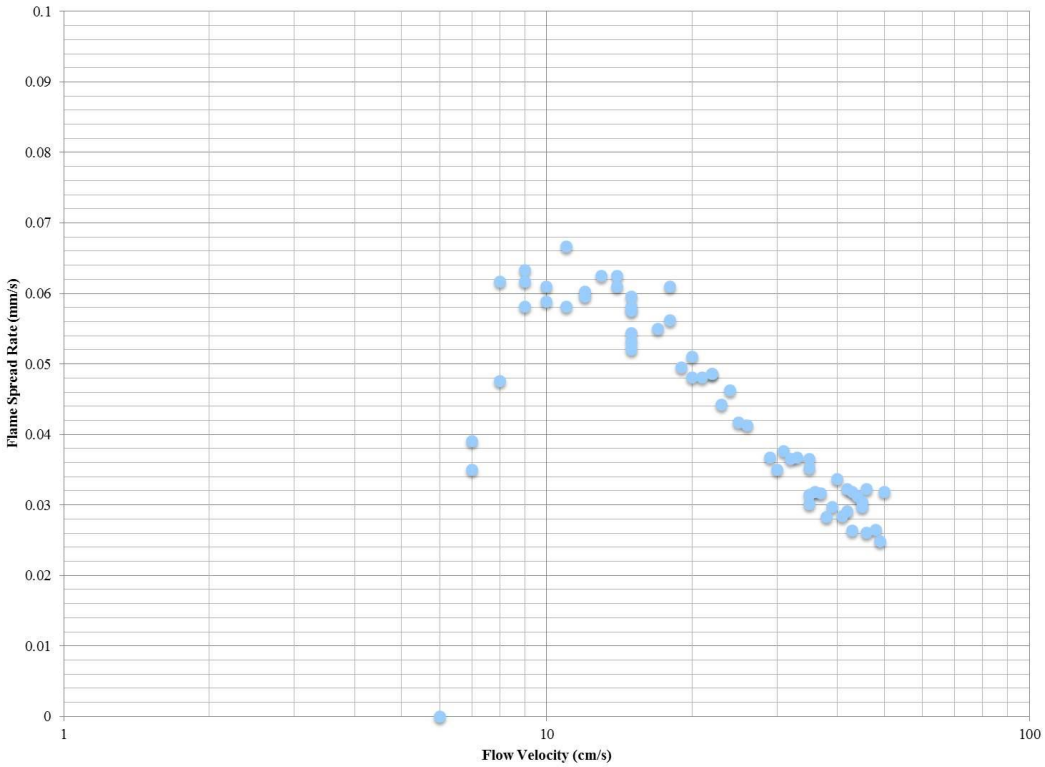

Figure 7.8: Flame spread rate vs. flow velocity for ¼" thick PMMA samples.

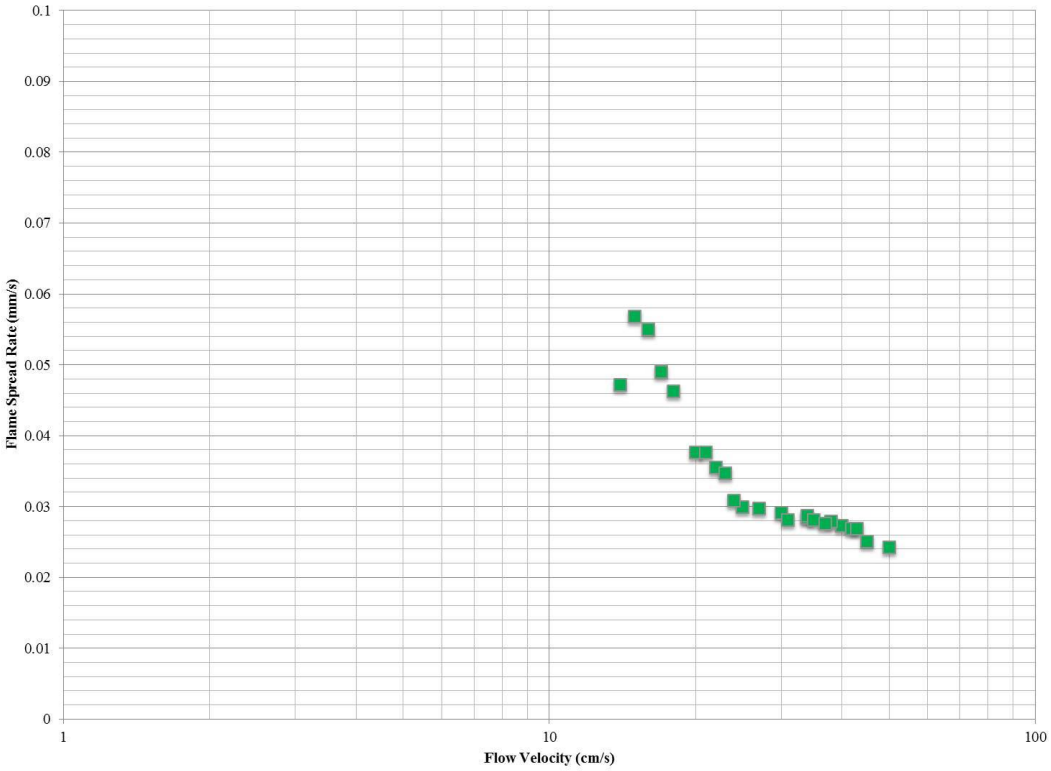

Figure 7.9: Flame spread rate vs. flow velocities for ½" thick PMMA samples.

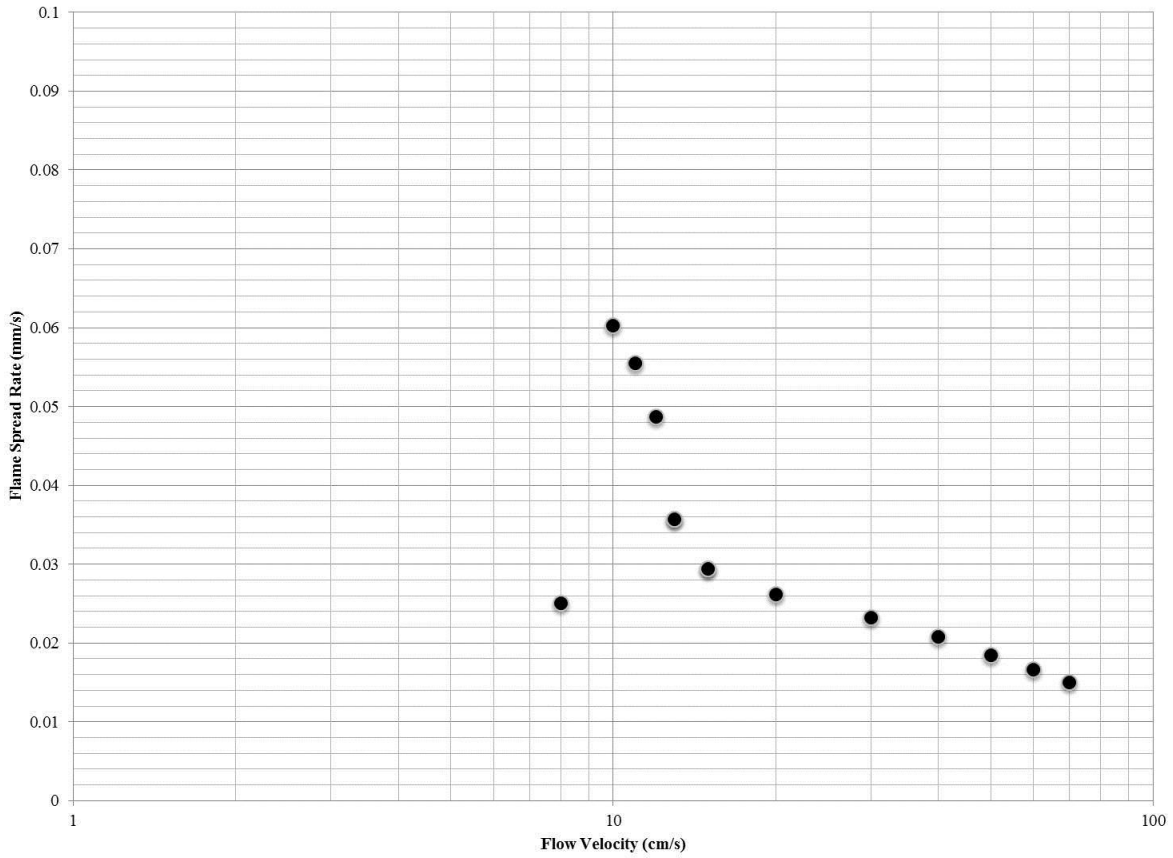

Figure 7.10: Flame spread rate vs. flow velocities for 1" thick PMMA samples.

It is observed that the peak flame spread rate is approximately 0.06 mm/s. This maximum spread rate is similar irrespective of the thickness of the sample. This peak spread rate occurs when the flame is propagating over the surface with only the top 1mm of the sample pyrolyzing. This leads to a thickness independent spread rate. Figure 7.11 shows the spread rate for all three sample thicknesses.

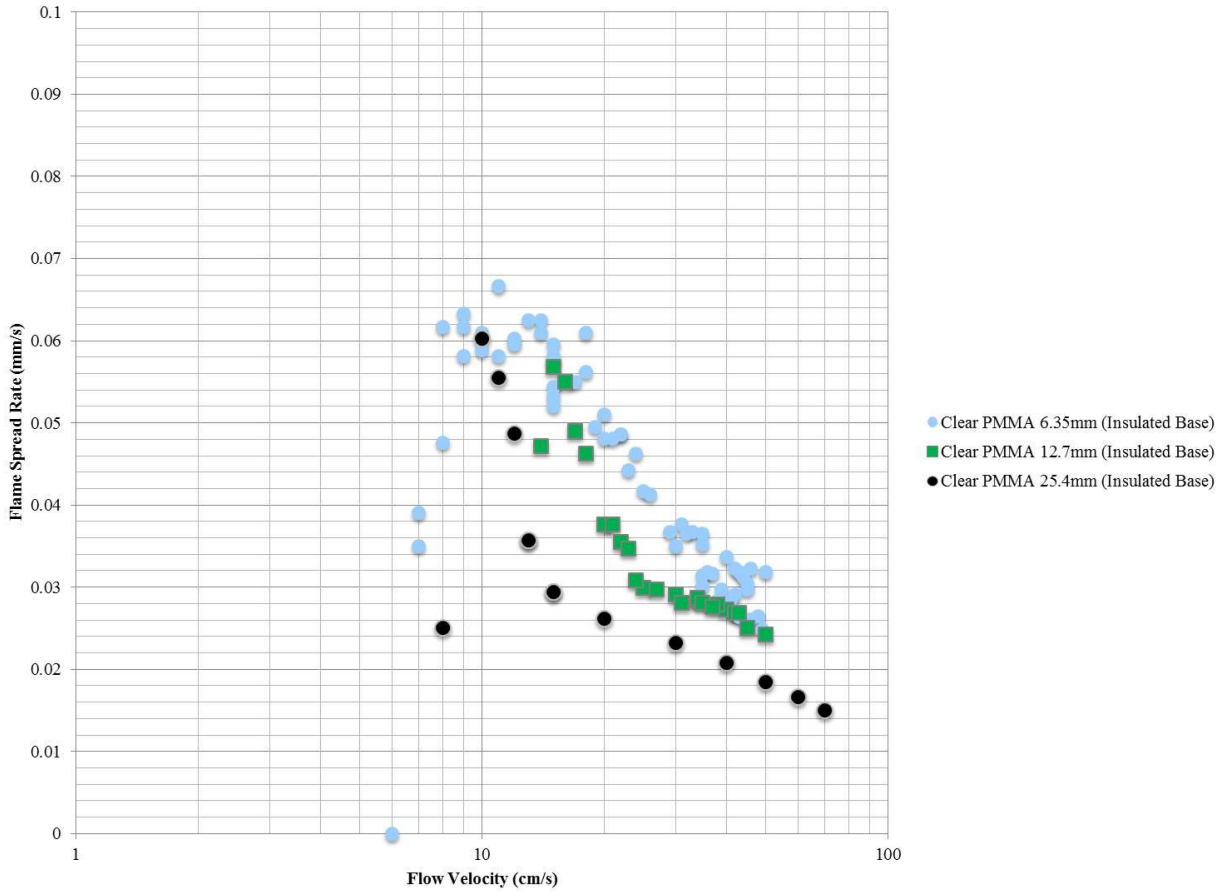

Figure 7.11: Flame spread rate vs. flow rate for all three sample thicknesses.

It is observed that as the sample thickness increases, the spread rate of the flame in the normal spread regime decreases more rapidly. For decreasing opposed flow speeds, the flamelet regime exists for a wider range of opposed flow speeds for ¼" thick samples than for thicker samples.

CHAPTER 8

CONCLUSIONS AND FUTURE WORK

A detailed experimental and numerical analysis was conducted of the confined channel flame in which a constant volume chamber of rectangular shape was employed to examine transient premixed flame ignition, propagation, and extinction (quenching). The propagation stages produced the classical tulip flame shape, as expected. Although our research agreed in every respect with the previous literature on the subject, our numerical analysis allowed us to make observations and propose alternatives that previous research had not. Presently, we review the principal results of our research:

The ignition by a single spark produces the four-stage process described by Clanet and Searby (1996) and as shown in Figure 4.1. Once the flame propagates to the approximate geometric center of the channel and the tulip flame is formed, the propagation rate of the flame slows considerably. The absolute flame speed is a minimum when the flame front is exactly planar and the flame area is a minimum. Thereafter, the flame area increases with tulip formation as does the propagation rate, though only slightly and not proportionally with the flame area increase. Comparing the flame structure and propagation using both explicit and implicit Navier–Stokes solvers, the influence of pressure waves on the formation of the tulip flame was studied. The formation of the tulip flame, even in the absence of pressure waves, indicates that morphological change was triggered by the influence of the stagnation point phenomenon and not pressure-flame interactions. In a flame-vortex interaction, considered generally, the solution of this particular confined flame problem suggests that the factor having greatest importance for altering the flame structure and behavior is the movement of the singular points (nodes, saddles, half-nodes, half-saddles). The formation and movement of these singular points is dictated by the presence of vorticity in the channel. The

unique and compelling change caused by the formation and relative motion of these singular points, is the complete reversal of flame front behavior from decelerating finger to steady tulip (see Figure 5.3).

There are six stages of combustion. These are:

(1) Ignition, in which the ignited flame is unaware of any existing boundaries in the combustion chamber. Here the flame propagates spherically and the pressure in the channel is constant.

(2) Finger flame, in which the pressure starts to rise (see Figure 5.3); the flame, which is concave toward the burned gases, propagates toward the far side faster than it propagates toward the side walls. In this stage the rate of pressure rise dp/dt achieves a constant and high value.

(3) Transition to planar flame: This occurs toward the end of the finger flame stage. The pressure, though increasing, does so at a slower rate, thus the dp/dt curve is of distinctly smaller slope (see Figure 5.3). The flame skirts are quenching, and these same skirts are moving at high speed toward the flame front, and the stagnation point that was formed at ignition is thrust toward the flame front from the rear by the vortices formed by the quenching flame skirts. This transition stage ends when the stagnation point and the flame front, which is now exactly planar, are contiguous.

(4) Tulip flame, in which the stagnation point lodges itself in front of the propagating premixed flame, which is now cusped toward the burned gases. The velocities of the flame and stagnation point are essentially identical so that the flame/stagnation point structure moves as a coherent unit. The pressure rise rate dp/dt is still positive but diminishing toward zero with time. When $dp/dt \rightarrow 0$, this stage of combustion is complete and the flame propagation is no longer steady. (5) Flame/wall interaction, in which the pressure decreases as the tulip/stagnation point structure approaches the far wall. Heat losses to the walls are becoming apparent in this stage of combustion.

(6) Quenching, in which the flame approaches the cold far wall head on and is quenched in a complicated process involving chemistry and unsteady flow processes studied by Wichman and Bruneaux (1995) will not be discussed here.

A detailed experimental analysis was conducted on diffusion flame spread over three thicknesses of PMMA slabs (1/4", ½" and 1" thickness). Three distinct regimes are observed for the flame spread – Normal mode, Flame spread over surface, and Flamelet Regime. The dimension of the flame and the depth of solid pyrolized vary significantly over these three regimes. It is observed that the maximum heat release occurs at higher opposed flow velocities, which also correspond to lower flame spread rates. The spread rate increases as the opposed flow velocity decreases, reaching a peak when only a thin layer of the top surface pyrolyzes. Further reduction in flow velocity causes breakup of the diffusion flame to either several flamelets (in wide samples) or reduction in the width of the flamelet (in narrow samples). This flamelet burrows into the thickness of the PMMA solid until it reaches the base of the sample, whereupon it bifurcates and rejoins at the top of the surface. Future work will require the validation of the flame spread rates in the Narrow Channel Apparatus with experimental results from actual microgravity experiments. A computational model can also be developed to capture heat transfer through all three modes (conduction within the solid PMMA, convection and radiation to the surface) and accurate model of heat released by PMMA pyrolysis and subsequent combustion.

APPENDICES

APPENDIX A

Construction of Constant Volume (CV) combustor

The combustion chamber apparatus consists of three aluminum parts, the center plate and two side plates which are bolted together to form a constant volume combustion chamber. The side plates will henceforth be referred to as “plate A”, while the center plate will be referred to as “plate B”. The enclosed combustion chamber has a length of 12 inches and a square cross section with each side measuring 2 inches. The total volume of the combustion chamber is 48 cubic inches. The pressure transducers, inlet/exhaust ports and spark plugs are all mounted on plate B. The front, side and top view of the combustion chamber is shown in Figure A.1.

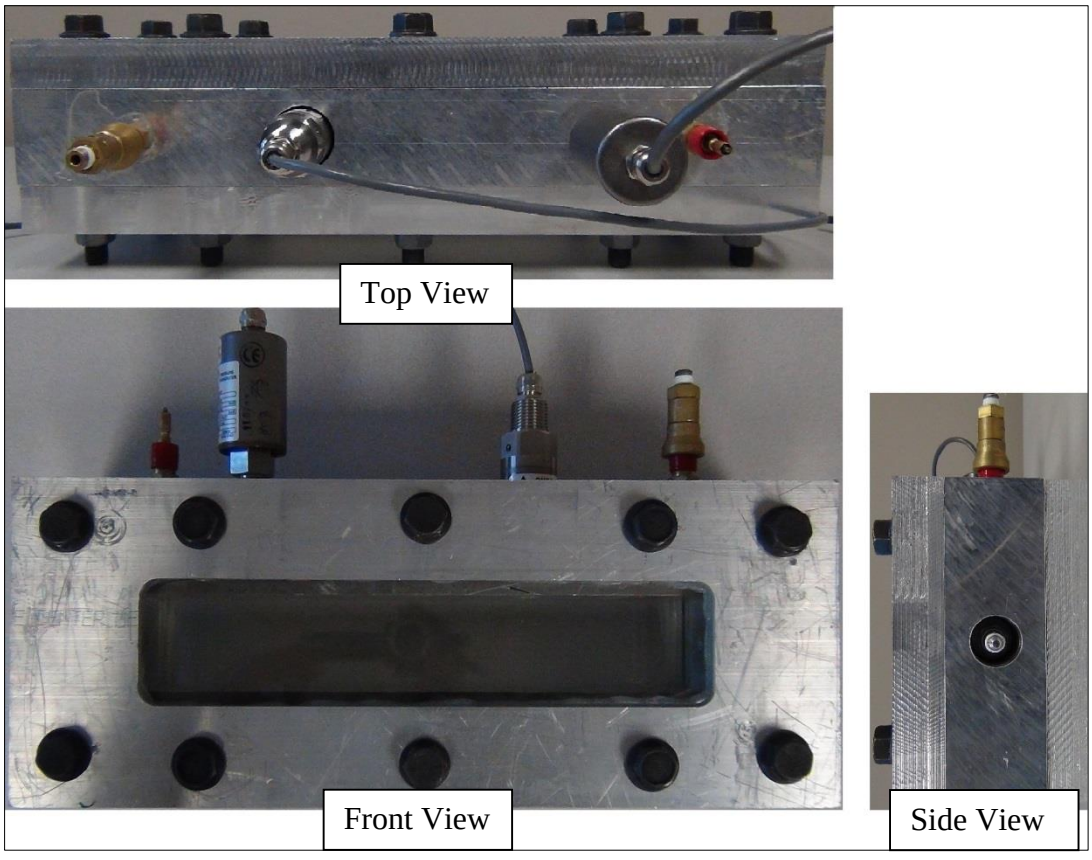

Figure A.1: Combustion chamber apparatus viewed from top, side and front of the apparatus.

A detailed description of the design and construction of the combustion chamber and diagnostic instruments will be provided below.

Plate A measures 16.5×6.5×1 inches and is machined from 6061 Aluminum metal blanks. Aluminum was chosen for its light weight, machinability and thermal conductance properties. A 12×3×0.75 inch recessed opening is machined in the geometric center of the plate. A smaller 11.5×2.5×1 inch opening is machined in the geometric center of the plate. This creates a 0.25 inch wide lip, which holds the 12×3×0.75 inch borosilicate glass slab. Borosilicate glass was chosen as the optical viewport material for its low cost and shattering resistance. When the glass slab is inserted into the recessed opening, a flush surface is created between the glass slab and the metal surface of plate A. Transparent silicone sealant (Dow Corning "700" silicone sealant) is applied along the length of the lip to attach the glass slab to the metal surface. Ten holes are machined into the plate, each measuring 0.55 inch in diameter to allow the plate to the bolted to the other two plates. A 1/16 inch thick high-temperature silicone gasket (McMaster-Carr 8525T41) is used to create an air-tight seal between the glass plate and the metal surface of plate B when sandwiched together. The orthographic front view of plate A with dimensions is shown in Figure A.2, and the rear view of the machined plate A is shown in Figure A.3. In this figure, the glass is permanently attached to the metal plate.

Plate B, which measures 16.5×6.5×2 inches, was machined from 6061 aluminum metal blanks. A 12×2×2 inch opening is machined through the geometric center of the plate. This forms the combustion chamber of the apparatus. Two spark plugs are flush mounted on either side of the 12 inch length and two pressure transducers, and inlet/exhaust ports are mounted on the top surface of plate B.

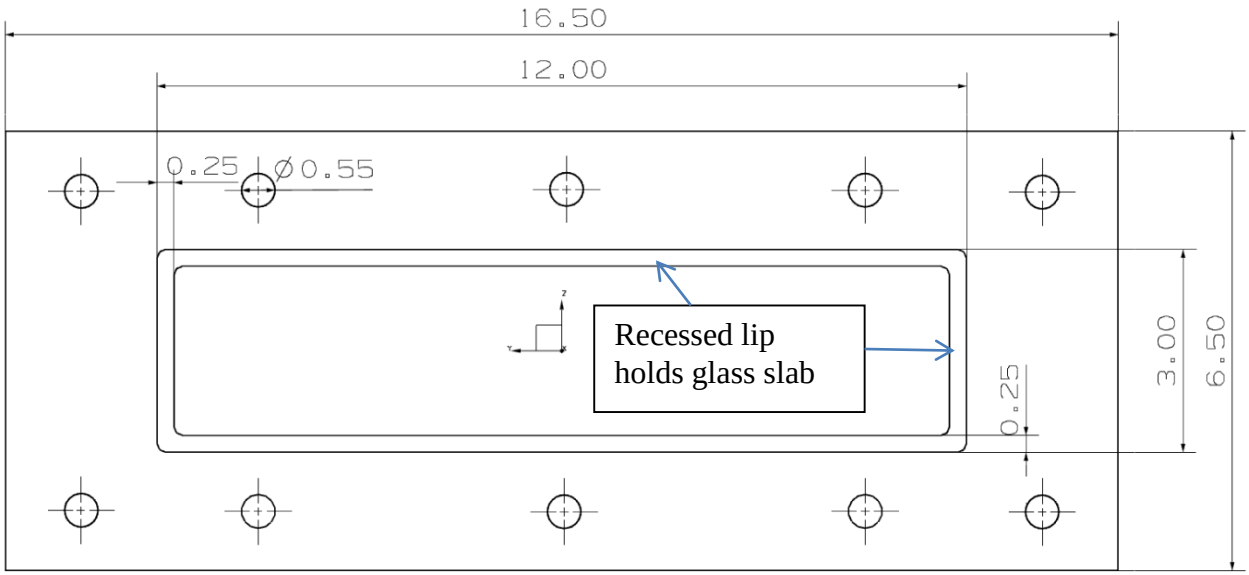

Figure A.2: Orthographic front view of plate A. The dimensions are in inches.

Figure A.3: Rear view of machined plate A with the glass slab attached to the metal place with silicone sealant.

The orthographic front view of plate B is shown in Figure A.4, and the front view of the machined plate, along with the various instruments labeled is shown in Figure A.5.

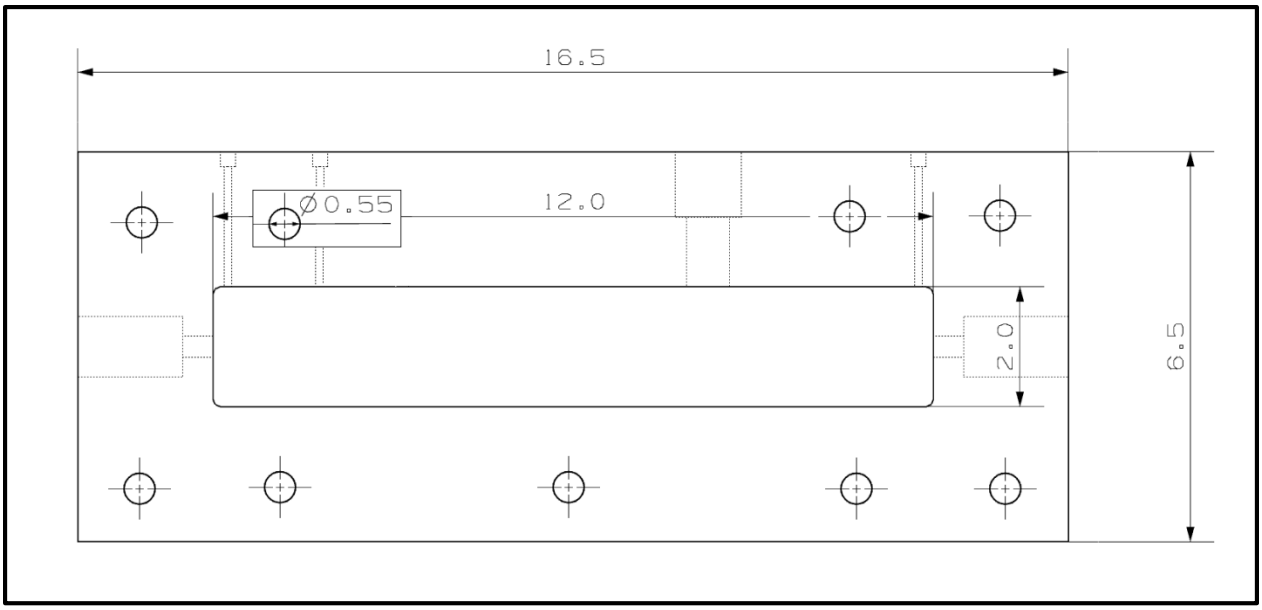

Figure A.4: Orthographic front view of plate B. The dimensions are in inches.

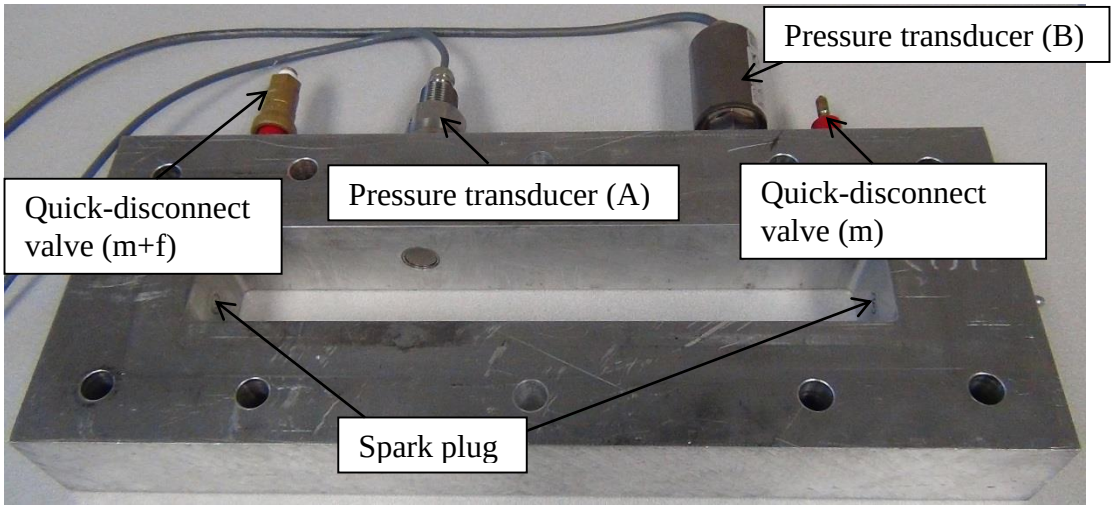

Figure A.5: Front view of the plate B, with pressure transducers, valves and spark plugs labeled.

Plate B is instrumented with two spark plugs, pressure transducers and quick-disconnect ports. Champion® 709 G54V spark plug is mounted on the metal plate B. This spark plug was chosen as it does not contain a protruding electrode and enables a flush mount with the metal surface of the combustion chamber. The Omegadyne® PX43EO-100GI flush-diaphragm pressure transducer is

mounted on plate B so that the 0.5 inch diameter diaphragm of the transducer is flush with the metal surface of the combustion chamber. This is shown in Figure A.5 and is marked as "pressure transducer A". The pressure transducer has an operational range of 0-100 psi with a 0.25 percent full-scale accuracy. The Omegadyne® PX305-300AI general purpose pressure transducer is mounted on the top surface of plate B, with a 1/8 inch diameter hole connecting it to the combustion chamber. This is shown in Figure A.5 and is marked as "pressure transducer B". The pressure transducer has an operational range of 0-300 psi with a 0.5 percent full-scale accuracy. Two Swagelok® BQC4D2PM quick-disconnect valves are mounted on the top of plate B to enable flushing the combustion chamber with air and filling gas fuel. The male coupling is attached to plate B and the female coupling is attached to the compressed air and fuel supply pipe. The quick-disconnect valves maintain a closed seal when they are disconnected and are rated for a maximum steady-state pressure of 25 bar. The two valves are labeled in Figure A.5.

The spark plugs are connected to two MSD® blaster™ ignition coils which supply 10mJ energy for every spark discharge. The two pressure transducers are connected to a National Instruments® NI-9203 data acquisition module. The ignition coils are connected to a NI-9481 digital relay module. These two modules are mounted on NI-cDAQ-9172 data controller module which is connected to the computer with a USB cable. A LabView® program is used to set the time delay between the spark firing and also to record the pressure from the transducers once the mixture is ignited. The pressure data is sampled at 10 kHz and is stored in a comma-separated-value (csv) file.

A Photron® SA6 high-speed camera is used to record the optical propagation of the flame inside the combustion chamber. The flame propagation is typically recorded at 1000, 5000 or 20,000 frames per second (fps).

To visualize the flame structure, a Schlieren apparatus was constructed using design instructions from G. S. Settles (2001). A Z-type Schlieren imaging system, with two spherical mirrors, measuring 6" in diameter and 60" focal length is used. Thorlabs® OSL-2 fiber-optic halogen lamp is used as the light-source for the Schlieren setup. The mirrors were purchased from Anchor Optics®. A generic razorblade is used as the knife-edge and a Thorlabs® P1000s pinhole is used in front of the light source. The combustion chamber is placed along path of the collimated light between the two mirrors. As the mirror diameter (6 inches) is less than the length of the combustion chamber (12 inches), only half of the combustion chamber can be visualized for each test. To record the flame structure for the entire length of its propagation, the focus area is changed for successive tests with the same unburnt initial conditions. The top-view of a typical Z-type Schlieren diagnostic setup is shown in Figure A.6.

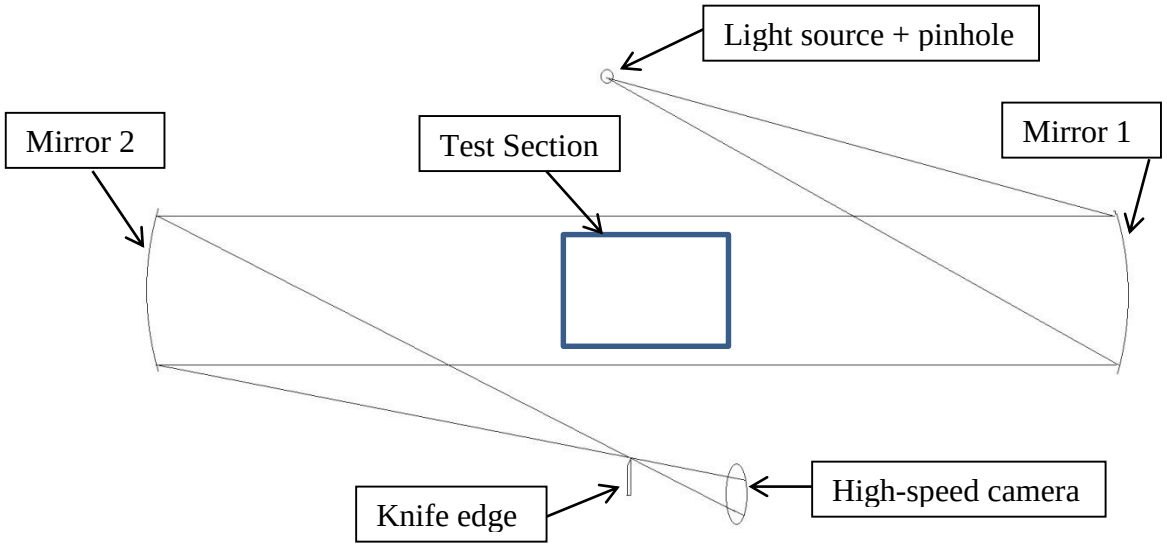

Figure A.6: Schematic top-view of a Z-type Schlieren setup (Settles, 2001).

The apparatus is constructed by sandwiching plate B with two pieces of plate A, and held together with ten 0.5 inch diameter bolts. The silicone gasket between the three plates creates an airtight

chamber measuring 12x2x2 inches, which is the enclosed combustion chamber. After each disassembly/assembly cycle, the combustion chamber is pressurized to 60 psi with compressed air and tested for leakage by monitoring the pressure drop and by using Swagelok® Snoop™ liquid leak detector. Typical causes for leaks include non-uniform tightening of the nuts and bolts, which can be prevented by using a torque-wrench.

APPENDIX B

Computational Fluid Dynamics (CFD) simulation setup

The numerical schemes described below have been implemented with the commercial CFD software, Ansys Fluent®. Additional user defined function (UDF) scripts were utilized to modify the default options. Numerical simulations of the flame propagation were performed for both two-dimensional (2D) and three-dimensional (3D) geometries.

The 2D simulations were performed with mesh cell size of 1/128 cm whose results were compared with mesh cell sizes of 1/64 cm and 1/256 cm for grid independence. The simulations were performed with 1-step methane-air chemistry and the 30 species, 184 step reaction mechanism by Lu and Law (2008) for validation. The 3D simulations were performed with mesh cell size of 1/40 cm whose results were compared with mesh cell sizes of 1/20 cm and 1/80 cm for grid independence. The 3D simulations were performed with 1-step methane-air chemistry with the thickened flame model, first described by Butler and O'Rourke (1977). A detailed description of both 2D and 3D simulation model and the computational mesh is described below.

COMPUTATIONAL GEOMETRY AND MESH GENERATION

The computational geometry consists of a rectangular domain (for 2-D simulations) measuring 304.8×50.8 mm, which forms the combustion chamber with an aspect ratio (L/D_h) = 6. For the case of a 3-D simulation, a cuboidal domain measuring 304.8×50.8×50.8 mm is used. The computational geometry uses a simplified representation of the experimental setup. The 3.175 mm diameter fillet along the four edges of the apparatus and three 5 mm diameter holes which connect the inlet/exhaust valves and pressure transducer to the combustion chamber are not modeled in the computational grid. A schematic diagram of the 2D domain is shown in Figure B.1.

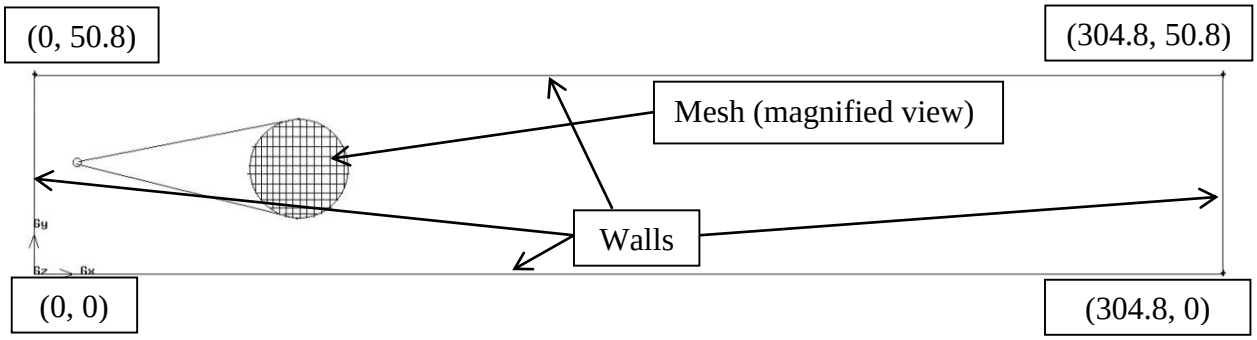

Figure B.1: Schematic diagram of the computational domain. Dimension in mm.

For the 2-D simulation, mesh generation was performed using structured quadrilateral cells with four nodes per cell. The cell side measured 1/128 cm, and cell sizes of 1/64 cm and 1/256 cm were used to evaluate mesh independence. For the 3-D simulation, mesh generation was performed using structured hexahedral cells with eight nodes per cell. The cell side measured 1/40 cm, and cell sizes of 1/20 and 1/80 cm were used to evaluate mesh independence.

The total number of cells was approximately 2.53 million for the 2-D simulation with 1/128 cm quadrilateral cell size and approximately 50.25 million for the 3-D simulation with 1/40 cm hexahedral cell size.

COMPUTATIONAL FLUID DYNAMICS SETUP

The computational fluid dynamics simulation for the two dimensional domain is performed by writing the Navier-Stokes equations in integral Cartesian form for an arbitrary control volume *V* with differential surface area *dA* as follows:

$$\frac{\partial}{\partial t}\iiint_V \rho dV + \iint_{dA} \rho V.dA = 0 \qquad B.1$$

$$\frac{\partial}{\partial t}\iiint_V \rho u dV + \iint_{dA} (\rho u V + P\hat{\imath} - \tau_{xi}).dA = 0 \qquad B.2$$

$$\frac{\partial}{\partial t}\iiint_V \rho v dV + \iint_{dA} (\rho v V + P\hat{\jmath} - \tau_{yi}).dA = 0 \qquad B.3$$

$$\frac{\partial}{\partial t}\iiint_V \rho w dV + \iint_{dA} (\rho w V + P\hat{k} - \tau_{zi}).dA = 0 \qquad B.4$$

$$\frac{\partial}{\partial t}\iiint_V \rho E dV + \iint_{dA} (\rho E V + PV - (\tau_{ij}V_j + q)).dA = 0 \qquad B.5$$

$$\frac{\partial}{\partial t}\iiint_V \rho Y_m dV + \iint_{dA} (\rho V Y_m + J_m).dA = R_m \qquad B.6$$

Equation B.1 is the integral form of the continuity equation, Eqs. B.2, B.3 and B.4 are the momentum equations, Eq. B.5 is the energy equation and Eq. B.6 is the transport equation of species "*m*". In the above equations, ρ is the density of the fluid; *V* is the velocity vector with components *u*, *v* and *w* in the Cartesian coordinate system; P is the pressure inside the control volume; Y_m represents the mass fraction of species "m" in the control volume. The total energy E, viscous stress tensor τ, species diffusion flux J_m and thermal conduction q are described in the Eqs. B.7, B.8, B.9 and B.10 respectively.

$$E = h + \frac{V^2}{2} - \frac{P}{\rho} \qquad B.7$$

$$\tau_{xx} = -\frac{2}{3}\mu(\nabla.V) + 2\mu\frac{\partial u}{\partial x} \qquad B.8a$$

$$\tau_{yy} = -\frac{2}{3}\mu(\nabla.V) + 2\mu\frac{\partial v}{\partial y} \qquad B.8b$$

$$\tau_{zz} = -\frac{2}{3}\mu(\nabla.V) + 2\mu\frac{\partial w}{\partial z} \qquad B.8c$$

$$\tau_{xy} = \tau_{yx} = \mu\left[\frac{\partial v}{\partial x} + \frac{\partial u}{\partial y}\right] \qquad B.8d$$

$$\tau_{xz} = \tau_{zx} = \mu\left[\frac{\partial u}{\partial z} + \frac{\partial w}{\partial x}\right] \qquad B.8e$$

$$\tau_{yz} = \tau_{zy} = \mu\left[\frac{\partial w}{\partial y} + \frac{\partial v}{\partial z}\right] \qquad B.8f$$

$$J_m = -\rho D_{m,a}\nabla Y_m - D_{T,m}\frac{\nabla T}{T} \qquad B.9$$

$$q = -k\nabla T \qquad B.10$$

Here, μ refers to the molecular viscosity coefficient, $D_{m,a}$ is the mass diffusion coefficient of species "m" in the gas mixture "a", $D_{T,m}$ is the thermal diffusion coefficient and k is the thermal conductivity. The simulation specific values of viscosity, diffusion coefficients, and thermal conductivity are listed in pages 122 and 123. In Eq. B.6, R_m is the net rate of production of species m, described in Eq. B.11.

$$R_m = MW_m\sum_{r=1}^{N}\hat{R}_{m,r} \qquad B.11$$

Here, MW_m is the molecular weight of species m, and $R_{m,r}$ is described in equation B.12 below.

$$\hat{R}_{m,r} = \left(\upsilon''_{m,r} - \upsilon'_{m,r}\right)\left(k_{f,r}\prod_{j=1}^{N}\left[C_{j,r}\right]^{\left(\eta'_{j,r}+\eta''_{j,r}\right)}\right) \qquad B.12$$

Here, $\nu'_{m,r}$ and $\nu''_{m,r}$ are the stoichiometric coefficients of reactant and product m in reaction *r* respectively, and $k_{f,r}$ is the forward rate constant of reaction *r*. In addition, $C_{j,r}$ is the molar

concentration of species *j* is reaction r, and $\eta'_{j,r}$ and $\eta''_{j,r}$ are the rate exponents of reactant and product species *j* in reaction *r*, respectively.

The forward rate constant, $k_{f,r}$ is written in Eq. B.13 below.

$$k_{f,r} = A_r T^{\beta} e^{\frac{-E_r}{RT}} \qquad B.13$$

Here, Ar is the pre-exponential factor, β is the temperature exponent, Er is the activation energy and R is the universal gas constant. The numerical values of the above quantities are listed on page 123.

The iterative SIMPLE (Semi-Implicit Method for Pressure Linked Equations) algorithm is used to solve the Navier-Stokes Eqs. B.1-6. The ideal gas relation, given in Eq. B.14, is used as an additional equation for the solver.

$$p = \rho RT \qquad B.14$$

A detailed description of the algorithm is given in Patankar and Spalding (1972) and Patankar (1980).

In Eq. B.14, p is the pressure, ρ is the density, T is the temperature and R is the gas constant (8.314 J/mol.K).

For the two-dimensional simulation case, the mesh size of 1/128 cm resolves the flame front (as demonstrated through tests of mesh independence) and the reaction zone is contained in about 12 cells. For the three-dimensional simulation case, the mesh size of 1/40 cm is insufficient to resolve the flame front and artificial thickening, illustrated by Butler and O'Rourke (1977) is used. A short description of the procedure is given below.

For a premixed flame, the laminar flame speed, U_l, is proportional to the root of the product DR, were D is the thermal diffusivity (L^2/t) and R is the reaction rate (t^{-1}). The laminar flame thickness is proportional to D/U_l. To thicken the laminar flame, the diffusivity can be increased along with

a corresponding reduction in the chemical reactivity. This ensures the laminar flame speed remains unchanged. The thickening factor F is calculated in Eq. B.15.

$$F = \frac{N\Delta}{\delta} \qquad B.15$$

Here, Δ is the grid cell size, δ is the laminar flame thickness and N is the number of points in the flame front to be resolved (set as 4). The grid size, Δ, is the cube root of the cell volume, and the laminar flame thickness, δ, is defined as D/U_l, where D is the thermal diffusivity evaluated as $k/\rho C_p$. Here k is the thermal conductivity, and C_p is the specific heat of the gas mixture.

In a narrow region around the reaction zone, the species diffusion coefficients, and the thermal conductivity, are multiplied by the thickening factor F while the reaction rate is divided by F. This step is performed by multiplying F with a factor Ω, which is calculated as shown in Eq. B.16 below:

$$\Omega = \tanh\left(\frac{\beta * \overline{|R|}}{\max(\overline{|R|})}\right) \qquad B.16$$

Here, R is the spatially filtered absolute value of the reaction rate, and β is set as 10. The value of Ω is unity in a narrow region around the flame front, and zero everywhere else. The width of this band can be changed by changing the value of β.

The spatial discretization of the different scalars is performed using the second order upwind scheme, described in detail by Barth and Jespersen (1989). The temporal discretization is performed using first-order backward differences, shown for a variable φ below:

$$\varphi^{n+1} = \varphi^n + \Delta t.F(\varphi^{n+1}) \qquad B.17$$

Here, F(φ) is the time derivative of the variable φ, and Δt is the time step size, chosen so that the Courant-Friedrichs-Lewy (CFL) condition is satisfied and remains 0.5. The CFL number is defined as

$$C = \Delta t \sum_{i=1}^{n} \frac{u_{x_i}}{\Delta x_i} \qquad B.18$$

where, C is the CFL number, u_{xi} is the local speed of sound "c", defined in Eq. B.19, and Δx_i is the cell size. The quantity "n" is the number of dimensions of the simulation mesh.

$$c = \sqrt{\gamma RT} \qquad B.19$$

Here, the quantity γ is the ratio of specific heats (C_p/C_v), R is the universal gas constant (8.314 J/mol.K) and T is the local temperature.

PROPERTIES OF GAS MIXTURES

The unburnt and burnt gas inside the combustion chamber is composed of the following five species – methane, oxygen, nitrogen, carbon dioxide and water vapor. Water remains in the vapor phase throughout the simulation: for simplicity, phase change is not modeled. The various temperature and pressure dependent properties of the gas mixture are given below.

SPECIFIC HEAT

The specific heat of the gaseous mixture is calculated as the mass fraction average of the pure species specific heat capacities,

$$c_p = \sum_i Y_i c_{p,i} \qquad B.20$$

Here, c_p is the specific heat of the mixture, $c_{p,i}$ is the specific heat of species i and Y_i is the mass fraction of species i.

The specific heat of individual species, $c_{p,i}$, is computed using a piecewise polynomial with temperature range from 300K to 5000K using the coefficients from GRI-Mech 3.0 database by Smith et.al. (2000). The input is supplied in the NASA thermodynamic file format, specified by Burcat and McBride (1993).

THERMAL CONDUCTIVITY AND VISCOSITY

The thermal conductivity and viscosity of the mixture is calculated using the following relation,

$$k = \sum_i \frac{X_i k_i}{\sum_j X_j \phi_{ij}} \quad , \quad \mu = \sum_i \frac{X_i \mu_i}{\sum_j X_j \phi_{ij}} \qquad B.21$$

Here, k is the thermal conductivity, μ is the viscosity, X_i is the mole fraction of species i and φ is described in the equation below:

$$\phi_{ij} = \frac{\left[1 + \left(\frac{\mu_i}{\mu_j}\right)^{1/2} \left(\frac{MW_j}{MW_i}\right)^{1/4}\right]^2}{\left[8\left(1 + \frac{MW_i}{MW_j}\right)\right]^{1/2}} \qquad B.22$$

Here, MW_i is the molecular weight of the species i.

The thermal conductivity of individual species, k_i is calculated using

$$k_i = \frac{15}{4}\frac{R}{MW_i}\mu_i\left[\frac{4}{15}\frac{c_{p.i}MW_i}{R} + \frac{1}{3}\right] \qquad B.23$$

Here, μ_i is the viscosity of species i, using Sutherland's viscosity law, which is described by

$$\mu_i = \mu_0 \left(\frac{T}{T_0}\right)^{3/2} \frac{T_0 + S}{T + S} \qquad B.24$$

Here, T_0, μ_o and S are reference temperature, viscosity and effective temperature respectively. The values of these parameters for the different species are given in Table B.1.

	Reference Viscosity (kg/m.s)	Reference Temperature (K)	Effective Temperature (k)
Methane	1.824e-05	273.11	143.5
Oxygen	1.919e-05	273.11	138.9
Nitrogen	1.663e-05	273.11	106.67
Carbon dioxide	1.37e-05	273.11	222.22
Water Vapor	1.703e-05	416.67	861.11

Table B.1: Parameters for Sutherland's viscosity law, Eq. B.24.

THERMAL DIFFUSIVITY

The thermal diffusivity coefficient for species i is calculated using

$$D_{T,i} = -2.59\text{x}10^{-7} T^{0.659} \left[\frac{MW_i^{0.511} X_i}{\sum_{i=1}^{N} MW_i^{0.511} X_i} - Y_i \right] . \left[\frac{\sum_{i=1}^{N} MW_i^{0.511} X_i}{\sum_{i=1}^{N} MW_i^{0.489} X_i} \right] \qquad B.25$$

REACTION RATE PARAMETERS

The numerical simulation is performed with both a 1-step methane-air chemical reaction and using the GRI-Mech 3.0 detailed chemical mechanism, consisting of 53 species and 325 reaction steps. The single step reaction chemistry is represented by

$$CH_4 + 2O_2 \rightarrow CO_2 + 2H_2O \qquad B.26$$

The parameters to be used in equations B.12 and B.13 are given below in Tables B.2 and B.3.

	η	ν
Methane	1	0.2
Oxygen	2	1.3
Carbon dioxide	1	0
Water vapor	2	0

Table B.2: Stoichiometric coefficients and rate exponents of 1-step reaction.

A	2.119e+11
E_a (j/kg-mol)	2.027e+08
β	0

Table B.3: Reaction rate parameters for 1-step reaction.

The reaction parameters for the GRI-Mech 3.0 detailed mechanism can be obtained from the database of Smith et. al. (2000).

BOUNDARY CONDITIONS

The computational domain is enclosed, or surrounded, by either four (2-D domain) or six (3-D domain) wall boundary conditions. In the experimental apparatus, four of the walls (square cross section walls and two lateral walls) are built of aluminum and the other two walls are made of the glass viewport. In the numerical simulation results, the temperature of all the wall boundaries has been set to a constant 300K. Additional simulations were performed for a conjugate heat transfer simulation, with the solid aluminum block exposed to both the combustion chamber and the outside air.

COMPARISON OF WALL BOUNDARY CONDITIONS

For the simulation Case I, the walls of the computational domain are at a constant temperature of T = 300K. For simulation Case II, the solid plate of aluminum surrounding the combustion chamber is also included in the numerical simulation and a conjugate heat transfer simulation is performed. Both the simulation cases are performed on a 2-D domain, for simplicity. The outer wall of the conjugate heat transfer simulation is set as a convective wall, with a heat transfer coefficient of h=10 W/m^{2}K, as suggested by Jacob (1958), and a free stream temperature of 300K. The computational domain of simulation Case II is shown in Figure B.2.

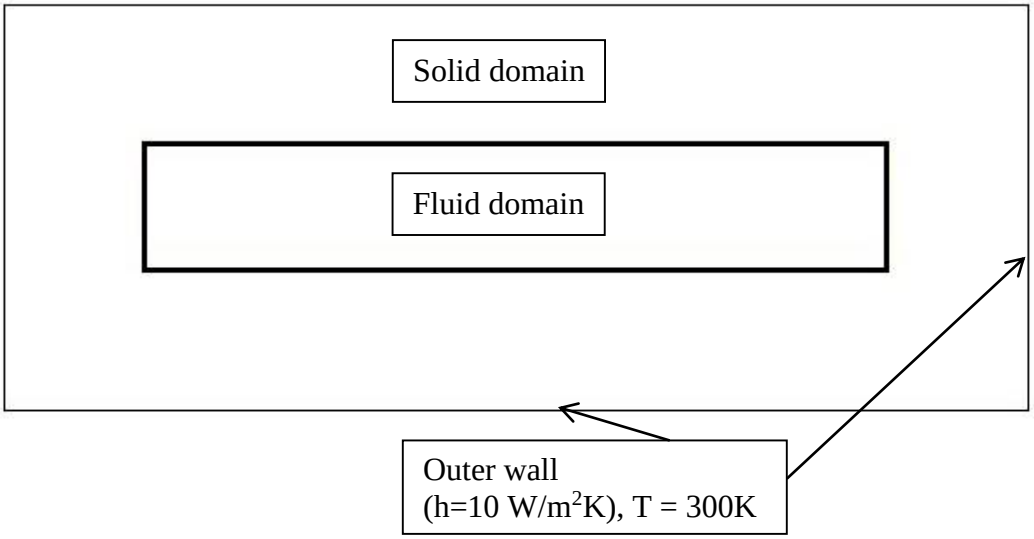

Figure B.2: Computational domain of simulation Case II.

The parameters compared between the two simulations are the average static pressure inside the fluid domain and the total heat transfer rate between the fluid and the solid wall.

The quantities are plotted against normalized time. The average pressure inside the combustion chamber for the two cases, along with the difference in the pressure between the two cases is shown

in Figure B.3. The pressure difference is calculated by subtracting the pressure from Case I (constant T) with pressure from Case II (conjugate BC).

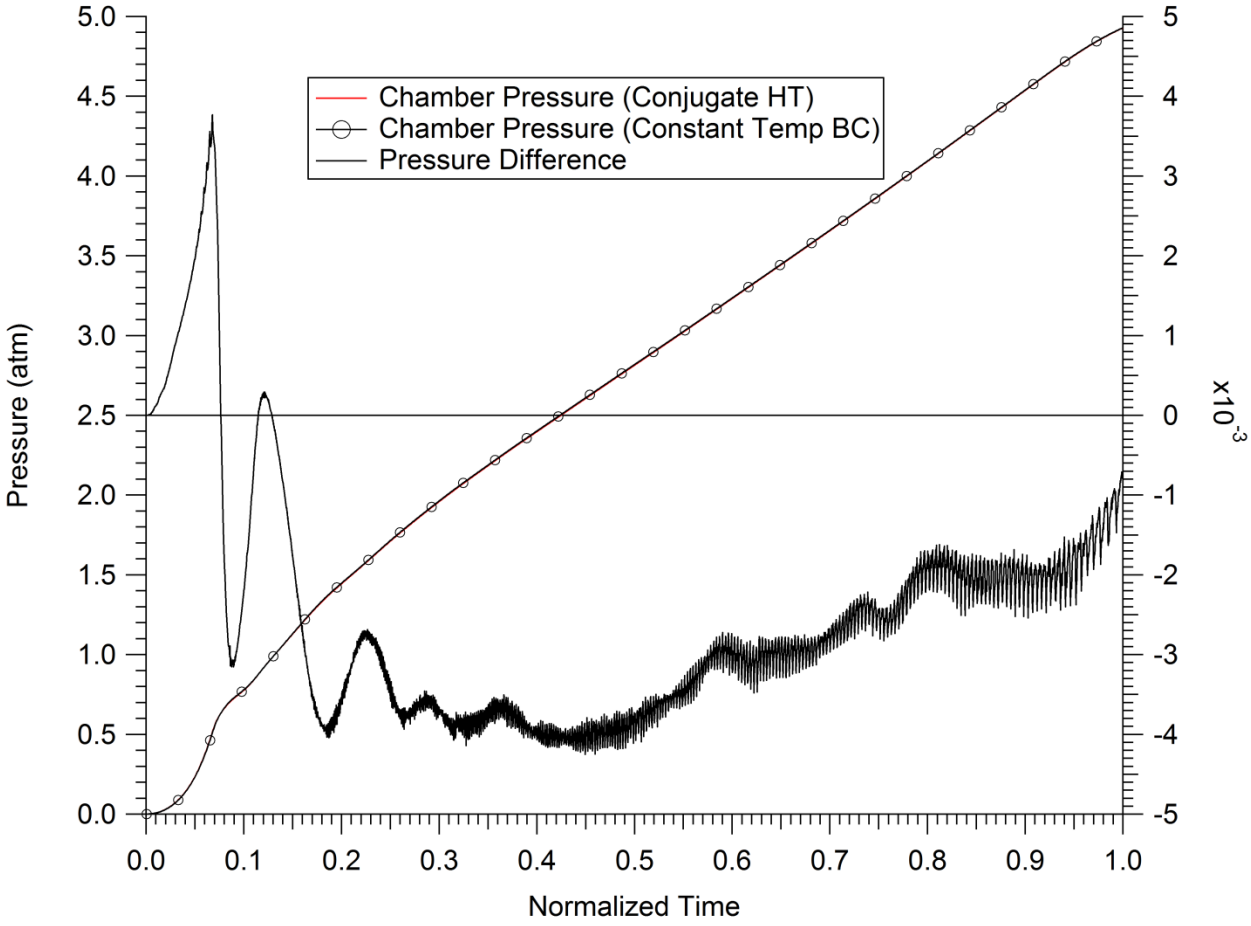

Figure B.3: Comparison of average chamber pressure between constant temperature and conjugate heat transfer boundary conditions.

From the Figure B.3, we observe that the maximum difference in the average pressure in the control volume between the two cases is only 0.004 atm, which is less than 0.1% of the maximum pressure in the combustion chamber.

To obtain further clarity, the heat transfer from the combustion chamber to the cold walls is shown in Figure B.4. The figure shows the heat flux to the wall for cases I & II, and also the difference in the heat transfer rate between the two cases.

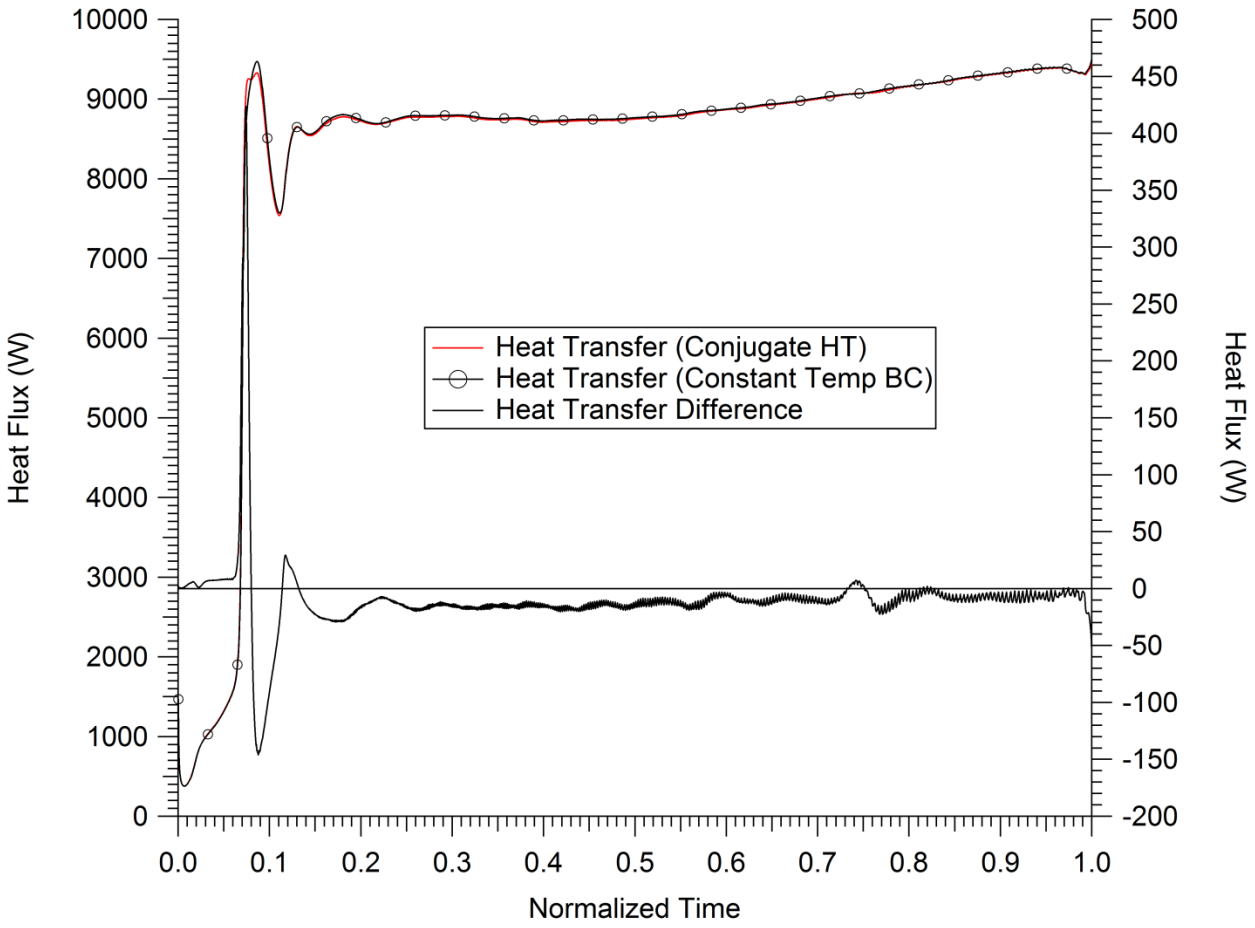

Figure B.4: Comparison of heat transfer rate to the cold walls for conjugate heat transfer and constant temperature wall boundary cases.

From the above figure, we observe that the difference in the heat flux to the cold wall between conjugate heat transfer case and the constant wall temperature case is 15W on average, which is 0.15% of the total heat flux to the cold wall. This proves that the constant temperature wall boundary (set to 300K) can be used in all simulations for computational simplicity while maintaining physical accuracy.

MESH INDEPENDENCE STUDY

The simulation for mesh independence is performed for varying levels of mesh refinement. The quadrilateral mesh for the two dimensional domain has three levels of mesh refinement - 1/64, 1/128 and 1/256 cm. The normalized heat release rate (HRR) is compared for the three simulations to determine mesh independence. The heat release rate for each case is normalized by dividing it with the maximum heat release rate for the coarse mesh (1/64 cm).

For the two dimensional simulation, the total heat release rate as a function of time for the three mesh sizes is shown in Figure B.5.

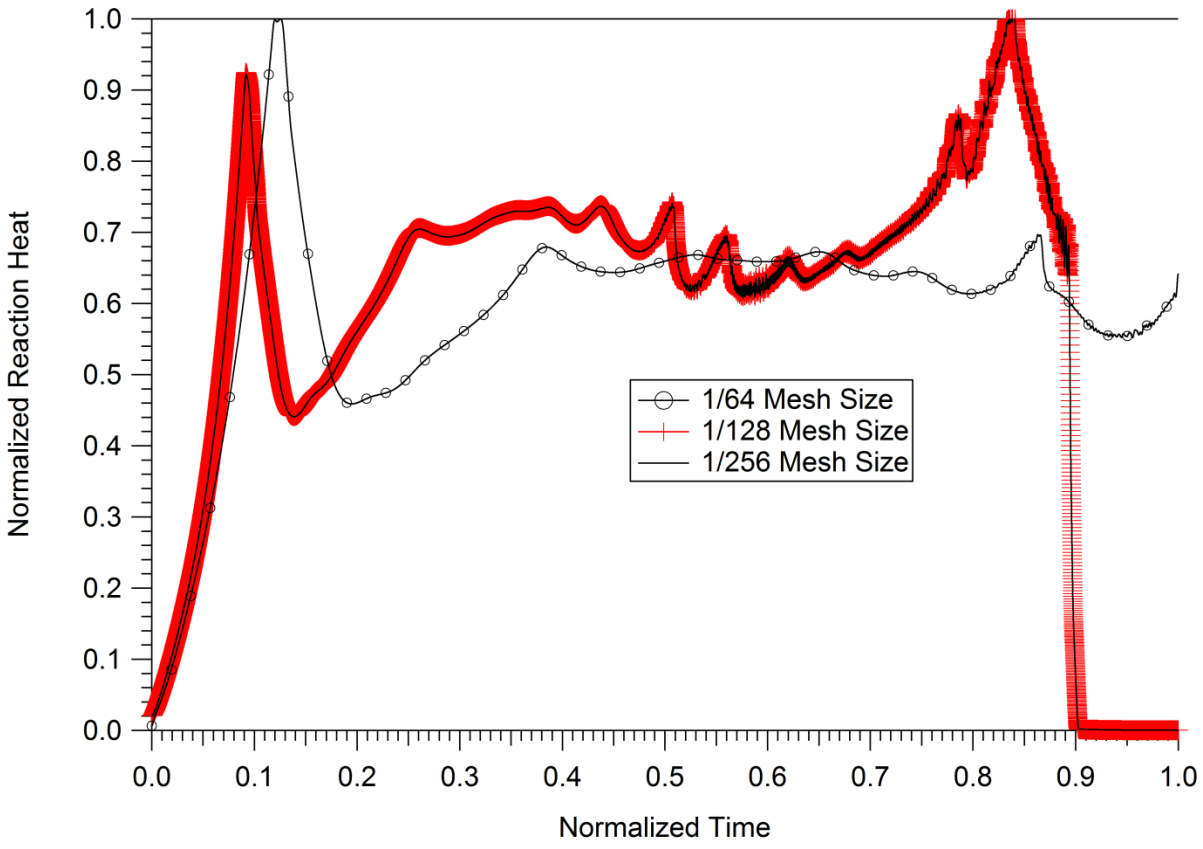

Figure B.5: Comparison of normalized reaction heat release for three levels of mesh refinement (1/64, 1/128 and 1/256 cm).

It is observed that the difference between the heat release rate for 1/128 cm and 1/256 cm mesh size is less than 2% of the heat release value, whereas, for the 1/64 cm mesh size, the difference in the heat release is greater than 10%. In order to reduce the total time taken for simulation and increase the computational speed, the mesh size of 1/128 cm (for 2-D simulations) and 1/40 cm (for 3-D simulations) is used in all subsequent simulations.

APPENDIX C

PROGRAM CODES

Program 1 – Premixed flame front tracking (flame_track.m)

```
%%%%%%%%%%%%%%%%%%%%%%%%%%%%%%%%%%%%%%%%%%%%%%%%%%%%%%%%%%%%%%%%%%%%%%%%%%%%
%                                Flame Tracking Code v1.2                                %
%                                                                                        %
%                                Created by Ashwin Hariharan                             %
%                                Email - ashwin.hariharan@gmail.com                      %
%                                                                                        %
%                Contact Author to use/modify source code and program                    %
%                                                                                        %
%%%%%%%%%%%%%%%%%%%%%%%%%%%%%%%%%%%%%%%%%%%%%%%%%%%%%%%%%%%%%%%%%%%%%%%%%%%%

clc
clear all

%% Specify Image Folder

filedir=uigetdir('','Select image folder');
oldfolder=cd(filedir);
imagelist=[ls('*.tif') ls('*.bmp') ls('*.jpg')];
numimages=length(imagelist);

%% Initial Parameters

left2right=0;
right2left=1;
tubefocuswidth=4;                          % Focus Width of Camera in cm
tubefocuslength=28;                        % Focus Area of the Camera in cm
framerate=20000;                           % Image Capture Rate in FPS
rawimage=imread(imagelist(1,:));
[d1,d2]=size(rawimage);
time=zeros(numimages,1);
binconvert=zeros(d1,d2);
flamepos=zeros(d1,numimages);
avflamepos=zeros(1,numimages);
centerflamepos=zeros(1,numimages);
flamediv=round(d1/3);
upperlobeflame=zeros(1,numimages);
lowerlobeflame=zeros(1,numimages);
userinput=75;
userflame=zeros(1,numimages);
```

```
%% Image Conversion

for imagenumber=1:numimages
rawimage=imread(imagelist(imagenumber,:));
[d1,d2]=size(rawimage);
maxint=max(max(rawimage));
minint=min(min(rawimage));
thresh=(maxint-minint)/24;
for i=1:d1
   for j=1:d2
      if rawimage(i,j)>thresh
         binconvert(i,j)=1;
      else
         binconvert(i,j)=0;
      end
   end
end
dispimage=255*binconvert;
image(dispimage)
colormap gray
axis image
M(imagenumber)=getframe;

if right2left == 1
   binconvert=flipdim(binconvert,2);
end
for i=1:d1
   for j=d2:-1:1
     if binconvert(i,j)==1
         flamepos(i,imagenumber)=(j);
         break
      end
   end
end
end

%% Flame Position Calculation
% Average Flame Position

for i=1:numimages
   avflamepos(1,i)=(sum(flamepos(:,i))/nnz(flamepos(:,i)));
end
% Centerline Flame Position

for i=1:numimages
```

```
   centerflamepos(1,i)=flamepos((d1/2),i);
end

% Lower and Upper Lobe Flame Position

for i=1:numimages
   lowerlobeflame(1,i)=flamepos((flamediv),i);
   upperlobeflame(1,i)=flamepos((2*flamediv),i);
end

% User Input Flame Position

for i=1:numimages
   userflame(1,i)=flamepos(userinput,i);
end

% Flipping position matrix

avflamepos=avflamepos';
centerflamepos=centerflamepos';
lowerlobeflame=lowerlobeflame';
upperlobeflame=upperlobeflame';
userflame=userflame';

% Computing deviation from center flame

deviation1=avflamepos-centerflamepos;
deviation2=lowerlobeflame-centerflamepos;
deviation3=upperlobeflame-centerflamepos;
deviation4=userflame-centerflamepos;

% converting from pixel to cm

mulfac=tubefocuslength/d2;
avflamepos=avflamepos*mulfac;
centerflamepos=centerflamepos*mulfac;
lowerlobeflame=lowerlobeflame*mulfac;
upperlobeflame=upperlobeflame*mulfac;
userflame=userflame*mulfac;
deviation1=deviation1*mulfac;
deviation2=deviation2*mulfac;
deviation3=deviation3*mulfac;
deviation4=deviation4*mulfac;

%% Flame Speed Calculations
```

```
avflamespeed = diff(avflamepos)*framerate;
centerflamespeed = diff(centerflamepos)*framerate;
lowerlobeflamespeed = diff(lowerlobeflame)*framerate;
upperlobeflamespeed = diff(upperlobeflame)*framerate;
userflamespeed = diff(userflame)*framerate;

%% Flame Surface Area Calculation

flamearea=diff(flamepos);
flamearea=flamearea*mulfac;
flamearea=flamearea.*flamearea;
flamearea=flamearea+(1/tubefocuswidth);
flamearea=sqrt(flamearea);
for i=1:(d1-1)
   for j=1:numimages
      if flamearea(i,j)==(2/tubefocuswidth)
         flamearea(i,j)=0;
      end
   end
end
totalflamearea=sum(flamearea);
totalflamearea=totalflamearea';

clear d1 d2 binconvert dispimage filedir flamearea flamedir flamepos framerate i imagenumber j
left2right right2left maxint minint numimages oldfolder rawimage thresh time tubefocuslength
tubefocuswidth flamediv mulfac

%% Writing Output to MS Excel files

heading1 = {'Average Flame Speed','Center Flame Speed','Lower Lobe Flame Speed', 'Upper Lobe
Flame Speed','User Flame Speed'};
datawrite=[avflamespeed,centerflamespeed,lowerlobeflamespeed,upperlobeflamespeed,userflam
espeed];
xlswrite('flamespeed.xls',datawrite);
heading2 = {'Average Flame Position', 'Center Flame Position', 'Lower Lobe Flame Position',
'Upper Lobe Flame Position', 'User Flame Position', 'Average Deviation', 'Lower Lobe Deviation',
'Upper Lobe Deviation', 'User Flame Deviation', 'Flame Area'};
datawrite=[avflamepos,centerflamepos,lowerlobeflame,upperlobeflame,userflame,deviation1,dev
iation2,deviation3,deviation4,totalflamearea];
xlswrite('flamepos.xls',datawrite);
xlswrite('flamespeedheading.xls', heading1);
xlswrite('flameposheading.xls',heading2);
```

BIBLIOGRAPHY

BIBLIOGRAPHY

Barth, T. J. and Jespersen, D. (1989). The design and application of upwind schemes on unstructured meshes. Technical Report AIAA-89-0366. AIAA 27th Aerospace Sciences Meeting, Reno, Nevada.

Butler, T. D. and O'Rourke, P. J. (1977). A numerical method for two dimensional unsteady reacting flows. Symposium (International) on Combustion. **16**, 1503-1515.

Burcat, A. and McBride, B. (1993). Ideal Gas Thermodynamic Data for Combustion and Air Pollution Use. Technion Report TAE 697.

Clanet, C., and Searby, C. (1996). On the "tulip flame" phenomenon. Combustion and Flame, **105**, 225.

Clavin, P. (1985). Dynamic behavior of premixed flame fronts in laminar and turbulent flows. Progress in Energy and Combustion Science. **11**, 1-59.

DeRis, J. N. (1969). "Spread of a Laminar Diffusion Flame" Twelfth Symposium (International) on Combustion, The Combustion Institute, pp. 241-252.

Dold, J.W., and Joulin, G. (1995). An evolution equation modeling inversion of tulip flames. Combustion and Flame, **100**, 450.

Dunn-Rankin, D., and Sawyer, R.F. (1985). Interaction of a laminar flame with its self-generated flow during constant volume combustion. Presented at the 10th International Colloquium on the Dynamics of Explosions and Reactive Systems (ICDERS), Berkeley, CA, August 4–9, pp. 115–118.

Dunn-Rankin, D., Barr, P.K., and Sawyer, R.F. (1988). Numerical and experimental study of "tulip" flame formation in a closed vessel. Symp. (Int.) Combust., **21**, 1291.

Ellis, O. (1928). Flame movement in gaseous explosive mixtures: some general ideas. Fuel Science in Practice. 7, 502.

Fernandez-Pello, A. C., and F. A. Williams. (1975). "Laminar Flame Spread over PMMA Surfaces." Fifteenth Symposium (International) on Combustion, The Combustion Institute, pp. 217-231.

Fernandez-Pello, A. C., and F. A. Williams. (1977). "A Theory of Laminar Flame Spread over Flat Surfaces of Solid Combustibles." Combustion and Flame, **28**, pp. 251-277.

Foss, J. (2004). Surface selections and topological constraint evaluations for flow field analyses. Exp. Fluids, **37**, 883–898.

Gaydon, A. G. and Wolfhard, H. G. (1979). Flames, their structure, radiation and temperature. Chapman and Hall, London.

Glassman, I. and Yetter, R. A. (2007). Combustion. Academic Press, Waltham, PA.

Gonzales, M., Borghi, R., and Saouab, A. (1992). Interaction of a flame front with its self-generated flow in an enclosure: The "tulip flame" phenomenon. Combustion and Flame, **88**, 201–220.

Guenoche, H. (1964). Nonsteady Flame Propagation, Pergamon Press, New York, pp. 107–126.

Hariharan, A., and Wichman, I. S. (2014). Premixed flame propagation and morphology in a constant volume combustion chamber. Combust. Sci. Technol., **186**, 1025–1040.

Hirschfelder, J. O., Curtiss, C. F. and Bird, R. B. (1954). The molecular theory of gasses and liquids. Wiley Publishing, New York.

Iancu, F., Piechna, J. R., and Mueller, N. (2008). Basic design scheme for wave rotors. Shock Waves. **18**, 356-378.

Jacob, M. (1958). Heat Transfer. John Wiley and sons, New York.

Kaltayev, A.K., and Reidel, U.R. (2000). The hydrodynamic structure of a methane-air tulip flame. Combustion Science and Technology, **158**, 53–69.

Law, C. K. (2006). Combustion Physics. Cambridge University Press, New York.

Linan, A. and Williams, F. A. (1994). Fundamental Aspects of Combustion. Oxford University Press, Oxford.

Lu, T. F. and Law, C. K. (2008). A criterion based on computational singular perturbation for the identification of quasi steady state species: A reduced mechanism for methane oxidation with NO chemistry. Combustion and Flame. **154**, 761-774.

Mallard, E. and LeChatelier, H. L. (1883). Combustion of explosive gas mixtures. Ann. Mines. **4**, 274-618.

Marra, F.S., and Continillo, G. (1996). Numerical study of premixed laminar flame propagation in a closed tube with a full Navier-Stokes approach. Symp. (Int.) Combust., **26**, 907–913.

Metzener, P., and Matalon, M. (1997). The propagation of premixed flames in closed tubes. Journal of Fluid Mechanics, **336**, 331–350.

McGreevy, J.L. (1993). Premixed flame propagation in closed tubes. PhD thesis. Northwestern University, Evanston, IL.

McGreevy, J.L., and Matalon, M. (1994). Hydrodynamic instability of a premixed flame under confinement. Combustion Science and Technology, **100**, 75–94.

Mikhelson, V. A. (1989). PhD Thesis, Moscow University. Moscow.

N'Konga, B., Fernandez, G., Guillard, H., and Larrouturou, B. (1993). Numerical investigations of the tulip flame instability—comparisons with experimental results. Combust. Sci. Technol., **87**, 69–89.

Oravecz, L.M. "Instabilities of Spreading Diffusion Flames in Microgravity and the Design and Construction of a Hele-Shaw Apparatus That Produces Flames in the Near Extinction Limit Regime Under Simulated Low Gravity Conditions." M.S. thesis. Michigan State University, 2001.

Patankar, S. V. (1980). Numerical heat transfer and fluid flow. Hemisphere Publishing Corp, Washington DC.

Patankar, S. V. and Spalding, D. B. (1972). A calculation procedure for heat, mass and momentum transfer in three-dimensional parabolic flows. International Journal of Heat and Mass Transfer. **15**, 1787-1806.

Perry, A.E., and Chong, M.S. (1987). A description of eddying motions and flow patterns using critical-point concepts. Annual Review of Fluid Mechanics, **19**, 125–155

Piechna, J. R. (2006). Feasibility study of the wave disk microengine operation. Journal of Micromechanics and Microengineering. **16**, 270-286.

Rayliegh, G. W. S. (1878). The explanation of certain acoustical phenomena. Nature. **18**, 319-321.

Rotman, D.A., and Oppenheim, A.K. (1986). Aerothermodynamic properties of stretched flames in enclosures. Symp. (Int.) Combust., **21**, 1303–1312.

Salamandra, G.D., Bazhenova, T.V., and Naboko, I.M. (1959). Formation of a detonation wave in gas combustion in tubes. Symp. (Int.) Combust., **7**, 851–855

Searby, G. (2009). Instability phenomena during flame propagation. Combustion Phenomena. CRC Press, Boca Raton, FL.

Settles, G. S. (2001). Schlieren and Shadowgraph Techniques. Springer-Verlag GmbH, Berlin.

Smith, G. P., Golden, D. M., Frenklach, M., Moriarty, N. W., Eiteneer, B., Goldenberg, M., Bowman, C. T., Hanson, R. K., Song, S., Gardiner, W. C., Lissianski, V. V. and Qin, Z. (2000). http://www.me.berkeley.edu/gri_mech/.

Starke, R., and Roth, P. (1986). An experimental investigation of flame behavior during cylindrical vessel explosions. Combustion and Flame, **66**, 249–259

Tanaya, Stefanus A. (2004) "Examination of a Simulated Micro-Gravity Device for Evaluating Flame Instability Transitions and Flame Spread Over Thin Cellulosic Fuels" M.S. thesis. Michigan State University.

Tanford, C. and Pease, R. N. (1947). Theory of burning velocity. Journal of Chemical Physics. **15**, 861-864.

Vagani, M. (2009). A wave disk engine concept for micro power generation. International Workshop on Micro and Nanotechnology for Power Generation and Energy Conversion Applications, Washington DC, December 1-4 2009.

Wichman, I.S., and Bruneaux, G. (1995). Head-on quenching of a premixed flame by a cold wall. Combustion and Flame, **103**, 296–310.

Wichman, I.S. and F.A. Williams. (1983). A Simplified Model of Flame Spread in an Opposed Flow along a Flat Surface of a Semi-infinite Solid. Combustion Science and Technology, **32**, 91-123.

Wichman, I.S. and F.A. Williams. (1983). Comments on Rates of Creeping Spread of Flames Over Thermally Thin Fuels. Combustion Science and Technology, **33**, 207-214.

Zeldovich, Y. B. and Frank-Kamenetskii, D. A. (1938). Thermal theory of flame propagation. Russian Journal of Physical Chemistry.

Zimont, V. L. (2000). Gas premixed combustion at high turbulence, turbulent flame closure model. Exp. Therm. Fluid Sci., **21**, 179–186.